8-2019

Generation and Modeling of Radiation for Clinical and Research Applications

Bishwambhar Sengupta
Clemson University, bishwambharsengupta@gmail.com

Generation and Modeling of Radiation for Clinical and Research Applications

---

A Dissertation
Presented to
the Graduate School of
Clemson University

In Partial Fulfillment
of the Requirements for the Degree
Doctor of Philosophy
Physics

---

by
Bishwambhar Sengupta
August 2019

Accepted by:
Dr. Endre Takacs, Committee Chair
Dr. Delphine Dean
Dr. Brian Dean
Dr. Jian He

Abstract

Cancer is one of the leading causes of death in todays world and also accounts for a major share of healthcare expenses for any country. Our research goals are to help create a device which has improved accuracy and treatment times that will alleviate the resource strain currently faced by the healthcare community and to shed some light on the elementary nature of the interaction between ionizing radiation and living cells.

Stereotactic radiosurgery is the treatment of cases in intracranial locations using external radiation beams. There are several devices that can perform radiosurgery, but the Rotating Gamma System is relatively new and has not been extensively studied. It has much flexibility as it uses fewer radiation sources which are capable of moving around the patient, unlike other systems that employ virtually static sources. We propose two new working modes of the RGS that will enable it to further extend its operational capabilities. We have studied the operation of an RGS device at the Rotating Gamma Institute in Debrecen, Hungary and have developed a Monte Carlo model of the same. The simulation results of the normal modes of operation are in close agreement with clinical results, thus validating our model. We have then used this model to propose the Intensity Modulated Radiosurgery (IMRS) and the Speed Modulated Radiosurgery (SMRS) mode of the RGS. In both modes, we can see that the penumbra falls off sharply along one axis which is required for treating cases near critical organs. While the IMRS has a disadvantage of longer treatment times, it is absent from the SMRS mode.

Current governing bodies state that any amount of radiation, with no threshold amount, is harmful and must be avoided at any cost. While this assumption is safe for radiation safety considerations, there is growing scientific evidence that the situation is more complex at low doses. In the modern day, we are continually exposed to low-dose radiation. Diagnostic imaging is one of the major contributors for exposure to low-dose ionizing radiation with over 70 million scans

performed annually in the US. This calls for the study of the effect that low-dose radiation has on cells. The scientific community is currently divided on the effect that low-dose radiation has on living cells as experiments have not been able to provide conclusive results. We have designed an incubator cabinet which allows the study of the effect of low-dose x-ray radiation on cells in a temperature- and atmospheric-composition-controlled, radiation-safe environment. We use bremsstrahlung radiation to excite quasi-monochromatic, fluorescent x-rays of a metal plate to act as a source that is used to irradiate biological samples. We have also installed a photon-counting detector to characterize the radiation incident on the cell cultures. By changing the tube current or by switching out the metal plates we are able to effectively change the dose rate, and the energy of the radiation, giving us the control to perform different experiments. Here, we have presented our device along with calculations that prove the capabilities of our device. We hope that future research will shine some light through the fog that currently engulfs radio-biology research in this radiation regime.

Dedication

I would like to dedicate this work to my family; Ma, Baba and Madhu.

Acknowledgments

I would like to start by thanking my advisor Dr. Endre Takacs. When I joined Dr. Takacss lab in the summer of 2016 I did not have much idea about Medical Physics. Yet, he accepted me as his Ph.D. student and has nurtured me into what I am today. I thank him for his patience as I stumbled through my research, for his kind encouragement and for his belief in me that I could succeed in my graduate career. Also for giving me the freedom to pursue projects in my way and for granting me several opportunities to explore new avenues in research. I have learned from him, both academic and life-lessons that would be valuable throughout my life. I also thank him for giving me the freedom to pursue my non-academic interests at Clemson. These activities have been my refuge from and helped me survive the grad school grind. Thank you, Dr. Takacs, for ensuring that I have a positive grad school experience.

I wish to express my gratitude to my Ph.D. committee members, Dr. Delphine Dean, Dr. Jian He, and Dr. Brian Dean. Thank you for your support and advice throughout my Ph.D. and for spending so many of your valued hours on my work and for providing counsel for my research career. You always made yourself available whenever I knocked on your door with any questions for which I shall remain forever grateful.

Many thanks to the Department of Physics and Astronomy and Clemson University for providing numerous grants for travelling to professional conferences and workshops. Attending these meetings have exposed me to my peers working in this field and has helped build my professional network. A special shout out to Dr. Daniel Thompson for being a great supervisor and for working with the TA's schedule in mind. Thank you for looking out for us.

I am grateful for the help and support from my lab mates: Leon Zheng, Donald Medlin, Justin Napolitano and Jaclyn D'Avanzo for making my experience at Clemson something that I will fondly remember forever. Thank you for volunteering to go through my work and screening for

errors, for the numerous questions that helped in my better understanding of the subject and most importantly, thank you for your friendship. It was a great experience working beside you and I wish you all the best and know that you will do well.

I would also like to thank the team at Medikai Innovacio Kft, especially David, Peter, and Tibor for their support and contribution towards this project. Thank you Dr. Filep for being a great mentor and for showing me around Debrecen. It was great chatting with you after work and thank you for sharing your experiences. I would also like to thank Laszlo Gulyas and Tamas Hollo from the Rotating Gamma Institute. Thank you for patiently answering my barrage of questions and for sharing your experiences working on the RGS. I could not have completed the project without your help and contribution. I had a great time working with yall. Köszönöm! I would also like to thank Dr. Josef Dobai and Dr. Imre Fedorcsak for sharing their clinical experiences with me and for being available to answer several of my questions.

I am highly obliged to Mr. Dan Pass of Moxtek Inc., for providing the experimental tube. Without your help, this project would not have been possible. I would also like to thank Shawn Chin for providing technical support for the detector and the tube from Moxtek.

I would like to thank my friends Mihiri, Abhishek, Puspal, Arghya, Kanishka and Samalka for their love and support and especially for enduring through my physics jokes and for helping in preserving my sanity. A special thanks to Paryatan Mandali for being there and making things happen and for the pearls of wisdom from Dr. Paliya which were really helpful. Thank you, Wren, for introducing me to Bojangles and many other important things in life. Thank you, Ethan, Andy, Chris, Amy, Yongchang, Yunhui, Gezhou, Fanchen, Yamei, Matt and Andrew for making the initial years and 310 more bearable.

Lastly and most importantly I would like to thank my family for their love, support, and understanding. To my parents, without your encouragement, it would not have been possible to come this far. Thank you for nurturing my curiosity and for giving me your blessings to pursue the path less traveled. To Madhu, for being the best sister and my biggest fan. Thank you!

Table of Contents

List of Tables

List of Figures

Chapter 1

Introduction

The National Cancer Institute (NCI) defines cancer as follows: cancer is the name given to a collection of related diseases in which the cells within the body begin to divide uncontrollably [1]. In 2015, it was found that 90.5 million people were living with cancer [2], with an estimate of 14.1 million new cases appearing per year [3], causing approximately 8 million death per year [4]. In the United States, one in three women and one in two men will develop cancer during their lifetime [5]. With a cancer survival rate of 67% in the US [6], it is rightly called The Emperor of all Maladies [5]. Due to the recent advancements and awareness on cancer, it is easy to mistake it as a disease that is caused due to our modern lifestyles. But we would be mistaken to assume so. Records and proof of cancer have been found in the texts [7] of ancient civilizations and in mummies from Egypt and Russia [8]. With the help of modern medicine, we now have average lifetimes long enough to experience a lot of cases of cancer. In most cases of cancer, the cells proliferate uncontrollably and have the ability to spread to different parts of the body. This is due to specific but abnormal changes that occur within the cell. More about these changes are discussed in the next section. The trigger for these changes may be exposure to carcinogenic chemicals [9, 10, 11], lack of proper diet and exercise [12, 13, 14], exposure to radiation [15, 16, 17], infection [18, 19] and genetic defects [20, 21, 22, 23]. There are several modes of treatment for cancer depending on the condition of the patient and how far the disease has progressed. Surgery to remove the cancerous tissue is performed when the cancer is isolated and in early stages of development [24]. Chemotherapy, a treatment type that uses anti-cancer drugs, can be administered as remedial, prolonging life or palliative modes [25]. Ionizing radiation is also used to treat cases of cancers in radiation therapy [26], radiosurgery [27]

and brachytherapy [28].

It has been observed that despite there being several different forms of cancer, all cancerous cells share some common traits. These traits allow them to overcome the several checks placed in our body and proliferate uncontrollably. In the following section, we will look at some of the common traits of cancer cells.

1.1 Cancer: Cells with Super Powers?

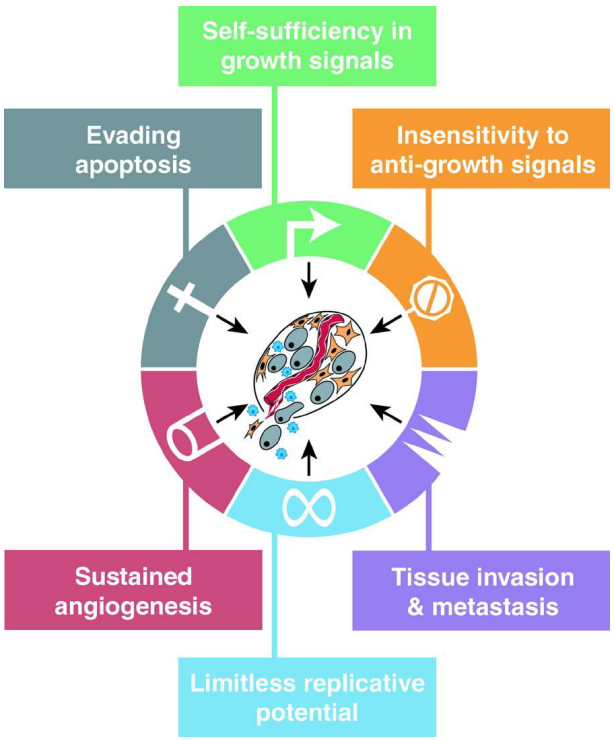

Figure 1.1: The Hallmarks of cancer cells [29]

1.1.1 Self-controlled growth signals

Regular cells are usually dormant and perform their regular function. On receiving an external mitogenic signal, mitogenesis is triggered and the cell switches from a dormant state to a proliferative state. These receptors are capable of binding several groups of molecules like diffusible growth factors, cell-to-cell interaction/adhesion molecules or extracellular matrix components to

name a few [29]. To the best of our knowledge, no ordinary cell can proliferate in the absence of such external stimulus. Most tumor cells mimic these growth signals to achieve self-sufficiency and independence from the normal tissue microenvironment. There are several ways in which the growth signals are replicated. Many cancerous cells can synthesize the growth factors (GF) to which they are responsive. This positive feedback loop is called autocrine stimulation [30]. Sometimes, the receptors that detect the growth signal molecules and transmits the signals into the cells are altered. They become hyper responsive and transmit growth signals even when the levels of growth factors are low-enough to not trigger proliferation in regular cells [30, 31, 32] and in extreme cases, it may also cause ligand-independent signaling [33]. The type of extracellular matrix receptors that are expressed can be switched, to favor the ones that promote growth signals [34, 35]. There are several indications that in human tumors, the growth signaling pathways are highly unregulated [36, 37]. There are several process that take place after the cell receives the growth signal. These possible processes form the circuit through which signals are carried out within the cell and are illustrated in the figure below. The change in the signal can happen at several places along the cell inner circuitry as has been observed earlier [36, 38, 39]. It is to be noted that just the independence from growth factor sources is not the full factor. It is becoming increasingly evident that other normal cells that constitute the cellular microenvironment also play a major role in the proliferation of cancer cells [40, 41, 42]. It is possible that the cancer cells may coax their normal neighbors into functioning in their favor [43, 44, 45] and more validation of this hypothesis is required to get the bigger picture.

1.1.2 Immunity from anti-growth signals

Analogous to the growth signals, regular cells also receive anti-proliferative signals to maintain homeostasis and cellular stability. Similar to the growth signals, the anti-growth signals can be an external growth inhibitor signal from the extracellular matrix and are received at the cell membrane receptors. Cell proliferation is stopped by either forcing the cell out of active proliferation state to be reworked in the future or to permanently stop them from proliferating by forcing them into a post-mitotic state [29]. Nascent cancer cells need to bypass these signals in order to thrive and try to adapt the cell circuit that carries this signal in their favor. Most of these signals are channeled through some specific protein pathways and these pathways are targeted and disrupted in several ways [46, 47, 48, 49, 50]. In some cases, the circuit may lose responsiveness at several places [50, 51, 52, 53, 54] while in others, they then develop dysfunctional receptors [50, 55]. Additionally,

cancer cells also have the ability to turn off the anti-growth signals from the extracellular matrix and promote pro-growth signals. There are also mechanisms through which the cells can block the transmission into post-mitotic non-proliferative state [56, 57, 58].

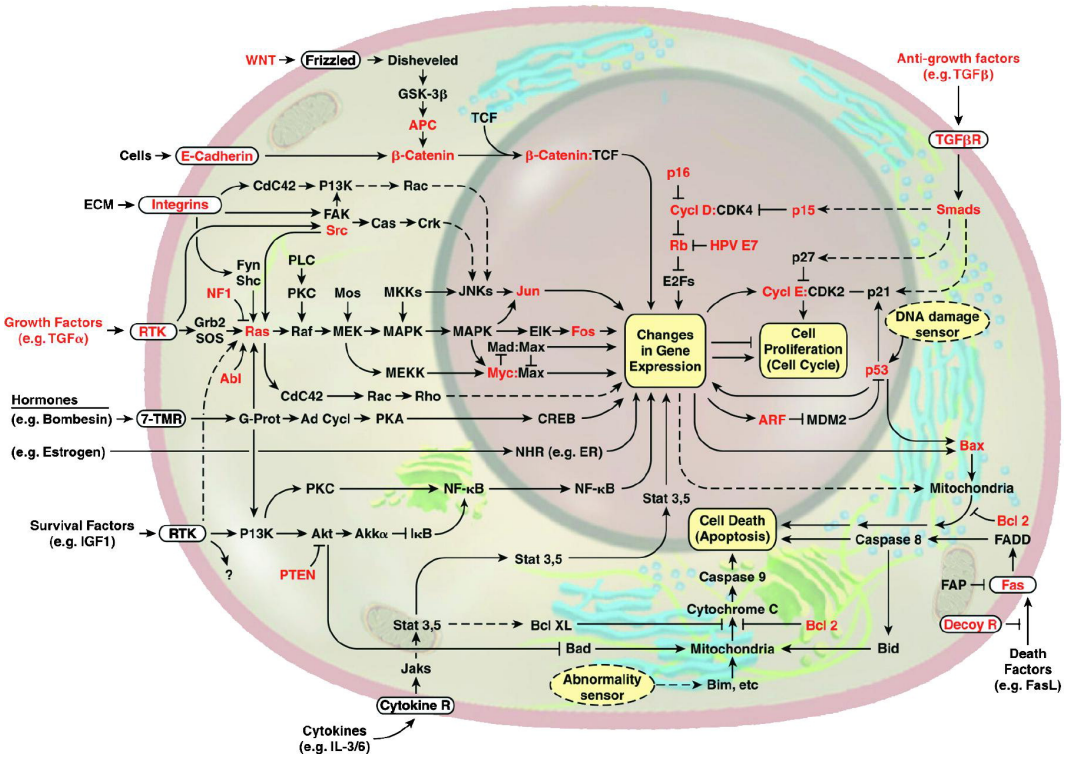

Figure 1.2: Cellular circuits: illustration of the inner mechanisms of cells [29]

1.1.3 Preventing apoptosis

Apoptosis is the programmed self-destruction of cells. This is a major way through which cell population is kept in control. It has been seen in several studies that resistance to apoptosis is a signature of almost all types of cancer cells. Almost all cells in our body have this self-destruct program. Once the sequence is initiated, the components of the cell are broken down within a span of $30 - 120$ minutes and the remnants of the dead cell are absorbed by the nearby cells within 24 hours [59]. The self-destruct sequence consists of two major sections: sensors and effectors. The sensors monitor the environment within and around the cell, seeking signs that might lead to cell death. These sensors, when triggered, set off reactions that lead to apoptotic death of the cell [35, 60, 61, 62, 63, 64]. Most apoptotic signals evoke a response from the mitochondria, which

produces catalytic molecules to speed up apoptosis [65]. Apoptosis effectors are also present within the intracellular matrix [66].

Apoptosis is considered a major obstacle for cancer [67, 68]. It is to be noted that the ability of cancer to thrive is not just due to cell proliferation [69], but also majorly due to its ability to evade apoptosis [70, 71, 72]. Cell apoptosis can be stopped by overexpression of the survival factors [73, 74, 75] or by disruption of the kill-switch circuitry [76, 77, 78]. It has been observed that whenever apoptosis in cells was prevented, either by inactivating the sensors or by suppressing the apoptosis circuit, a rapid growth in tumor cells followed [79].

1.1.4 Inexhaustible replicative ability

Regular cells have a finite number of replicative cycles [80]. Once they have completed the said number of cycles, they reach senescence, a stage where they do not grow anymore. The cells can then be forced to continue to go through replicative cycles, by disabling certain proteins [29] until they reach a second stage called crisis, which is characterized by large-scale cell death. The limit for replicative cycles for regular cells is between $60 - 70$ cycles. The cell does the counting of cycles by observing the telomeres, the ends of chromosomes. In each cycle, a part of the telomere is lost which finally leads to the apoptosis of the cell [81]. For the case involving malignant cells, it has been observed that after these may cycles, the rate of cell apoptosis is almost equal to the rate of cell accretion [82, 83, 84, 85, 86]. There is a very slim chance, 1 in 107, that a variant emerges from this stage with immortalization [82], the acquired ability to continue on the replicative cycle with no inhibition. Most cancerous cells have the ability to maintain telomere [87] levels above the critical threshold, by either adding to the ends of telomeric DNA [88] or by maintaining telomeres through the ALT mechanism [89], thereby giving them unlimited replicative potential. While immortalization is clearly understood, there is little known about how cancer cells avoid cellular senescence [80, 90].

1.1.5 Sustained angiogenesis

Angiogenesis is the growth of new blood vessels. It is clear that flow of blood, which carries oxygen and nutrients to the cells, is important for the survival and functioning of any tissue. Thus, cells are located in a tissue such that there is a blood vessel in the vicinity($< 100\mu m$). During the development of organs and tissues, the growth of new blood vessels is temporary and

is highly regulated such that it stops as soon as the requirement is met. Dormant blood vessels and blood vessels sprouting new capillaries express different signals. This combination of positive and negative signals, along with signals form the extracellular matrix decides if angiogenesis will occur [35, 91, 92, 93]. It is to be noted that tissues do not have the intrinsic ability to encourage angiogenesis and thus aberrant tissues lack the supply of nutrients and oxygen to prevent their capability to rapidly proliferate [94, 95, 96]. The signal receptors for angiogenesis reside on the surface of endothelial cells whereas the signal is carried by molecules in the extra-cellular matrix. These signals bind to the receptors on endothelial cells [30, 97]. There are many evidences that show the importance of angiogenesis for tumors [94, 95, 96, 98, 99, 96, 100]. It has been observed that angiogenetic ability is developed by the cancerous tissue before the appearance of a full-blown tumor growth [95]. Tumors induce angiogenesis by upsetting the balance between the positive and negative angiogenetic signals [101, 102, 103, 104, 105]. Thus, tumor angiogenesis is required for most cases of tumor for aggressive growth and thus can be a very effective treatment target for most cases of cancer.

1.1.6 Metastasis and tissue invasion

Metastasis is a pathogenic agents spread from a primary site to a different site within the hosts body [106]. This usually develops during the later stages of most cancer and is the leading cause of fatality from cancers in humans [107]. As the cancerous cells proliferate at the primary location, they compete for resources and nutrients and this ability lets them to depart from their primary site and migrate to a new part within the body where there is no resource crisis at the moment. At the new location, the cancerous cells recruit other healthy cells in their neighborhood to help proliferate. Metastasis is a highly complex mechanism and is yet to be fully understood [29]. It is believed that the mechanism is similar to the properties discussed above. There are several classes of proteins called the cell-cell adhesion molecules, that bind the cells in place inside a tissue. These proteins or their functioning are altered to get metastatic abilities [108, 109, 110, 111, 112, 113]. Metastatic cells also encounter new extracellular environment as they travel to new parts of the body and this is quite challenging. To successfully migrate to these conditions, the cancer cells now adapt by altering themselves such that they have a greater affinity to bind at these new substrates [91, 34]. The components of the extracellular matrix [114, 115, 116, 93] that holds the cells together, and neighboring cells [117] are also altered and degraded such that they can now dock into new surfaces

thereby enabling metastasis. The complexity arises from that fact that different kinds of cells are involved along with different kinds of extracellular environments. The mechanism of metastasis is not fully understood because of this reason, unlike the other properties discussed above which involve only a limited number of participants.

1.2 Research Objectives

According to the CDC, the total annual national health expenditure of the US in 2016 was $3.3 trillion [118]. This is approximately 18 % of the entire country's GDP [119] that year. Our research goals are two folds: i) to help create devices that with improved treatment accuracy while reducing the treatment time thereby freeing up more resources and infrastructure and, ii) To help in better understanding of the fundamental nature of radiation and how it effects cell. This will help in paving way for new modes of treatment procedures and safer radiation based equipment. The goals are explained in more details int eh following subsections:

1.2.1 Objective 1:

Stereotactic Radiosurgery (SRS) is a form of external beam radiation therapy that employs 3D target localization, known as stereotaxy, to guide several finely collimated radiation beams. The multiple radiation beams intersect at a focal spot to deliver a single, precisely localized, high dose of targeted radiation with low treatment planning margins [120]. SRS was mainly restricted to intracranial locations and are recently used to treat regions near the spine [121]. SRS devices may use high energy x-rays, accelerated particles or gamma-ray photons to deliver the dose and there are a number of device in the market currently of each kind. Highly accurate dose delivery is important for the treatment of cases near critical structures of the brain or near organs at risk. Intracranial radio surgical treatments performed with various types of devices have been well documented in the literature [122, 123, 124, 125], but papers describing the dosimetric capabilities of the RGS type machines are sparse [126, 127, 128, 129]. We propose to investigate the dosimetry of Rotating Gamma Systems (RGS) by creating a Monte Carlo (MC) model of the device in Geant4 and verify it to pave way for further development. We would also like to suggest two new working modes of the RGS that would bolster this devices clinical application to regions in close proximity to organs at risk.

1.2.2 Objective II: effect of low-dose radiation on cells

We are continually exposed to low-dose radiation in our daily life from a variety of sources like, background radiation, cosmic radiation, diagnostic procedures and sometimes from fallouts from industrial and military activities [130]. While the release of the nuclear bombs during World War II led to public opinion being swayed towards nuclear nonproliferation [131], the Nuclear disaster in Chernobyl sowed seeds of fear [132, 133] within peoples minds towards any forms of radiation. Soon, stricter regulations were put in place and any radiation, no matter how weak in energy or intensity (no threshold), was presumed harmful and this led to the establishment of the linear no-threshold model [134]. In the following decades, there were several studies that suggested that radiation, especially at low energies, may not be harmful for humans [135, 136]. There were also data from the various space missions to suggest the same [137]. Currently, the scientific community is divided on the effect of low-dose radiation on humans. Some studies have shown that is harmful [138, 139, 140, 141, 142, 143], while some other have concluded otherwise by observing hormesis [144, 145, 146, 147], and some were inconclusive [145]. There is a need for a controlled study that can solve this conundrum once and for all. It requires a setup that can deliver a fully characterized low-dose radiation to the target cells. Our goal is to build and commission such a device which will enable the study of the effect of low-dose radiation on living cells.

Chapter 2 and 3 have the fundamental principles and a summary of previous literature that has motivated our work. In Chapter 4, we discuss our work in the improvement of RGS, expanding their capabilities to perform near critical organs. In Chapter 5, we discuss a new setup that can be used to do a systematic study of the effect of low-dose radiation on cells which will once and for all dispel all ambiguity on the effect of low-dose radiation and any adverse effect that they may have on us. Chapter 6 discusses the conclusion of our research project and the results we have obtained so far. It also highlights the scope of some future studies that may stem from the current results.

Chapter 2

The Physics of Radiation

2.1 Electromagnetic Radiation

By definition, electromagnetic-waves are coupled oscillating electric and magnetic fields that propagate through space carrying energy and momentum at the speed of light. They are transverse in nature with the electric and magnetic oscillation taking place in planes perpendicular to each other and the direction of propagation. Their phases may differ as they travel through different media. Thus, they can be characterized by their wavelength, frequency, and phase angle. These waves are generally produced by charged particles subject to acceleration [148, 149] and interact with other charged particles and fields. Electromagnetic waves carry linear momentum, angular momentum, and energy. This energy is carried away from the source and can be imparted into the materials that they interact with. In general, their propagation is governed by Maxwell's equations [150].

Alternatively, quantum electrodynamics, the most advanced theory of the electromagnetic interaction, considers electromagnetic waves to consist of photons, which are charge-less elementary particles with no rest-mass. These are quanta of the electromagnetic field which form the basis of all electromagnetic radiation [151]. Quantum electrodynamics [152] also dictates how electromagnetic radiation interacts at the atomic level. In addition to the aforementioned sources, electromagnetic-waves can be produced from various quantum effects like atomic and molecular transitions and black-body radiation [153]. Each photon has a defined quantum of energy, which is proportional to

its frequency as described by the Plancks equation [154].

$$E = h\nu \tag{2.1}$$

Where h is Plancks constant, ν is the frequency of the photon, and E is the energy carried away by a single photon. The classical and the quantum explanations of electromagnetic-waves do not contradict each other. The two intersect in the concept of the wave-particle duality of Nature — all particles exhibit wave properties [155, 156] and vice-versa.

$$p = h/\lambda \tag{2.2}$$

where p is the particle's momentum and λ is the corresponding wave's wavelength.

For historical reasons, different regions of the electromagnetic spectrum are known by different names. For example, the tiny part of the spectrum that is visible to the human eye is called the visible or optical part of the spectrum. Electromagnetic-waves of the lowest energy are used for wireless communication and are called radio waves. The waves with the highest energy is called gamma-rays and they usually have extraterrestrial origins. Figure 1 is an illustration of the electromagnetic spectrum and its constituent regions.

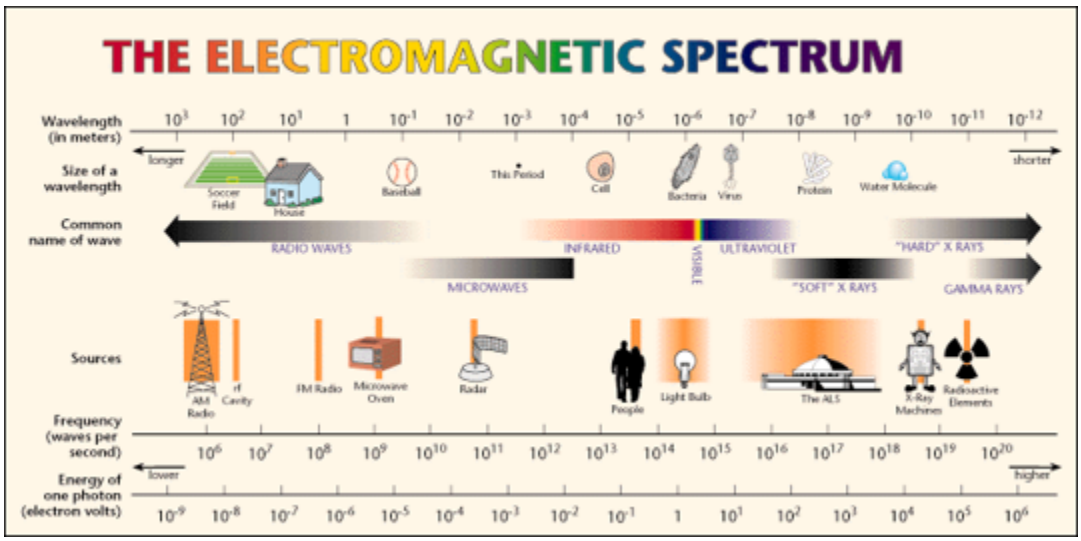

Figure 2.1: The electromagnetic spectrum [157]

How the different types of electromagnetic waves affect materials, chemical compounds, and

biological organisms are all different and depend on the energy that the photons carry along with the incident intensity and frequency. Hence, we can classify electromagnetic waves into ionizing and non-ionizing radiation depending on their ability to ionize target materials. Visible light and all electromagnetic waves carrying lesser energy, namely infrared, microwaves, and radio waves all fall under non-ionizing radiation. Whereas electromagnetic waves carrying more energy than the visible spectrum viz. ultra-violet waves, X-rays, gamma-rays and also particles emitted by radioactive elements all fall under ionizing radiation. Since non-ionizing radiation does not have enough energy, it does not interact much with the media through which it passes — at most leading to heating effects due to combined energy transfer by multiple photons. Ionizing radiation, on the other hand, has the energy to ionize molecules or break chemical bonds. Due to this destructive property, ionizing radiation can cause damage to biological cells and living tissue. Consequently, ionizing radiation is used in treating cases of cancer inside the body where it is used to selectively 'destroy' the cancerous tissues. In the subsequent sections, we will look more closely at the different kinds of ionizing radiation, their sources and properties, how they interact while propagating through media, and how we measure the amount of damage that they do to biological cells. We will also discuss the different quantities used to measure this damage, both in the lab and in the clinic.

2.2 Ionizing Radiation

As discussed earlier, radiation that is capable of ionizing the atoms and molecules of the medium through which it passes is called ionizing radiation. Both charged and uncharged particles can be sources of ionizing radiation. Each group can be further classified as follows:

- Charged particle radiation
  - fast electrons or positrons
  - heavy charged particles
- Uncharged radiation
  - electromagnetic radiation
  - neutrons

In the above classification, heavy charged particles include alpha particles, protons, fission products, or other products of nuclear reactions [158]. Fast electrons or positrons include beta decay particles and emitted in a nuclear decay and other processes. Electromagnetic radiation mentioned above primarily refers to the X-rays that are emitted in atomic transitions and gamma-rays that are a result of transitions between nuclear energy levels. Neutrons, both fast and slow, are the by-products of nuclear reactions.

The energy of ionizing radiation typically ranges between 10 eV to 20 MeV. Photons carrying energy lower than 10 eV do not have enough energy to ionize materials and the upper limit of 20 MeV is the typical upper bound of energy used in radiotherapy devices [159]. Sometimes ionizing radiation is also classified according to its hardness, i.e., its ability to penetrate different thicknesses in media. This, again, depends on the energy of the radiation in question. Low energy X-rays and alpha particles cannot penetrate deep into the material and are considered soft, whereas high energy X-rays and gamma particles are able to penetrate deep into the medium and are considered hard radiation.

2.2.1 Units and Definitions

Before we proceed further, we need to look into some units and definitions that will be used in our further discussions. Radioactivity [160] is defined as the spontaneous disintegration of atomic nuclei resulting in the emission of alpha particles, beta particles, and/or gamma photons. The activity of a radioactive source is defined as the rate of decay of its nuclei and is given by the law of radioactive decay:

$$\frac{dN}{dt} = -\lambda N \tag{2.3}$$

where N is the number of radioactive nuclei and λ is the radioactive decay constant.

Historically, the curie (Ci) was used as the unit for activity. It is defined as 1 $Ci = 3.7 \times 10^{10}$ disintegrations/second which is the best estimate of the activity of 1 gram of ^{226}Ra. For laboratory-scale experiments and measurements, millicurie (mCi) or microcurie (μCi) are more suitable orders of magnitudes to use.

The SI unit of activity is the becquerel (Bq). This was adopted at the 1975 meeting of the General Conference of Weights and Measured (GCPM) and is defined as one disintegration per

second and has now become the standard of activity [161]. In relation to the curie

$$1\ Bq = 2.703 \times 10^{-11} Ci \tag{2.4}$$

It is to be noted that the activity refers to the disintegration rate of a particular source in question. The specific activity of a radioactive source is defined as the activity per unit mass of the radioactive sample. For a pure radioactive sample, the specific activity can be calculated as follows:

$$Specific\ activity = \frac{activity}{mass} = \frac{\lambda N}{\frac{NM}{A_v}} = \frac{\lambda N}{M} \tag{2.5}$$

where M is the molar weight and N is the number of nuclei of the sample, A_v is the Avogadros number. λ is the decay constant of the isotope and it is equal to $\lambda = \frac{ln2}{t_{1/2}}$, where $t_{1/2}$ is the half-life of the radioactive nucleus in question.

2.2.2 Energy

Traditionally, the kinetic energy of charged particles is measured in electron volts or eV. It is defined as the kinetic energy gained by an electron upon being accelerated by an electric potential difference of 1 volt. This is a convenient unit when dealing with particle radiation as it is easy to calculate the energy it obtains from the electric field (potential difference $\times$ charge). In the laboratory, kilo electron volt (keV) and mega electron volt (MeV) are commonly used. The SI unit of energy is joule (J). It is related to the electron volt as follows:

$$1\ fJ = 10^{-15}\ J = 6.241 \times 10^{3} eV \tag{2.6}$$

For non-particle radiation, like X-rays and gamma-ray photons, the energy is related to the radiation frequency by the Plank-Einstein relation [154]:

$$E = h\nu \tag{2.7}$$

where h is the Planck constant ($6.626 \times 10^{-34} Js$ or $4.135 \times 10^{-15} eVs$) and ν is the frequency of the electromagnetic wave. The wavelength is related to the photon energy by $\lambda = 1.240 \times 10^{-6}/E$ where E is in eV and λ is in meters.

Table 2.1: Some pure β-emitters and their properties

Isotope	**half-life**	**max**
Cu-66	9.74E-06	2640
Pb-209	0.00038	644.4
Y-91	0.16	340.9
Sn-123	0.354	314
Bk-249	0.877	125.7
Ru-106	1	39.4
Pm-147	2.6	224.6
Kr-85	10.8	173.4
Cd-113m	14.1	580
Ar-42	32.9	600
Sm-151	90.1	54.8
Ni-63	100.2	66.9
Si-32	172.1	225
Ar-39	269.2	565
C-14	5734	156.5
Pd-107	6.50E+06	33

2.3 Sources of Ionizing Radiation

2.3.1 Fast Electrons

The most common source of fast electrons is a radioisotope that decays via a beta-minus emission. Schematically, it can be written as:

$$^{A}\mathrm{X}_{Z} \longrightarrow {}^{A}\mathrm{Y}_{Z+1} + \beta^{-} + \bar{\nu} \tag{2.8}$$

where X is the initial or parent nucleus, Y is the product or daughter nucleus, and $\bar{\nu}$ is the antineutrino. To conserve momentum, the recoiling nucleus Y will have a small recoil energy which is not enough to ionize media and, therefore, can not be detected. Neutrinos and antineutrinos have small interaction cross-sections with materials and remain undetected for all cases. As radionuclides are produced by neutron bombardment of stable atoms, there are a variety of beta emitters with half-lifes ranging from a fraction of a second to a few years. A small sample of the list is provided in Table 1 and a more comprehensive list can be found at the website of the University of Wisconsin-Madison [162]. The nuclear products from most beta-decays end up excited states and they de-excite by emitting gamma photons along with secondary beta-particles. Since the recoil energy of the product nucleus is almost zero, the energy is mostly shared by the beta particle and the antineutrino. As a

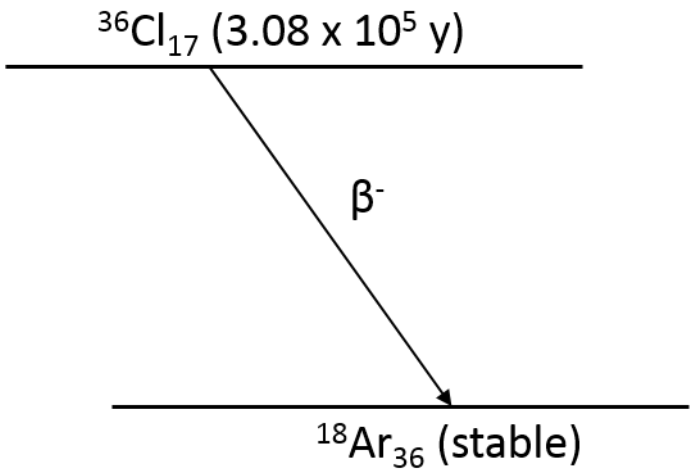

Figure 2.2: The decay scheme of ^{36}Cl

result the beta particles may have energies between the Q-value of the reaction and zero, usually in the MeV range.

2.3.2 Internal Conversion

Internal conversion occurs when the nucleus is at a higher energy state and and its relaxation to the ground state takes place by the emission of a beta particle. Due to the discrete energy levels of the excited nucleus the emitted beta particles are mono-energetic. In these cases, the nuclear excitation energy E_{ex} is directly transferred to one of the orbital electrons in the atom, which then leaves the reaction site with a kinetic energy of

$$E = E_{ex} - E_b \tag{2.9}$$

Here E_b is the binding energy of the electron in the atomic orbital it is ionized from. Due to the excitation energies of the nuclei these electrons usually appear with kinetic energies in the range of high keV to MeV. A list of transitions yielding internal conversion electrons can be found in the Handbook of Radioactivity Analysis [163].

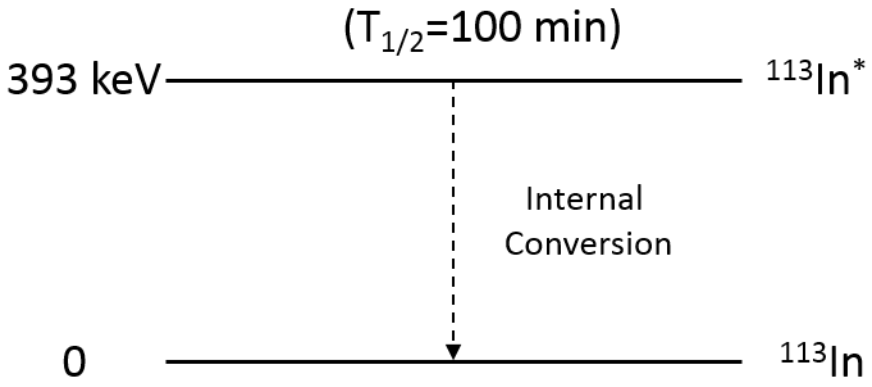

Figure 2.3: Internal conversion of the isomeric level in metastable ^{113}In

2.3.3 Auger Electrons

Auger electrons are generated in a similar way to internal conversion electrons, but the energy comes from a metastable atom instead of a metastable nucleus. The atom may become unstable due to an electron capture or it might have a vacancy due to some preceding process. This vacancy may be filled by an outer electron giving rise to characteristic photon or the available energy may be directly transferred to another bound electron. The result of the latter case is that the ionized electron will travel with a kinetic energy that is the energy difference between the initial atomic excitation energy and the binding energy of the second electron. For this reason, Auger electrons also produce a discrete energy electron-spectrum in the range of few keV. This process is mostly favored in low-Z elements for quantum mechanical considerations.

2.4 Sources of Heavy Charged Particles

2.4.1 Alpha Decay

Energetically unstable heavy nuclei undergo spontaneous emission of alpha particles to become stable. This decay is governed by the quantum barrier penetration mechanism [164]. The half-life of sources varies from days to many thousand years [165]. Using the same notation for the

parent and daughter nuclei as in 2.8 the decay process can be written as:

$$^{\mathrm{A}}\mathrm{X}_{\mathrm{Z}} \longrightarrow {}^{\mathrm{A}-4}\mathrm{Y}_{\mathrm{Z}-2} + {}^{4}\alpha_{2} \tag{2.10}$$

Alpha particles are mono-energetic as the nuclear energy levels are discrete and the energy is shared between the recoil nucleus and the α-particle in a way such that each α-particle appears with the same energy of $\frac{Q(A-4)}{A}$. Q is the Q-value (the energy liberated in the nuclear process) that characterizes the decay. In some instances, there may be more than one transition for the excited nucleus to decay to and the α-particle spectrum consists of particles with different well-defined energies [165]. α-particle energies vary between 4 MeV and 6 MeV and they correlate with the half-life of the parent element. α-particles having 6 MeV correspond to some of the shortest half-lives. Below 4 MeV, the probability for barrier penetration becomes very small and the half-life of the parent becomes too long (meta-stable nucleus).

2.4.2 Spontaneous Fission

Fission is the splitting up of a heavier nucleus into two lighter nuclei. Spontaneous fission is usually seen in extremely heavy nuclei and is very rare. Each fission gives rise to two fragments which travel in opposite directions. These fragments are medium weight with a positive charge and this process is asymmetric in nature, i.e., the fragments are clustered in heavy and light groups having an average mass-numbers of 143 and 108 respectively [166]. These fragments share around 185 MeV energy on average with the light fragment receiving a bigger portion of the energy due to the conservation of momentum.

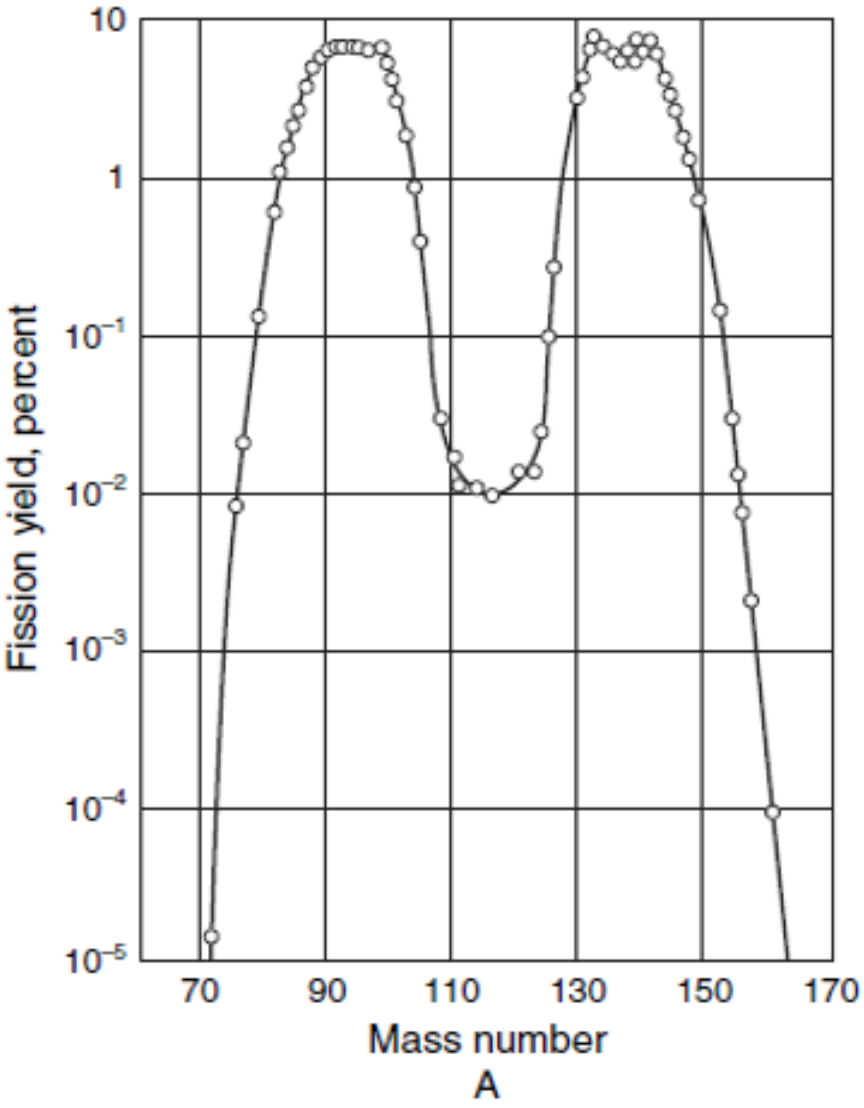

Figure 2.4: Fission product yields for ^{235}U from P.Lux [166]

2.4.3 Electromagnetic Radiation

2.4.3.1 Gamma-rays Following Beta Decay

Gamma radiation can be emitted after a beta decay while the nucleus is in the transition from an excited nuclear state to a nuclear state with lower energy. These are excited states of the daughter nucleus that are created during the beta decay of the parent nucleus. One of the decay schemes is shown in Fig. 2.5 [158]. As the average lifetime of the excited daughter nucleus is much smaller than the lifetime of the parent undergoing beta decay the gamma photons appear along with the half-life characteristics of the parent beta decay. Again, as the nuclear excited states have well-defined energies, the energies of the gamma-rays, emitted due to transitions between these states are also mono-energetic. Most gamma-ray sources have energies below 2.8 MeV determined by the excited energy levels available in nuclei.

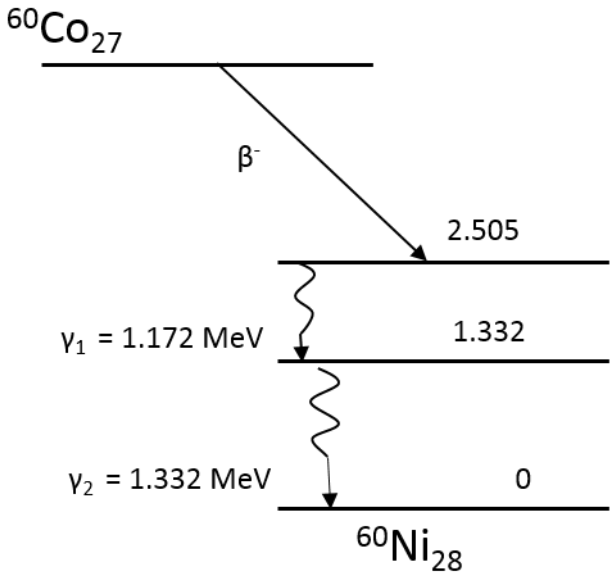

Figure 2.5: The decay scheme of ^{60}Co

2.4.3.2 Annihilation Radiation

Additional electromagnetic radiation is generated when a parent nucleus undergoes beta-plus decay. The positrons emitted in the primary decay process are do not travel far from their origin as there is an abundance of electrons, their antiparticle pair, they can get *annihilated* with.

Annihilation is the destruction of a particle and its antiparticle counterpart as a result of their spatial proximity. In the case of an electron-positron pair annihilation radiation is in the form of two photons of energy 0.511 MeV travelling in opposite directions due to momentum conservation.

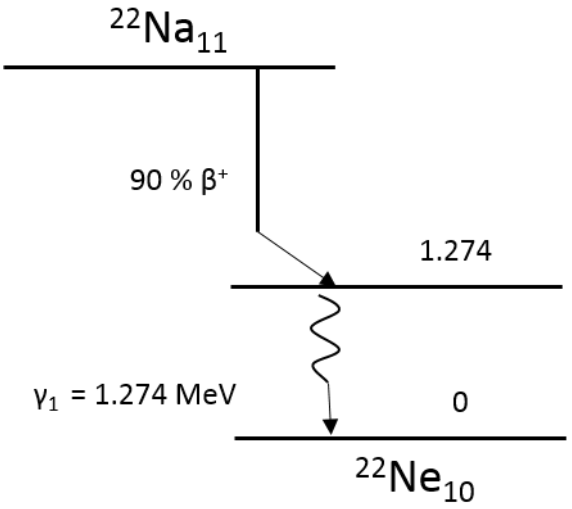

Figure 2.6: Annihilation radiation can follow a ^{22}Na to ^{22}Ne nuclear reaction. In this beta-plus decay process a position is created that can annihilate with an electron in the proximity of the nucleus.

2.4.3.3 Gamma-rays Following Nuclear Reactions

For gamma-rays of higher energy to be generated, higher excited nuclear energy levels must be populated. This usually happens in nuclear reactions. Some examples are shown below

$$^4\alpha_2 + {}^9\mathrm{Be}_4 \longrightarrow {}^{12}\mathrm{C}_6^* + {}^1\mathrm{n}_0 \tag{2.11}$$

$$^4\alpha_2 + {}^{13}\mathrm{C}_6 \longrightarrow {}^{16}\mathrm{O}_8^* + {}^1\mathrm{n}_0 \tag{2.12}$$

In the first reaction, the lifetime of C in the excited state is very short and, hence, we gamma photons experience a Doppler broadening due to Doppler shift. In the case of oxygen, the lifetime is long enough for the daughter nucleus to slow down and mono-energetic gamma-ray photons of

6.130 MeV can be observed. Usually, α-emitters are also mixed with other material for higher yield. For example, $^{238}PuO_2$ with an activity of $6 \times 10^9 Bq$ when combined with isotopically separated $200mg$ of ^{13}C yields 770 photons/sec of 6.130 MeV gamma photons [167].

2.4.3.4 Bremsstrahlung Radiation

When fast-moving electrons are suddenly slowed down, a part of their kinetic energy is converted into electromagnetic radiation called bremsstrahlung. The amount of energy converted to radiation increases with the incident kinetic energy and is higher for stopping material with the higher atomic number. This is an important process for the production of X-rays from conventional X-ray tubes. Since any amount of the incident kinetic energy may get converted to electromagnetic radiation, bremsstrahlung radiation produces a continuous spectrum. This is in contrast to the previous sources of radiation mentioned above as they are mostly mono-energetic due to the nature of their origin. Since bremsstrahlung radiation has a continuous spectrum, filtering is usually used before their use in different applications.

Bremsstrahlung radiation can also be observed when fast electrons being emitted from active beta-sources. When these beta electrons interact with atoms in the absorber media apart from bremsstrahlung characteristic X-rays can also created (discussed below). In this case the bremsstrahlung spectra is populated with characteristic peaks representative of the absorber media.

2.4.3.5 Characteristic X-rays

Fast-moving electrons and other radiation can ionize inner-shell electrons of atoms. The electrons from the higher energy levels fill the vacancy with the emission of a photon to ensure energy conservation. This is a fast transition, on the order of nanoseconds, and the corresponding X-ray energy is unique for each element as it depends on the energy difference between its electronic levels. These radiations are called characteristic X-rays. They are often used as atomic signatures to identify elements of an unknown sample.

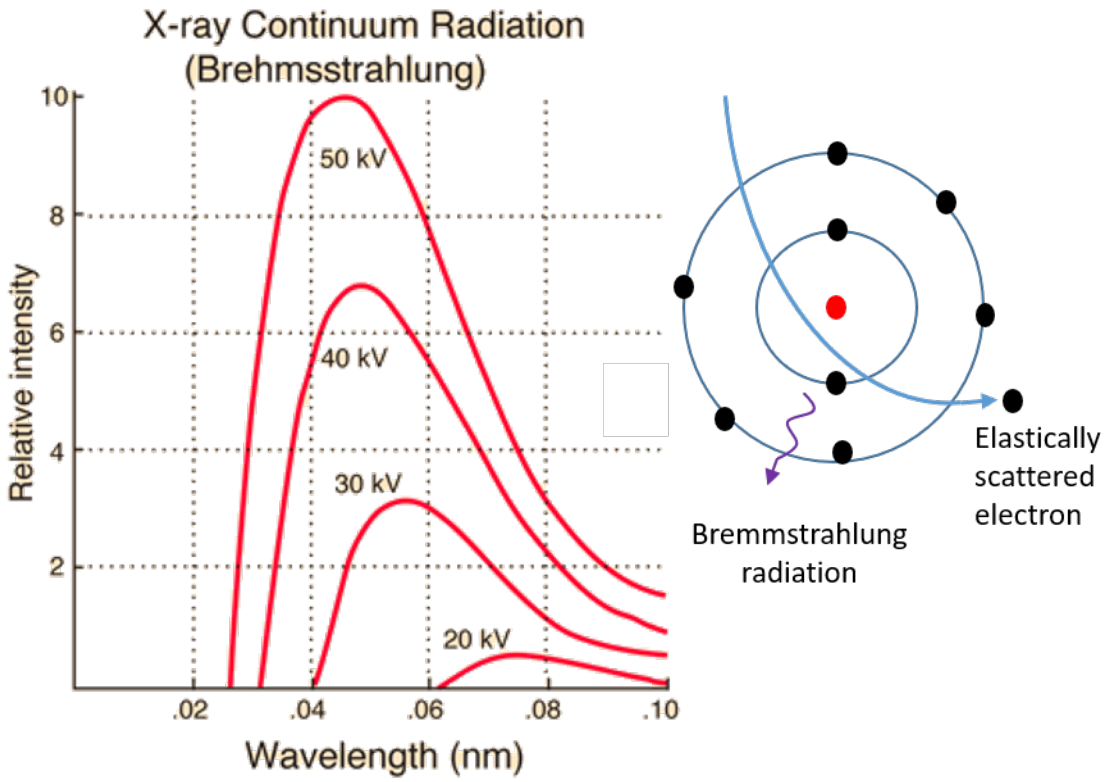

Figure 2.7: Bremmstrahlung radiation [168]

As an example, let an electron be ionized from the K shell of an atom. If an electron from the L shell fills the vacancy the photon emitted will have an energy equal to the energy difference between those two levels and is called a K_α photon. If an electron from the M shell fills the vacancy, it will have higher energy and is called a K_β photon. Hence, the highest energy that we can get from a $K-$shell electron being ionized will be the binding energy of $K-$shell electron. Vacancies created by electrons filling the vacancy of the $K-$shell can be filled by other electrons at even higher shells and we get a subsequent series of X-ray photons. It is to be noted that the intensity of lines from subsequent higher series can be lower than the $K-$series due to competing atomic processes. As discussed earlier, the energy of the $K-$series of X-rays depends on the element from which it is produced and varies from 1 keV for sodium, which has a $Z = 11$, to 100 keV for radium with a $Z = 88$. The characteristic X-ray energies of some elements are listed in Table 2 and more can be found in literature [169].

It is to be noted that an atom may be excited to a higher state by a variety of physical

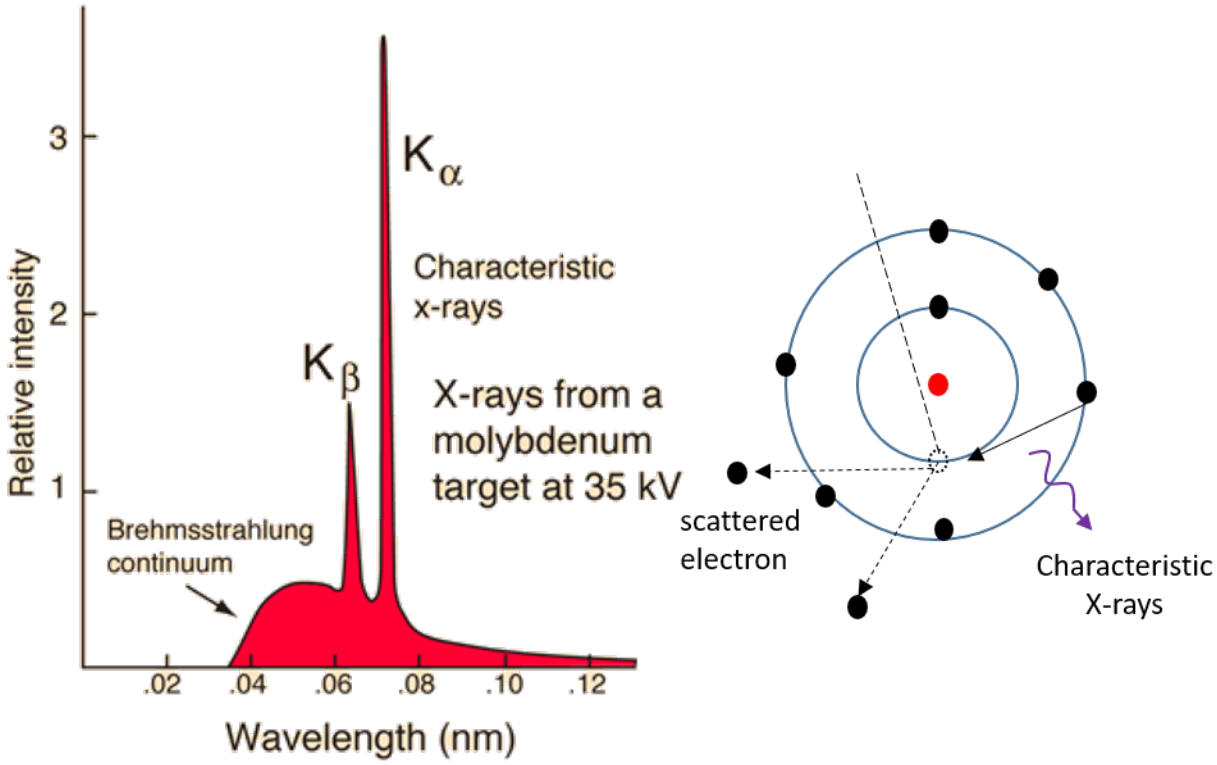

Figure 2.8: Characteristic X-ray radiation [168]

processes like excitation by radioactive decay or excitation by external radiation and, therefore, characteristic X-rays can also be found as secondary radiations from any of the above processes.

Table 2.2: Characteristic K_α X-ray energies of a few elements

Atomic Number	**Element**	**K-a Energy (keV)**
11	Na	1.041
13	Al	1.487
17	Cl	2.622
20	Ca	3.692
26	Fe	6.404
28	Ni	7.478
29	Cu	8.049
42	Mo	17.479

2.4.4 Neutrons

Excited nuclei can also decay by neutron emission. But this does not happen naturally and some prior event must excite the nucleus to higher energy levels. A few of these processes are summarized below.

2.4.4.1 Spontaneous Fission

Many heavy nuclides have high fission decay probability. Each fission event emits several fast neutrons, so these elements can serve as good neutron sources. As has been discussed earlier, fission can have several other by-products like gamma-rays, beta particles, etc. For these elements to be used as neutron sources, they are usually encapsulated in thick containers such that just the neutrons and gamma-rays emerge out from the source. A common example of a neutron source is ^{252}Cf, which has a half-life of 2.65 years and is produced in the decay of almost all transuranic elements.

Table 2.3: Characteristics of $Be(\alpha, n)$ neutron sources [158, 170, 171]

Source	**Half-life**	E_α **(MeV)**
$^{239}Pu/Be$	24000	5.14
$^{210}Po/Be$	138	5.3
$^{238}Pu/Be$	87.4	5.48
$^{241}Am/Be$	433	5.48
$^{244}Cm/Be$	18	15.79
$^{242}Cm/Be$	162	6.1
$^{226}Ra/Be$	1602	Multiple
$^{227}Ac/Be$ and daughters	21.6	Multiple

2.4.4.2 Radioisotope Sources

Neutrons are also produced in the direct decay of several radionuclides. A number of target materials can lead to (α, n) reactions for α particle energies that are available during radioactive decay. It has been found that the maximum yield is possible when beryllium is used

$$^{4}\alpha_{2} + {}^{9}\mathrm{Be}_{4} \longrightarrow {}^{12}\mathrm{C}_{6} + {}^{1}\mathrm{n}_{0} \tag{2.13}$$

Neutrons produced through this reaction have an energy of 5.71 MeV.

2.4.4.3 Photo-neutron Sources

Certain gamma-emitting radioisotopes can be used to produce neutrons under favorable conditions. Excited nuclear states can be achieved by the absorption of a gamma-ray photon which then allows the emission of a free neutron. ^{9}Be and ^{2}H are two nuclei for which the reaction yield is high enough to be of practical use.

$$^{9}\mathrm{Be}_{4} + h\nu \longrightarrow {}^{8}\mathrm{Be}_{4} + {}^{1}\mathrm{n}_{0} - 1.66\,\mathrm{MeV} \tag{2.14}$$

$$^{2}\mathrm{H}_{1} + h\nu \longrightarrow {}^{1}\mathrm{H}_{1} + {}^{1}\mathrm{n}_{0} - 2.226\,\mathrm{MeV} \tag{2.15}$$

One advantage of employing photo-neutron sources is that the resulting gamma-ray photons are mono-energetic, which yields neutrons energies that are also mono-energetic. A major disadvantage is that a large number of gamma-ray photons are required to make the intensity of this source high enough to be applicable for practical purposes.

2.4.4.4 Reaction from Accelerated Charges

Deuterons can be created in an ionized form and can be accelerated to attain high energy in accelerator facilities. If they collide with a deuteron or tritium rich targets neutrons are produced in the process.

The DD reaction:

$$^{2}\mathrm{H}_{1} + {}^{2}\mathrm{H}_{1} \longrightarrow {}^{3}\mathrm{He}_{2} + {}^{1}\mathrm{n}_{0} \quad \mathrm{Q} = +3.26\,\mathrm{MeV} \tag{2.16}$$

The DT reaction:

$$^{2}\mathrm{H}_{1} + {}^{3}\mathrm{H}_{1} \longrightarrow {}^{4}\mathrm{He}_{2} + {}^{1}\mathrm{n}_{0} \quad \mathrm{Q} = +17.6\,\mathrm{MeV} \tag{2.17}$$

The properties of neutron generator sources can be found in the literature [172, 173]. The Coulomb barrier for low Z elements is low, so the deuterons need not have high kinetic energy to make these reactions possible. Deuterium ions are accelerated by $100 - 300\ kV$ potentials and the resulting neutrons that are produced are approximately of the same energy. For example, in a neutron generator a 1 mA beam of deuterons will yield approximately 109 neutrons/sec when a deuterium target is used and approximately 1011 neutrons/sec when a tritium target is used. Other elements, like $^{9}Be(d,n)$, $^{7}Li(p,n)$ and $^{3}H(p,n)$ are also often used, but they require higher incident particle energy for the reaction to take place. Cyclotrons and Van de Graff accelerators are generally used for these reactions to be utilized as a neutron source.

2.5 Interaction of Radiation with Matter

The operating principles of detectors of ionizing radiation are based on the interaction of radiation with the material of the detector [158, 174]. In this section, we discuss how ionizing radiation interacts with matter and, accordingly, the methods to detect it. Following the discussions in the previous section, we could split the discussion of the interactions into the following four radiation categories:

- Charged particle radiation
- Fast electrons
- Uncharged radiation
- X-rays and gamma-rays

Particles belonging to the first two categories interact with the medium primarily through the Coulomb force with electrons of the medium. The particles in the last two categories are uncharged therefore they must first undergo an interaction with a charged particle involving either the the nuclei of the atoms or electrons in the media. In most cases, the outcome is a partial or full energy transfer resulting in excited atoms or free electrons. Subsequent processes distribute the energy within the medium in a way that in the end an electric signal is created that signals the arrival of

the particle and in most cases proportional to the deposited energy.If this reaction fails to take place within the detector, then radiation will pass through the detector undetected. For example, X-rays and gamma-rays can completely transfer their energy to the medium and the effect of daughter particles produced is similar to the interaction of fast electrons described earlier. Devices used for gamma-ray detection are tuned to promote such interactions and to fully contain the secondary particles, so that the entire energy from the gamma-ray photon may be absorbed and be accounted for.

2.5.1 Interactions of Heavy Charged Particles

2.5.1.1 Nature of Interaction

Heavy charged particles primarily interact with orbital electrons via the electric (Coulomb) force. Interaction with the nucleus, albeit rare, is possible, but it does not greatly affect the detection process.

Upon entering the medium, the charged particle interacts with free and bound electrons of the medium. Depending on the proximity of the charge therefore the strength of the interaction, bound electrons may be excited to a higher energy level (excitation) or be completely removed from the atom (ionization). The energy required to excite or ionize the atom comes from the incident charged particle and its kinetic energy is reduced after the interaction. There is a limit to the amount of energy that the incident particle can transfer in each interaction ($4Em_0/m$), so in general several interactions are needed to deposit all its energy into the medium. The incident particle can slow down and eventually lose most of its energy and stop. This interaction can be characterized by its *range* in any given absorbing material.

For example in photo-multiplier tubes radiation creates an initial free electron that multiply in a chain of acceleration and emission processes to create an output current signal. In other detectors electric field is applied to separate initially generated electron-hole pairs to create a similar output current.

2.5.1.2 Stopping Power

The linear stopping power, S, for a charged particle in a given absorber is defined as the rate energy loss by that particle per as it travels within the material.

$$S = -\frac{dE}{dx} \tag{2.18}$$

It is also called the *specific energy loss*. For any given particle, S increases as it loses its velocity within the material. The expression that connects the properties of the particle and that of the medium to the specific energy loss is known as the *Bethe formula* [158].

$$-\frac{dE}{dx} = \frac{4\pi e^4 z^2}{m_0 v^2} NB \tag{2.19}$$

where

$$B \equiv Z[ln\frac{2m_0 v^2}{I} - ln(1 - \frac{v^2}{c^2}) - \frac{v^2}{c^2}] \tag{2.20}$$

v and z are the velocity and charge of the primary particle, N and Z are the number density and atomic number of the medium, m_0 is the rest mass of electron and e the elementary charge. For most cases, $v << c$ and only the first term carries a reasonable contribution.

Bethe formula breaks down for ions at low energies, because when they slow down they capture electrons and get neutralized.

2.5.1.3 Energy Loss Characteristics

The Bragg-curve: The specific energy loss along the track of a particle is called the Bragg-curve. The Bragg-curve for alpha particles can be seen in Fig. 4.8. As α-particles have a charge of $+2e$ and, as predicted by equation 2.19, the specific energy increases as $1/E$. Towards the end of its track, the α-particle loses its charge by electron capture and the curve falls off. Particles with higher charge start capturing electrons early compared to lower charged particles in the same medium.

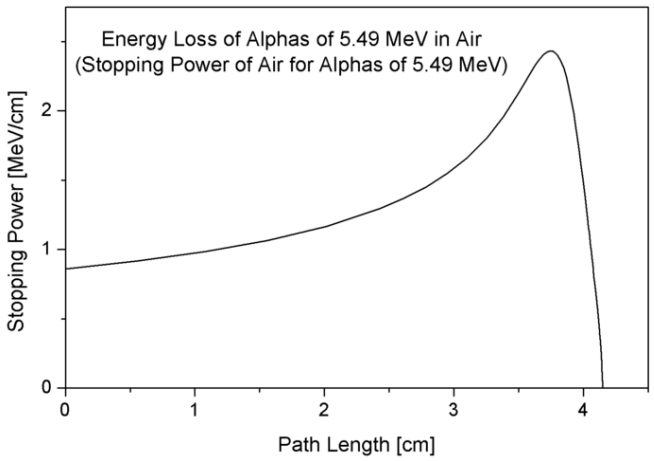

Figure 2.9: Specific energy loss of alpha particles in air by Helmut Paul [175].

Energy straggling: The interaction of charged particles with the neighboring media is a stochastic process which results in the energy spread of the beam as it passes through an absorber. The width, δE, resulting from interacting with the absorber medium is called energy straggling and varies with distance along the particles path. An illustration of this effect is shown in Fig. 2.11 below: The beams energy spreads out initially and narrows down at the end of its range as the particle energy has been reduced considerably.

Particle range: Particles lose their energy as they travel through an absorber medium. Their mean range is defined as the medium thickness that reduces the energy of the particle to zero. Sometimes an extrapolation method is used by extending the final, linear part of the curve to find zero position. As the definition suggests, the range of a certain type of charged particle depends on the absorbing medium. Experimentally, range data have been collected by performing measurements with a beam of mono-energetic charged particles. Detailed reports for example may be obtained from compilations like the Radiobiological Health Handbook issued by the U.S. Department of Health, Education and Welfare [177].

Range straggling: is defined as the fluctuation in the range of particles starting with the same initial energy. Again, statistical reasons that lead to energy straggling also lead to range straggling. For heavy charged particles, the straggling can be a few percents of the mean range. The degree of straggling will affect the sharpness of the range curve.

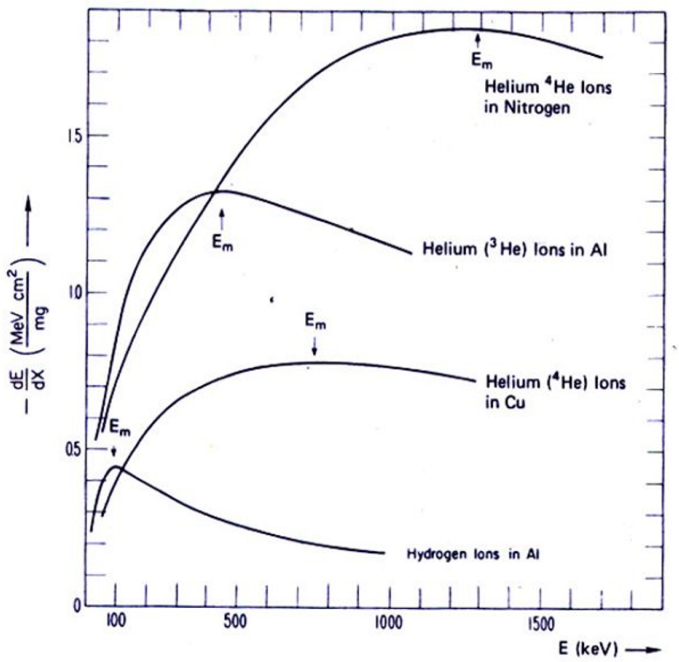

Figure 2.10: Specific energy loss as a function of energy for some positive ions [176].

Energy loss in thin absorbers: Most detectors have a thin layer of absorbing material that gets penetrated by the charged particle being detected. The energy deposited in the absorbing layer can be calculated as follows:

$$\delta E = [-\frac{dE}{dx}]_{avg} \times t \tag{2.21}$$

where t is the absorber thickness and $(-\frac{dE}{dx})_{avg}$ is the linear stopping power for the average energy of the particle inside the detector. Values for linear stopping power for differently charged particles for various media can be found in [178, 179, 180, 181, 182]. For low energies, particle ranges can be shorter than the absorber thickness, but as the particle energy increases, more particles pass through the medium without depositing any energy. The average energy deposited in a given thin medium will be given by the product of the thickness of the detector and the average linear stopping power.

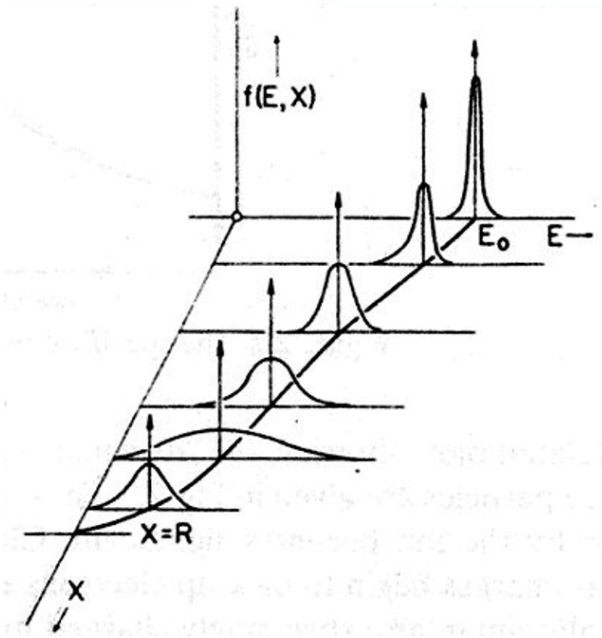

Figure 2.11: Energy distribution of initially mono-energetic charged particles at various penetration depths

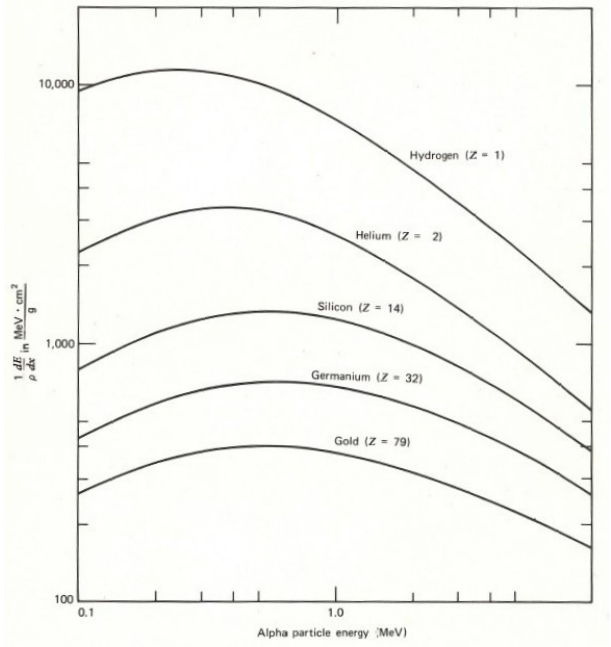

Figure 2.12: Specific energy loss of α-particles through thin absorbing medium [158]

Experimental data available for energy and range characteristics is not exhaustive. As a result, for complex mixture absorbers, the data is generated by the Bethe formula of equation 2.19 assuming that the stopping power is additive in nature in regardsto the different compounds. This is known as the Bragg-Kleeman rule.

$$\frac{1}{N_c}\left[\frac{dE}{dx}\right]_c = \sum_i W_i \frac{1}{N_i}\left[\frac{dE}{dx}\right]_i \tag{2.22}$$

Here N_c is the atomic density of compound, N_i is the atomic density of the ith component of the compound, $[\frac{dE}{dx}]_c$ is the linear stopping power, $[\frac{dE}{dx}]_i$ is the same for the ith component, and W_i is the weight fraction.

2.5.2 Interaction of Fast Electrons

Fast electrons, compared to heavy charged particles, lose energy at a much slower rate and go through a more complex path through the absorbing media. Large deviations of their path from the straight line are due to interaction with electrons of the medium, which have a similar mass. A large fraction of their total energy can be transferred in a single encounter. Interactions with the nuclei are also possible resulting in additional energy exchange.

2.5.2.1 Specific Energy Loss

Bethe gave the following relation for fast electrons to describe the specific energy loss by ionization and excitation:

$$-\left[\frac{dE}{dx}\right]_c = \frac{2\pi e^4 NZ}{m_0 v^2}\left[ln\frac{m_0 v^2 E}{2I^2(1-\beta)} - (ln2)(2\sqrt{1-\beta^2} - 1 + \beta^2) + (1-\beta^2) + \frac{1}{8}(1-\sqrt{1-\beta^2})^2\right] \tag{2.23}$$

where the symbols have the same meaning as in Bethe equation for α-particles and $\beta \equiv v/c$. Besides Coulomb interactions, electrons can also lose energy via radiative processes like bremsstrahlung or electromagnetic radiation which can be emitted from different positions in its wake. The linear radiative energy loss via radiative processes is be given by:

$$\left[\frac{dE}{dx}\right]_r = \frac{NEZ(Z+1)e^4}{137 m_0^2 c^4}\left[4ln\frac{2E}{m_0 c^2} - \frac{4}{3}\right] \tag{2.24}$$

From the above expression, it is clear that radiative losses are more important for high Z elements and for higher energy incident electrons. The total linear stopping power for an electron is the sum of contributions from collisional and radiative losses.

$$\frac{dE}{dx} = \left[\frac{dE}{dx}_c\right] + \left[\frac{dE}{dx}_r\right] \tag{2.25}$$

The ratio of the two terms is approximately equal to $EZ/700$ where E is in MeV. For the customary β-particles, the energies are in the low-MeV range and radiative losses contribute to a only a small fraction of total energy loss, but can become significant for higher atomic number media.

2.5.2.2 Electron Range and Transmission Curves

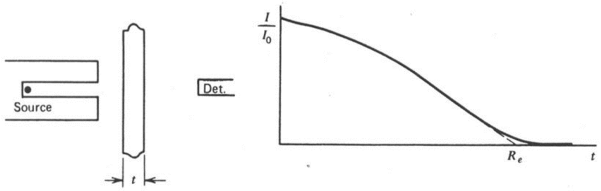

Figure 2.13: Transmission curve for monoenergetic electrons [158].

Electrons that penetrate the absorber and come out of the other side are the ones whose initial direction has changed the least number of times as they traveled through the absorber. For this reason, electron range is also not well-defined and is usually taken by extrapolating the linear portion of the curve as shown in the figure above. Specific energy loss for electrons is much smaller than those of heavy charged particles which makes their path in absorbers much greater than those of the heavy charged particles.

2.5.2.3 Absorption of Beta Particles

For β-particles emitted from radioactive sources, the transmission curves look different from the one shown in the figure above. These low energy β-particles are readily absorbed by absorbing media of small thickness, so the slope of the attenuation curve is much sharper and looks almost exponential. An absorption coefficient n may be defined by

$$\frac{I}{I_0} = e^{-nt} \tag{2.26}$$

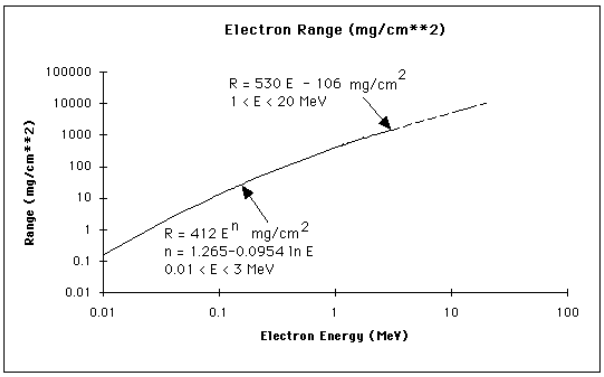

Figure 2.14: Range of β-particles for different energies in Si [183, 158]

Where I_0 is the counting rate without an absorber, I is counting rate with an absorber present and t is the absorber thickness given in $g/cm2$.

2.5.2.4 Backscattering

Backscattering is the large angle deflection of electrons in their paths. Due to this, an incident electron may emerge out of the detector and affect the efficiency of the detector. Backscattering is most prominent in electrons with low energy interacting with absorbers with high atomic numbers. This can also influence the yield from any radioactive isotope emitting β-particles or conversion electrons.

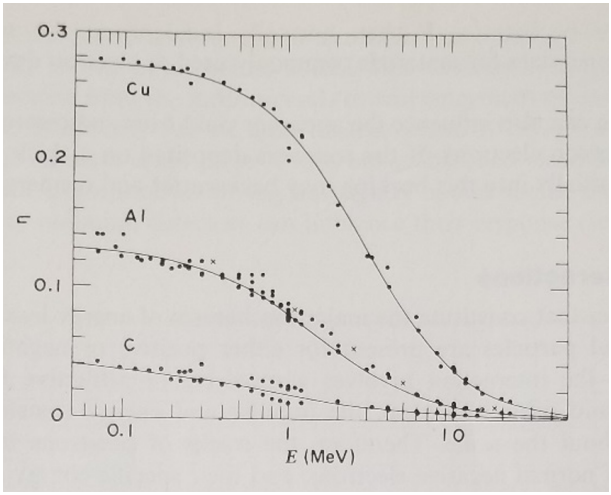

Figure 2.15: Fraction η of normally incident electrons that are backscattered as a function of energy [184, 158]

2.5.2.5 Positron Interactions

Most interactions discussed above for β-particles are due to Coulomb forces and are applicable for positrons as well. Since they have the same mass as electrons, most energy transfer cases are valid and similar for the positrons including tracks, specific energy loss, and range in an absorber. The only exception being the annihilation reaction discussed in the previous section. The resulting photon from an annihilation reaction has an energy of $0.511 MeV$ and as such can carry energy far away from the location of the reaction.

2.5.3 Interaction of Gamma-rays

There can be many possible routes of interaction between gamma photons and matter, but the three predominant ones for radiation measurement are the *photoelectric-effect*, the *Compton-scattering*, and the *pair production*. In these three processes, partial or full energy transfer occurs between the gamma photon and the electrons in the absorbing medium. Unlike the charged particles, if it takes place the interaction of gamma-photons is instantaneous with the possibility of the photon being scattered at large angles or get completely absorbed.

2.5.3.1 Interaction Mechanisms:

Photoelectric effect: Photoelectric effect was first observed in the later part of the $19th$ century when a zinc plate inside an electroscope was exposed to ultraviolet radiation. In 1905, Albert Einstein hypothesized that light carries energy in discrete energy packets photons to explain the experimental results. This laid the foundation of quantum mechanics and for the explanation of photoelectric-effect he later received the Nobel prize in 1921 [185]. In the photoelectric-effect, a photon having sufficient energy can interact with a bound electron in a way that it transfers all of its energy to the electron. The electron, now having enough energy, is able to leave its binding potential. In this process, the photon interacts with the atom as a whole and it is not possible between a photon and a free electron due to momentum conservation considerations. Photons with enough energy are able to remove the innermost electrons, which are tightly bound to the atom. The kinetic energy of a photoelectron is given by

$$E_{e^-} = h\nu - E_b \tag{2.27}$$

where E_b is the binding energy of the electron, h is Plancks constant and ν is the frequency of

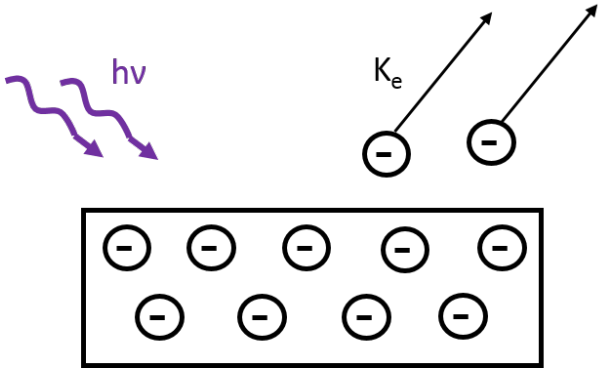

Figure 2.16: Illustration of the photoelectric effect

the incident photon. For gamma-photons of energy more than a few keV, most of the energy is converted into the kinetic energy of the photoelectron. In this process, the absorber atom is left ionized, which is quickly quenched by electron capture from the medium or internal rearrangement of electrons which results in characteristic X-ray photons. These X-ray photons are reabsorbed within the material through the photoelectric effect or the emission of Auger electrons.

The photoelectric-effect is the primary mode of interaction of soft X-rays with relatively low energies with matter and it is enhanced for absorbers of high atomic number. Fig. 2.17 shows the photoelectric absorption cross-section of sodium-iodide, a popular material used in gamma-ray detectors. The discontinuities appear at energies that correspond to the binding energies of the electrons in the absorbent atoms.

Compton-scattering: Compton-scattering is the most dominant interaction for gamma photons from radioisotope sources. In this case, the incoming gamma photon is scattered by a bound electron from the absorbing medium. The gamma photon transfers part of its energy to the initially at rest recoil electron. The scattered gamma photon will have less energy and changed momentum due to the energy and momentum transfer. The amount of energy transferred in this interaction can be a large portion of the initial energy of the gamma photon. The energy transferred in this interaction and the scattering angle can be derived from the conservation of energy and momentum and can be written as

$$h\nu' = \frac{h\nu}{1 + \frac{h\nu}{m_0 c^2}(1 - cos\theta)} \tag{2.28}$$

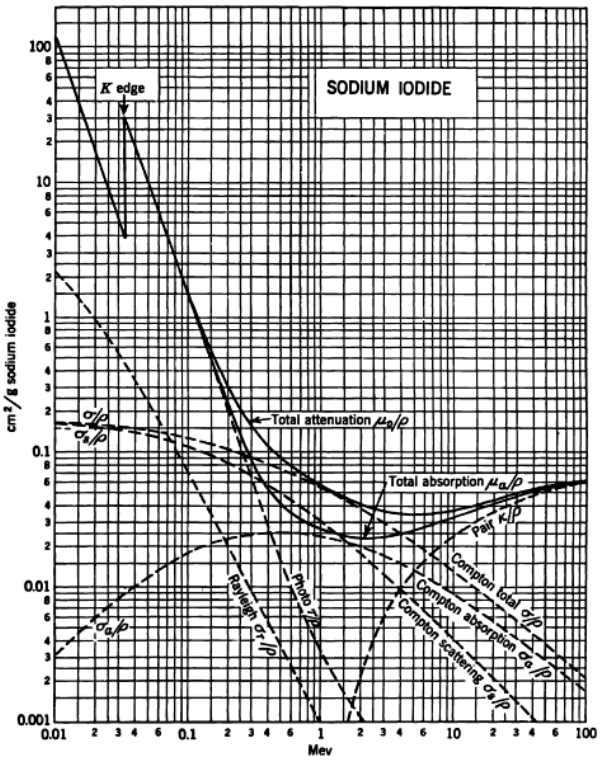

Figure 2.17: Absorption edges in NaI [174]

Where m_0c^2 is the energy corresponding to the rest mass of the electron ($0.511MeV$). The angle of scattering dictates the amount of energy transferred with a small amount of energy transferred for small scattering angles. However, the incident photon always retains some energy even when it is scattered by a large angle ($\theta = \pi$). The probability of a gamma photon to interact via Compton-scattering with each atom depends on the number of electrons present and thus increases as the atomic number increases. The dependence on the incident energy of the gamma photon can be seen in Fig. 2.19 The angular distribution of scattered photons will be given by the *Klein-Nishina formula* [158],

$$\frac{d\rho}{d\Omega} = Zr_0^2 \left[\frac{1}{1+\alpha(1-cos\theta)}\right]^2 \left[\frac{1+cos^2\theta}{2}\right] \left[1 + \frac{\alpha^2(1-cos\theta)^2}{(1+cos^2\theta)[1+\alpha(1-cos\theta)]}\right] \tag{2.29}$$

and is illustrated in Fig. 2.19.

Pair production: For pair production to be possible energetically, the incident gamma photon must have an energy that is more than twice energy that corresponds to the rest-mass

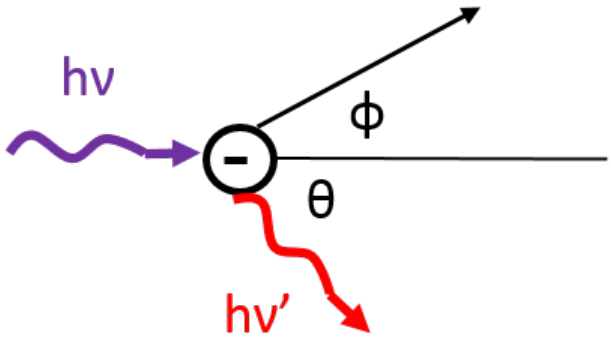

Figure 2.18: Illustration of the Compton-scattering

of the electron, i.e., more than $1.02MeV$. As a result, this interaction is dominant only for high energy gamma-ray photon.. A pair-production event must take place in the proximity of the nucleus for energy and momentum conservation considerations. Once created, the positron gets quickly absorbed in the medium and two annihilation photons are produced as the secondary products of this interaction. The probability of pair-production varies approximately as the square of the atomic number of the absorber. [174].

The probability of each of the above interaction taking place when a gamma-ray photon enters an absorbing media will depend on the energy of the gamma-ray photon and the atomic number of the absorbing media. The probability of each of these interactions occurring as a function of the energy f the incoming photon is shown in Fig. 2.20.

2.5.3.2 Gamma-ray Attenuation

Attenuation coefficient: Attenuation of gamma-ray photons in absorbing media is exponential in nature as shown in Fig. 2.21. In each interaction, the gamma-ray photon is either scattered or absorbed. The *linear attenuation coefficient* is the sum of probability per unit path length for each interaction to occur.

$$\mu = \tau(photoelectric) + \sigma(Compton) + \kappa(pair - production) \tag{2.30}$$

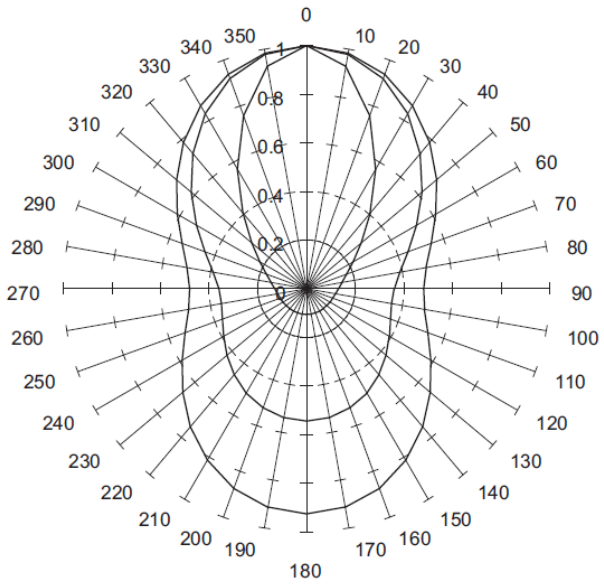

Figure 2.19: Dependence of Klein-Nishina cross-section on scatter angle for primary radiation of $10keV$, $100keV$ and 1000 keV [186].

The number of photons that are transmitted through the medium is given by

$$\frac{I}{I_0} = e^{-\mu t} \tag{2.31}$$

where t is the thickness of the medium. The reciprocal of μ gives the mean free path, λ, which is defined as the average distance that the photon travels in the medium before an interaction. For usual gamma energies, this can vary from a few millimeters to tens of centimeters, depending on the properties of the absorbing medium. It is to be noted that the linear attenuation coefficient, μ, will vary from case to case as it depends on the density of the object in question. Hence, the *mass attenuation coefficient* is more prevalent and widely adopted. For given energy incident photons, the mass attenuation coefficient remains constant irrespective of the physical state of the absorber.

$$mass attenuation coefficient = \frac{\mu}{\rho} \tag{2.32}$$

where ρ is the density of the medium.

Absorber mass thickness: In light of the mass attenuation coefficient discussed above,

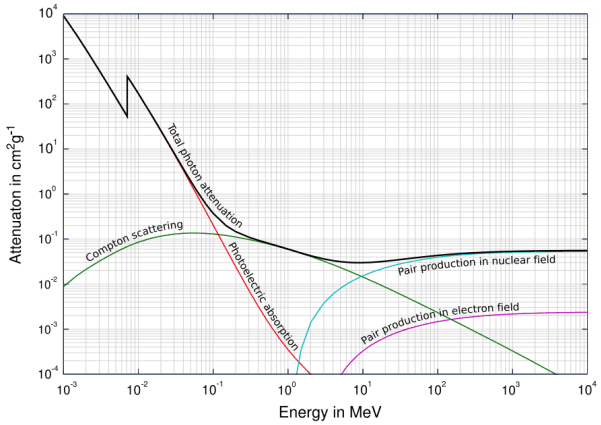

Figure 2.20: The probability of occurrence of different gamma-ray interactions with matter as the function of the energy of the photon [187].

the gamma-ray attenuation through any absorber can now be written as:

$$\frac{I}{I_0} = e^{-\frac{\mu}{\rho}\rho t} \tag{2.33}$$

Where ρt is called the mass thickness of the absorber and determines the degree of attenuation through the medium. This quantity is kept in mind while choosing materials for radiation protection and shielding. Range and stopping power, when expressed in terms of ρt, are approximately the same for absorbing material having similar Zs.

Buildup: Buildup is related to the total detector response in relation to the photons that are not collided. The detector is incapable of distinguishing photons with a direct path from the ones that followed an indirect path, and there might be a possibility that the detector is overcounting and thus the clean exponential attenuation will not be valid. In such *broad beam* conditions, the attenuation equation is replaced by the following:

$$\frac{I}{I_0} = B_{(t,E_y)} e^{-\mu t} \tag{2.34}$$

Where $B_{(t,E_y)}$ is called the *buildup factor* to account for the scattered photons. The value of the buildup factor will depend on the type of detector used and the specific geometry of the experiment.

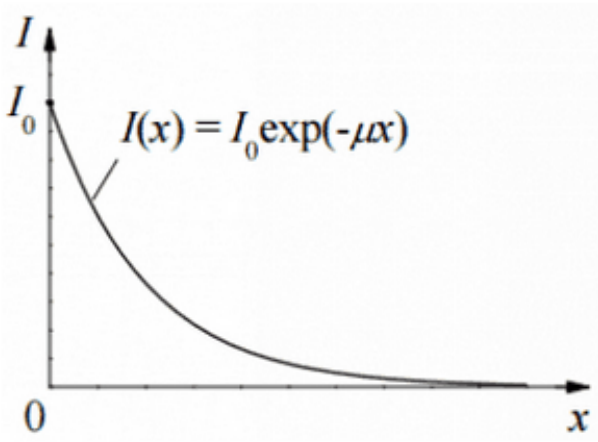

Figure 2.21: Gamma-ray attenuation in matter

2.5.4 Interaction of Neutrons

2.5.4.1 Properties of Neutrons

Neutrons are neutral and do not interact with atoms in the absorbing material with electric forces, which is the prevalent mode of interaction for charged particles. They often travel deep into the material without any interaction as the only possible way for them to react is with the nucleus of the atoms in the absorbing material. Therefore, the two possible modes of interaction for a neutron are:

- Being captured by the nucleus resulting in the emission of secondary particles or,
- Being scattered inside the absorbing medium.

In the case of neutrons, the secondary particles generated are mostly heavy charged particles. Most neutron detectors detect the heavy charged particles and use some conversion to account for the neutrons that might have created them. The probability of different neutron reactions varies greatly with neutron energy. Neutrons are classified as *slow* and *fast* neutrons on the basis of their energy — neutrons having energy less than 0.5 eV are classified as slow neutrons and the ones having higher energy are classified as fast neutrons.

2.5.4.2 Interaction of Slow Neutrons

Slow neutrons mostly interact via elastic scattering and neutron-induced nuclear reactions with the nuclei of the absorbing medium. Since the neutrons have low energy, very little energy is transferred to the nucleus in a collision and this mostly serves to slow down the neutron to *thermal equilibrium* levels ($0.025eV$) before another reaction can take place. The most important interactions involving slow neutrons are the neutron-induced reactions which produce secondary particles as these particles can be directly detected. A radiative capture reaction [(n, γ) reaction] is the most plausible reaction as the energy of the neutrons is so low. Since the products of this reaction are γ-photons, which are equally difficult to detect, this type of reaction is not preferred. A reaction like (n, α), (n, p) and $(n, fission)$ is preferred as the secondary particles produced are charged particles and are easier to detect.

2.5.4.3 Interaction of Fast Neutrons

Fast neutrons have higher kinetic energy and are able to transfer enough energy while scattering with the nuclei in the medium. The nucleus now recoils away with some kinetic energy. In this way, the neutrons are moderated to lower energies. Hydrogen is preferred to be used as a moderator as, due to their similar sizes, a neutron can transfer its energy completely in a single interaction. For neutrons having enough energy, inelastic collisions may also happen where they transfer enough energy to raise the nucleus to an excited state. The nucleus then de-excites by emitting gamma-ray photons. The neutron is also able to lose more energy per interaction in this way.

2.5.4.4 Neutron Cross-section

Probability per unit path length is constant for any interaction mechanism if the neutrons have fixed energy. It is defined as cross section ρ per nucleus for each type of interaction. It is traditionally measured in barns ($10^{-28}m^2$). A few reactions and their cross section dependence on neutron energy are shown in Fig. 2.22. The macroscopic cross-section is given by multiplying the cross section with the number of nuclei per unit volume. This now describes the probability per unit path length for a specific reaction to happen. For total probability, we combine the cross sections of individual processes.

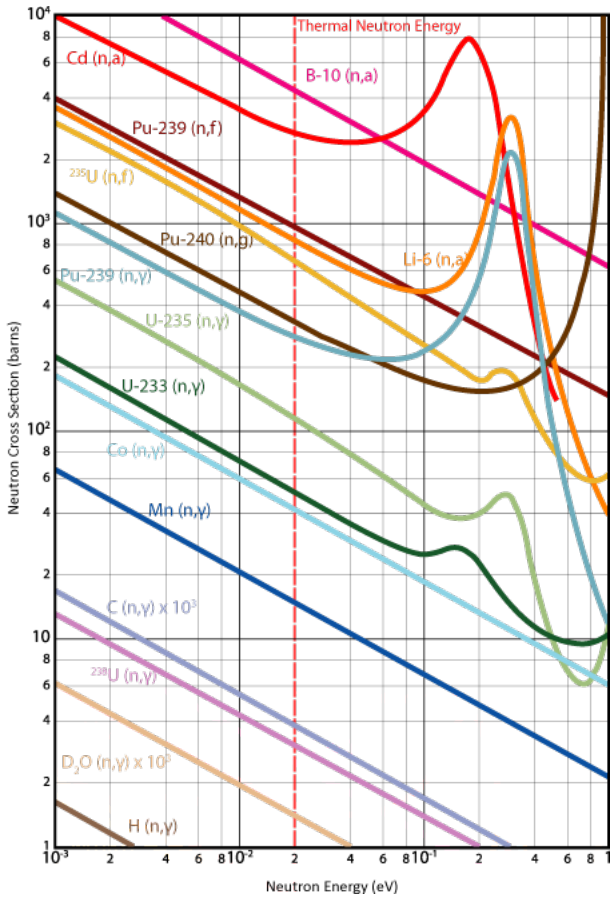

Figure 2.22: Reaction cross section versus neutron energy [188].

$$\Sigma = N\sigma \tag{2.35}$$

$$\Sigma_{tot} = \Sigma_{scatter} + \Sigma_{radiative\ capture} + \ldots \tag{2.36}$$

Σ_{tot} is the probability per unit path length for any interaction to occur. This is similar to the linear absorption coefficient for gamma-ray photons. Thus, the number of neutrons attenuated while traveling through an absorber on thickness t will be given by:

$$\frac{I}{I_0} = e^{-\Sigma_{tot}} \tag{2.37}$$

Analogous to the gamma-ray photons, the mean free path, λ, is given by $1/\Sigma_{tot}$. For slow neutrons, λ at most can be a centimeter whereas, for fast neutrons, it is usually tens of centimeters.

Chapter 3

Radiation Exposure and Dose

Since the discovery of X-rays and radiation, they have been used in several areas, from medical to commercial. With more use, it became clear that there was a need to understand and study the effect of ionizing radiation. Initially, there were attempts to measure on the basis of chemical and biological effects produced by radiation [189]. Skin erythema dose (SED) [190], was used in radiotherapy and was defined as the amount of X- or γ-radiation that would cause the reddening of the skin. The drawbacks of using this unit were that it depended on many factors like the type of skin, the quality of radiation, dose fractions, etc., which could not be standardized. Hence, the International Commission on Radiation Units and Measurements [191] (ICRU) was formed in 1928 with the primary objective to propose a unit of measurement of radiation as applied to medicine. They adopted the roentgen as the unit to measure X- and γ-radiation exposure.

3.1 The Roentgen

The quantity *exposure* is a measure of ionization produced in air by photons[189]. As per definition set by the ICRU [192], *exposure (X) is the ratio of dQ to dm; where dQ is the absolute value of total charge of the ions of one sign produced in air when all the electrons (negatrons and positrons) liberated by photons in air of mass dm are completely stopped in air.*

$$X = \frac{dQ}{dm} \tag{3.1}$$

The SI unit of exposure is coulomb per kilogram (C/kg). The historical unit, roentgen (R) is also used with a conversion of

$$1R = 2.58 \times 10^{-4}\ C/kg\ of\ air \tag{3.2}$$

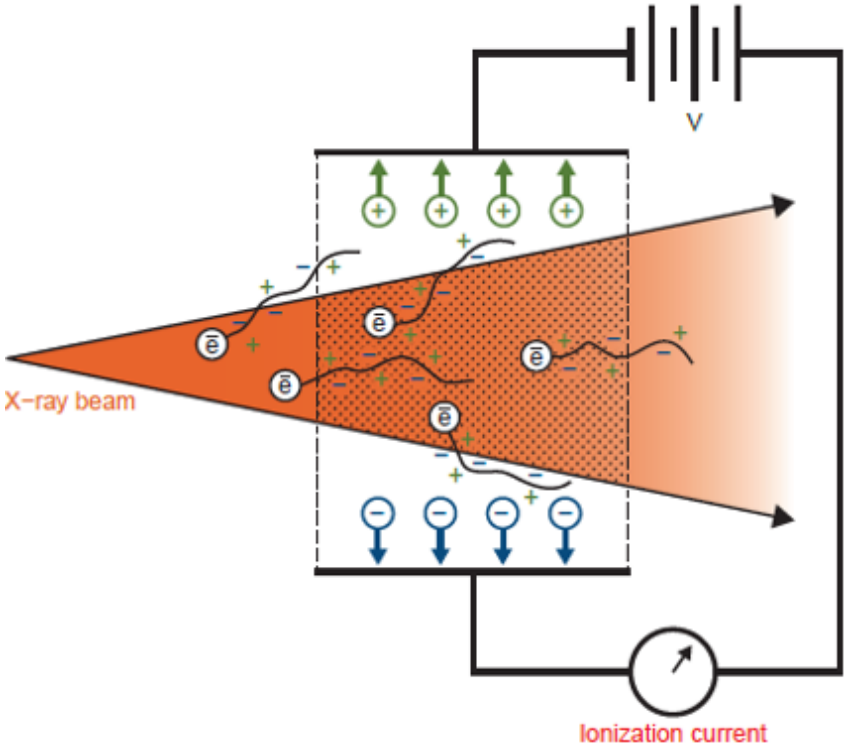

Figure 3.1: Measurement of exposure [189].

An illustration of the principle behind the device used to measure exposure is shown in Fig. 3.1. Ionizing radiation passing through air create electrons through the Compton effect, photoelectric effect, or pair production. The electric field across the collection plates separate the charges and the measured current is proportional to the exposure. Electrons produced within the region of interest may move out of the region while still retaining some of their energy. An electron created outside the region of interest may also move into the region. In a properly designed device electron equilibrium guarantees that losses and gains cancel and the measurement properly provides the above defined exposure values. This principle is fulfilled in free-air ionization chambers described in detail below.

3.2 Free Air Ionization Chamber

Ionization chambers are usually used to measure exposure from ionizing radiations. They are very sensitive and bulky and are usually used to transfer primary standard exposure rates for calibrating devices that are used in the field. During their use the source of ionizing radiation is placed at the location S in front of the instrument so that diaphragm D precisely define the amount of radiation entering the chamber. As radiation passes through the device electron equilibrium is created as shown in Fig. 3.2. The plates are maintained at a high potential difference, usually of the order of $100V/cm$, to collect electrons and ions that are produced due to the passage of ionizing radiation. The volume of air is precisely defined inside the C collector plates. Guard rings G ensure that the electric lines of force are straight in the region of interest.

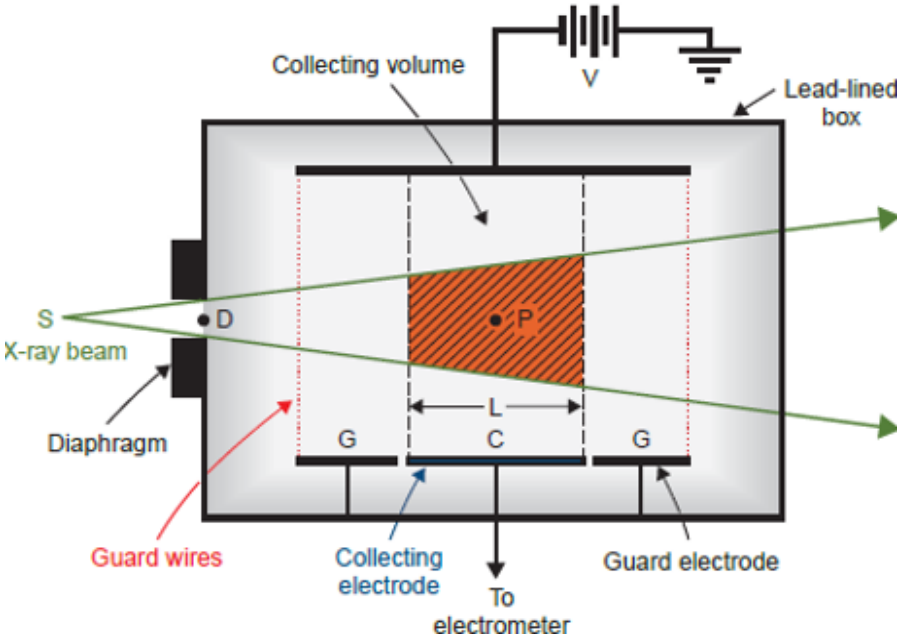

Figure 3.2: A schematic diagram of a free-air ionization chamber [189].

If ρ is the precisely measured density of air and ΔQ is the charge collected, then the measured exposure will be given by

$$X_p = \frac{\Delta Q}{\rho . A_p . L} . \frac{1}{2.58 \times 10^{-4}} R \tag{3.3}$$

A_p is the cross-sectional area of the beam, and L is the length of the collecting plate. For accurate measurements using this ionization chamber, the following corrections need to be taken into

consideration:

1. air attenuation
2. recombination of ions
3. effects of the environment like temperature, pressure, humidity on the density of air
4. ionization produced due to the scattering of photons.

For higher energies photons, the range of secondary charged particles produced in air increases and a larger distance is required between the plates. On increasing the separation, the uniformity of the electric field may be difficult to maintain. Also, with larger distances the recombination of ions before they reach the collector plate need to be considered as an additional correction factor. Nevertheless, these devices are extremely accurate and provide the primary transfer calibration standards for more accessible field use instruments.

3.3 Thimble Chambers

Due to the difficulties to use free air ionization chambers in clinical settings these chambers are rarely used in the field. Specially designed detectors with sealed air cavity inside them are used for field measurement instead. These devices consist of a volume of air that is sealed inside a metal shell. The shell thickness is chosen such that it is equal to the maximum range of electrons in air and an electrode is introduced into the cavity to measure the ionization charge produced. As the shell thickness is equivalent to the range of electrons in air, electron equilibrium inside the cavity exists in the measurement volume. As the volume of air inside the cavity is well defined, one can calculate the exposure by measuring the amount of charge collected within the chamber. An illustration of the thimble chamber is shown in Fig. 3.3. There are several factors that can affect the measurement of exposure using this device and for more details and information regarding other types of detectors, a standard textbook, like the Physics of Radiation Therapy by Faiz Khan is referred to [189].

As mentioned above, exposure is the measure of ionization produced in air by X-rays and γ-rays and cannot be used for photon energies above $3MeV$. Also, as different materials exposed to the same amount of X-ray or γ-ray radiation, different amounts of energy will be absorbed. As discussed earlier energy transfer increases with the atomic number in absorbing media and the occurrence of

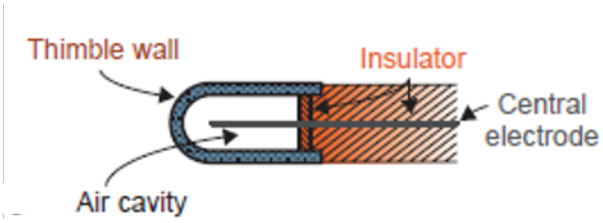

Figure 3.3: The basic principle behind a thimble chamber [189].

various physical and chemical reactions also changes with the amount of energy absorbed per unit mass of the material. Thus, it is important to extend the notion of exposure to different materials and use the the energy absorbed per unit mass to characterize the absorbed radiation. This quantity is known as the *absorbed dose*.

3.4 Absorbed Dose

Absorbed dose, sometimes also referred to as dose, is defined as the ratio $d\overline{\in}/dm$, where $d\overline{\in}$ is the mean energy imparted by ionizing radiation to piece of material of mass dm [193]. Historically, rad (radiation absorbed dose) was used as the unit of the absorbed dose, but today the SI unit is Gray (Gy).

$$1\ rad = 100\ ergs/g = 10^{-2}\ J/kg = 1\ cGy \tag{3.4}$$

3.4.1 Kerma

Kerma is related to the absorbed dose, but it measures the kinetic energy of secondary charged particles deposited in a volume. K or $k$inetic $e$nergy $r$eleased in the $m$edium is defined as the ratio of dE_{tr}/dm, where dE_{tr} is the sum of initial kinetic energies of all charged ionizing particles liberated by photons in the material of mass dm [193].

$$K = \frac{dE_{tr}}{dm} \tag{3.5}$$

It is measured in J/kg and the SI unit is also gray (Gy). For a photon beam, Kerma at any points on its path is proportional to its energy fluence Ψ and is related as follows

$$K = \Psi \left(\frac{\overline{\mu}_{tr}}{\rho} \right) \tag{3.6}$$

Here $\frac{\overline{\mu}_{tr}}{\rho}$ is the mass-energy *transfer* coefficient of the medium for given energy photons. It is related to the average mass-energy *absorption* coefficient as

$$\left(\frac{\overline{\mu}_{en}}{\rho} \right) = \left(\frac{\overline{\mu}_{tr}}{\rho} \right) (1 - \overline{g}) \tag{3.7}$$

where $\overline{g}$ is the average energy of electron lost in the radiative process. With this Kerma can be written as

$$K = \Psi \left(\frac{\overline{\mu}_{en}}{\rho} \right) / (1 - \overline{g}) \tag{3.8}$$

For lighter element absorbers, most energy of the radiation is used for ionizing the medium (*inelastic collisions*), but a small part also translates to radiative collision (*bremsstrahlung*) processes. Thus, Kerma can have two contributing factors:

$$K = K_{col} + K_{rad} \tag{3.9}$$

K_{col} and K_{rad} are the collisional and radiative parts respectively, and the two components of Kerma can be written as

$$K_{col} = \Psi \left(\frac{\overline{\mu}_{en}}{\rho} \right) \tag{3.10}$$

and

$$K_{rad} = \Psi \left(\frac{\overline{\mu}_{en}}{\rho} \right) \cdot \left(\frac{\overline{g}}{1 - \overline{g}} \right) \tag{3.11}$$

3.4.1.1 Relation with Exposure

Exposure, as defined earlier, is similar to collisional kerma but for ionization in air. It can be calculated by using the ionization charge produced per unit of energy transferred by photons. For dry air, the mean energy required to create an ion pair is $\overline{W} = 33.97 eV/ion\ pair$ [194]. Thus, $\frac{\overline{W}}{e}$ is the average energy required for a unit charge of ionization to be produced, where e is the elementary

charge. Therefore, exposure X, therefore can be obtained as

$$X = (K_{col})_{air} \cdot \left(\frac{e}{\overline{W}} \right) \tag{3.12}$$

or,

$$X = \Psi_{air} \left(\frac{\overline{\mu}_{en}}{\rho} \right)_{air} \cdot \left(\frac{e}{\overline{W}} \right)_{air} \tag{3.13}$$

3.4.1.2 Relation with Absorbed Dose

It is interesting to note the difference between absorbed dose and collisional kerma. Collisional kerma is maximum at the surface, as energy starts to get transferred to the atoms of the medium. As the photon progresses into the medium, it loses energy and thus, the value of collisional kerma also decreases. Absorbed dose, on the other hand, builds up initially and then starts to fall at the same rate as kerma. An illustration is shown in Fig. 3.4. As the photon enters the medium it starts to ionize it and this is reflected in the buildup region for the absorbed dose. At a region further into the medium, the photon has transferred most of its energy and now the absorbed dose is larger than the collisional kerma as his is the region of electron production. As we progress further into the medium, collisional kerma drops as there is no more source to create more ionization in the medium. Thus, the absorbed dose also falls at the same rate as the collisional kerma.

A more detailed analysis of absorbed dose and different methods for calculating them can be found in the literature [189, 195, 196, 197].

3.5 Radiation Protection and Shielding

Ionizing radiation can potentially cause serious damage to biological cells and tissues. Once these hazards were realized, exposure limits and radiation protection standards started to be introduced. National and international organizations such as the International Commission on Radiation Protection (ICRU) [191], The Nuclear Regulatory Commission(NRC) [198] and the National Council on Radiation Protection (NCRP) [199] function as standard defining and regulatory bodies.

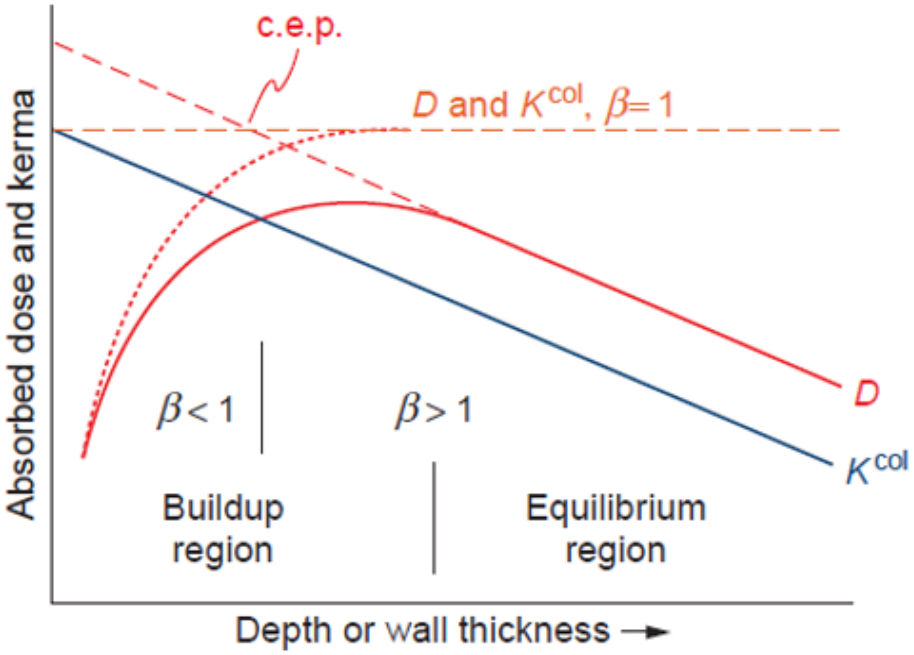

Figure 3.4: Relation between absorbed dose D and collisional kerma K_{col} [189]

3.5.1 Dose Equivalent

In the case of biological cells and living tissues, damage due to exposure to ionizing radiation is due to the chemical changes that are triggered. The absorption of the same energy per unit area from different sources of ionizing radiation can have very different effects. The severity of these changes is proportional to the local rate of energy deposition along the particles track [158]. We have seen that heavy charged particles have a higher rate of energy deposition compared to electrons and thus must cause more biological damage than electrons. Thus, while designing radiation protection equipment, a quantity called the *dose equivalent* (H) needs to be used.

$$H = D \cdot Q \tag{3.14}$$

Where D is the absorbed dose and Q is the quality factor of the type of radiation. The SI unit is still J/kg, but the dose equivalent is measured in sieverts (Sv).

$$1\ Sv = 1\ J/kg = 10^{-2}\ rem \tag{3.15}$$

Table 3.1: Quality factors for particles of different energies

Radiation	**Quality**
X-rays	1
γ-rays	1
electrons	1
Neutrons $<$ 10 keV	5
10-100 keV	10
100 -2 MeV	20
2 - 20 MeV	10
$>$20	5
Protons $>$ 2 MeV	2
α-particles, fission fragments, heavi nucleii	20

Quality factors are multiplicative constants chosen such that they represent the linear energy transfer (LET) component of the ionizing radiation. A list of some quality factors is shown in Table 3.1.

When performing a treatment, not all organs or tissues receive the same amount of exposure as their density, constituent components, and location with respect to the source may be different. Each tissue or organ may also have different sensitivities to various radiation-induced effects. To account for all of these factors, a term called the effective dose equivalent has been introduced. It is defined as the sum of the weighted dose equivalents for irradiated tissues or organs [200].

$$H_E = \sum W_T H_T \tag{3.16}$$

Here W_T is a weighting factor for tissue T and H_T is the average dose equivalent in tissue T. The weighting factors for different tissues, W_T, represent the statistical risk of the tissue when the body is exposed to uniform radiation. The weighting factor for a few organs and tissues are listed in Table 3.2 and a full list can be found from the National Council on Radiation Protection and Measurements Report Number 116 [200].

Table 3.2: Some values of weighting factors

Tissue(T)	**WT**
Skin	0.01
Breast	0.05
Liver	0.05
Thyroid	0.05
Lung	0.12
Stomach	0.12
Total	1

3.6 Background Radiation

The International Atomic Energy Agency (IAEA) [201] defines background radiation as the dose or dose rate that is attributable to all sources other than the ones specified [202]. This dose rate exists in nature at a particular location before the measuring device or source is brought there. Background radiation can have the following sources:

1. terrestrial radiation, like natural radioactive ores, or accidents like the Fukushima-Daichi incident, or radiation from weapon testing
2. cosmic radiation
3. radiation from ingested radioactive elements

3.6.1 Sources of Background Radiation

Terrestrial sources: Terrestrial sources of radiation can vary over the geographic region. This includes sources of radiation that are outside the human body. The most common radionuclides that contribute to this background are potassium, uranium, thorium and their decay products like

Table 3.3: Exposure from natural background radiation[203, 204]

Radiation Source	**Average Annual Exposure in mSv at**	
	World	**US**
Airbourne/Inhaling	1.26	2.28
Ingestion	0.29	0.28
Terrestrial	0.48	0.21
Cosmic	0.39	0.33

radium and radon. In its natural state radon exists as a gas and can be easily inhaled. In the US, radon is the second most frequent cause of lung cancer [205, 206]. Most of the elements, like potassium and uranium, have a long half-life and their concentrations are gradually decreasing. But others like radium and radon with shorter half-lives have not decayed away yet as they are being continually produced in nature. Almost all of them decay via processes that have daughter particles in the keV-MeV range. The global average annual exposure from inhaling radon is $1.26mSv$ [203] and in the US, the annual average is $2.28mSv$ [204].

It has been observed that natural background radiation varies geographically. There are reports of some areas having much higher background radiation than the global average [207, 208]. Ramsar, in Iran, has a mean dose of 10.2 mGy/yr with a maximum of 260 mGy/yr [136]. In Guarapari in Brazil, the mean radiation level is 5.5 mGy/yr with a maximum of 35 mGy/yr [208]. Karunagapalli in India and Yangjian in China come in at the end of this list with mean annual doses of $3.8mGy/yr$ and 3.5 mGy/yr, with maximum doses of 35 mGy/yr and 5.4 mGy/yr respectively [135, 209]. In comparison, the global average for annual dose from natural background radiation is 0.5 mGy/yr [208]. The high values in Iran are due to the use of radioactive limestone in building materials, that occurs naturally in the region. People there also receive additional dose from inhaling radon [130]. For the cities in India [135] and Brazil [210, 211] the high background radiations are due to the abundance of a phosphate mineral called Monazite in these regions [212].

Cosmic-rays: We are constantly being bombarded with extraterrestrial ionizing radiation. These mainly consist of positively charged particles and heavy nuclei mostly coming from the solar wind. When these particles interact with the atmosphere, they create a shower of secondary particles and radiations that include X-rays, protons, alpha-particles, muons, pions, neutrons, and electrons. Exposure from these particles depends on the elevation and change with the proximity to the ionosphere. As an example, at the altitude of $30,000$ feet, which is the altitude that regular passenger aircraft maintains, the exposure is 5 $\mu Sv/h$ [213, 214, 215, 216, 217, 218]. Also, in the city of Denver, CO, which is at an elevation of 1650 meters above sea level, the exposure from cosmic dose is almost double of that at the sea level [219]. Cosmic radiation becomes a greater concern during the various space missions and experiments that the astronauts perform on a regular basis. A detailed report can be found on the amount of exposure received by astronauts during several space missions [137].

Ingested sources: We receive internal exposure from radioactive elements which we take

Table 3.4: Some naturally occurring radioisotopes and their half-lives

Radioactive Isotope	**Half-life**
^{40}K	1.25×10^9 *years*
^{14}C	5730 *years*
^{45}Ca	162.7 *days*
^{210}Pb	22.3 *years*
^{210}Po	138 *days*
^{226}Ra	1600 *years*
^{228}Ra	5.75 *years*

into our bodies through food and water, and through the air we breathe. In addition, we naturally have radioactive elements (potassium-40, carbon-14, radium-226) in our blood or bones [220]. We ingest or inhale these elements in our day to day life and there are many different radioactive substances in our body at any time. A list of such radioactive nuclei and their half-lives is provided in Table [221, 222, 223].

During and after World War II several nuclear bombs were tested and detonated [224, 225, 131], which resulted in radioactive contamination of the environment. In 1963, several nations got together to sign the Partial Test Ban Treaty (PTBT) [226, 227] that prohibits the test of nuclear weapons except for those conducted underground. Since then 123 countries have signed the agreement [227]. Due to these testing, the background radiation levels had peaked during 1963 to approximately 0.15 mSv/yr, but since the ban, the worldwide levels have gone down to 0.005 mSv/yr by the year 2000 [228]. Nuclear accidents also contribute to background radiation. Although, they are very rare there were two major notable incidents that had global effects: the Chernobyl accident and the Fukushima Daiichi nuclear disaster. It is estimated that, due to the Chernobyl accident, ionizing radiation levels were as high as 5.6 roentgen/sec near the incident site. This resulted in over $20,000$ roentgens per hour or $200Gy/hr$ [229] radiation levels, compared to the defined lethal dose of $5Gy$ over 5 hours. In the Fukushima Daiichi incident, it was estimated that $8.4kg$ of caesium-137 has entered the ocean [230, 231], and due to strong currents in the region has been spread throughout the Pacific region [232, 233, 234].

From Diagnostic procedures: Medical imaging is one of the leading sources of increased background radiation with the global average being $0.6mSv/annum$. This varies from country to country, being as high as $3mSv$ in the USA [235]. With almost 70 million scans done annually in the US, this is the leading source of ionizing radiation for the general public [236] with an adult

Table 3.5: Effective dose from Medical Procedures[239]

Region	Procedure	Approximate Effective Dose	Comparable to Natural Background radiation for
Abdomen			
	CT - Abdomen + Pelvis	10 mSv	3 years
	CT-Colonography	6 mSv	2 years
	Barium Enema	8 mSv	3 years
Bone			
	X-ray of Spine	1.5 mSv	6 months
	Xray of hand/foot	0.001 mSv	3 hours
Head			
	CT - Head	1.5 mSv	6 months
	CT - Spine	6 mSv	2 years
Chest			
	CT - Chest	7 mSv	2 years
	CT - Lung screening	1.5 mSv	6 months
	X-ray of Chest	0.1 mSv	10 days
	Mammography	0.4 mSv	7 weeks
Medicine			
	PET-CT	25 mSv	8 years

receiving an effective dose of 20 μSv from a chest X-ray [237] and $5-10$ μSv from a dental X-ray [238]. Table 3.5 lists some of the medical imaging procedures and the approximate effective dose received by an adult during that procedure [239].

3.6.2 Effect of Low-level Radiation

The biological effects of radiation have been extensively studied and one can find a number of works in literature [240, 241, 242, 243, 244]. For example, we know that when the whole body or a large part of it is exposed to a high dose (on the order of $0.3-0.7$ Gy) of external radiation in a very short amount of time it may lead to Acute Radiation Syndrome (ARS). It is also known as radiation toxicity or radiation sickness. It results in the destruction of the bone marrow, the gastrointestinal tract, or the cardiovascular and the central nervous system [245]. While the effect of large doses of radiation is clear, as they produce prominent effects, the effects of low-dose radiation, usually less than 100 mGy, is difficult to ascertain. This difficulty stems from the fact that this low dose is very close to the natural background radiation levels and it is difficult to resolve the small consequences from naturally occurring effects. The frequency with which these effects take place is very low thus making it difficult to study. It has been seen that exposure from low-dose radiation may produce

1. radiation-induced gene mutation [246, 247, 248],
2. neoplastic diseases like radiation-induced leukemia, thyroid tumors and lesions of skin [249, 250, 251],
3. affect the growth of fetus and young children [252, 253, 254, 255],
4. premature aging [256, 257, 258],
5. cataracts.

The adverse effects of low-dose radiation may be characterized as stochastic and non-stochastic effects according to the NCPR [199]. For the stochastic processes, the amount of absorbed dose does not correlate to the severity of the condition. Development of cancer or genetic effects falls under this category. For non-stochastic processes, the effect increases in severity with the increase in absorbed dose, like cases of organ atrophy, fibrosis, lens opacification, decrease in sperm count, and blood changes. For the stochastic category, it is not possible to define a threshold dose as these do not depend on the amount of exposure. On the other hand, we can set a threshold limit for the non-stochastic effects so that serious health impairing is preventable. However, to err on the safer side, it is assumed that the dose-risk relationship is linear and that there is no minimum threshold. That is, exposure to any amount of radiation is dangerous. Thus, at workplaces which involve radiation, the exposure is kept As Low As Reasonably Achievable (ALARA).

The origin of linear no-threshold model: Historically, the harmful effects of radiation were discovered soon after the discovery of X-rays and radioactivity. It was known that exposure to X-rays and radiation causes cancer [259, 260] and genetic mutation [261]. Most of these early experiments used high doses of radiation and, thus, it was concluded that there was no threshold level of dose, exposure below which could be deemed safe [262]. As it is difficult to perform conclusive experiments on the effects of low-dose radiation, there were some studies that suggested that there may be benefits of Low-dose radiation [263]. The interest in the effect of radiation on biological cells became more intense after the atomic bombs were dropped on Hiroshima and Nagasaki in 1945 [264]. While there could have been other sources of carcinogenic material that could have affected the survivors of the atomic bomb, they were ignored in this study. Concept of the maximum permissible dose was introduced by the NCRP in 1954 and in 1958, UNSCEAR presented the linear no-threshold model to UN [265, 134]. It was noted that there was no data to support the low-dose data points

Table 3.6: Recommendations of the National Council of Radiation Protection and Measurements Report no. 116[200]

Exposure Type	**Acceptable Dose**
A. Occupational Exposure	
1. Effective dose limits	
a) Annual	50 mSv
b) Cumulative	10 $mSv \times age$
2. Equivalent dose annual limits for tissues and Organs	
a) Eye Lens	150 mSv
b) Skin, hands, feet	500 mSv
B.Public Exposures (annual)	
1. Effective dose limit, continuous, or frequent exposures	1 mSv
2. Effective dose limit, infrequent exposures	5 mSv
3. Equivalent dose limits for tissues and organs	
a) Eye Lens	15 mSv
b) Skin, hand, and feet	50 mSv
4. Remedial action for natural sources	
a) Effective dose (excluding radon)	> 5 mSv
b) Exposure to radon decay products	$> 7 \times 10^{-3} Jh/m^3$
C. Education and training exposures(annual)	
1. Effective dose limit	1 mSv
2. Equivalent dose limit for tissues and organs	
a) Eye lens	15 mSv
b) Skin, hand, and feet	50 mSv
D. Embryo-fetus exposures (monthly)	
1. Equivalent dose limit	0.5 mSv
E. Negligible individual dose (annual)	0.01 mSv

[266]. Nevertheless, the concept of ALARA, was introduced to maintain safe working conditions and was quickly adopted globally [259] within a decade. Even though no evidence was found to support damaging effects from low-dose radiation, the linear no-threshold (LNT) model was accepted by the National Academy of Science in 1972 on practical safety grounds [266].

The scientific community is actively debating on the effects of low-dose radiation on humans and mammals. There have been a lot of studies which suggest that the LNT model does not hold at lower doses [267, 268, 269, 270, 271]. Recent studies among populations that are exposed to higher levels of background radiation showed lower instances of Cancer in this population compared to groups that received less background radiation [272, 273, 274, 275, 276]. Studies on the population that was exposed to the fallout following the incident at Chernobyl suggest that a simple model like the LNT cannot explain its results, especially the effect of radiation on the neurological damage to the fetuses [133, 277, 278, 132, 279]. There were also studies which suggested a linear relationship between dose and risk [280, 281] and others which suggest a non-linear relationship [282]. There are also some studies which support the threshold model [283] which was later disproved [284]. There are also reports of non-cancerous effects of low-dose background radiation [285, 286]. A number of organizations have moved away from the LNT model. In 2005, the *Académie des Sciences* and *Académie Nationale de Médecine* of France rejected the LNT model [287, 288]. The Health Physics Society has also revised its statement [289]. The American nuclear Society now states that more research is required on the LNT and before any adjustments can be made to radiation protection guidelines [290]. Despite the above research, the regulatory agencies are not ready to renounce the LNT model as they feel that there is not enough data to clearly determine the effects of low-dose ionizing radiation on human cells. Population studies are difficult as a lot of people must be involved to conduct a better study and there are several factors that may influence the outcome of the experiment. The benefits from low-dose ionizing radiation should also exceed the potential detrimental effects [266, 291, 292] to reject the LNT model. Thus there is a need for controlled experiments to study the effects of low-dose ionizing radiation to once and for all clear the air on this issue.

Chapter 4

New Operating Modes for the RGS

Stereotactic Radiosurgery (SRS) is being used for the treatment of intracranial and extracranial benign and malignant tumors, vascular malformations and functional disorders of the brain that operates by focusing high-intensity ionizing radiation on a very small area [293]. It is a non-invasive procedure which uses focused narrow beams of highly intense radiation to destroy intracranial tissues or lesions that are either unsuitable or inaccessible for open surgery [294]. The term radiosurgery was coined by the Swedish neurosurgeon Lars Leksell, who had pioneered stereotaxy — a method for locating points within the brain using an external, three-dimensional frame of reference [295, 296]. The use of ionizing radiation was considered for this purpose since the nineteen fifties with X-rays and proton beams initially used to test the idea [297, 298]. He is considered the father of radiosurgery and the inventor of the Gamma Knife [299]. The first procedure with the Gamma Knife was performed in 1967 [300].

The Gamma knife is currently the most popular device for radiosurgery with over one million patients treated so far and an estimated eighty thousand patients treated globally per year [301]. The first gamma knife consisted of 179 source bodies containing cobalt-60 arranged in a hemispherical arc [302]. The beams from these sources are confocal and are collimated using a collimator helmet that the patient wears around their head. This helmet is attached to a stereotactic frame that helps in selecting the region to be treated. An illustration is shown in the figure below. [Fig of Scheme of GK] Over time, the gamma knife has evolved with different numbers of sources, different position of sources, and sources that can move relative to their initial position. All of them work on the same underlying principle4.

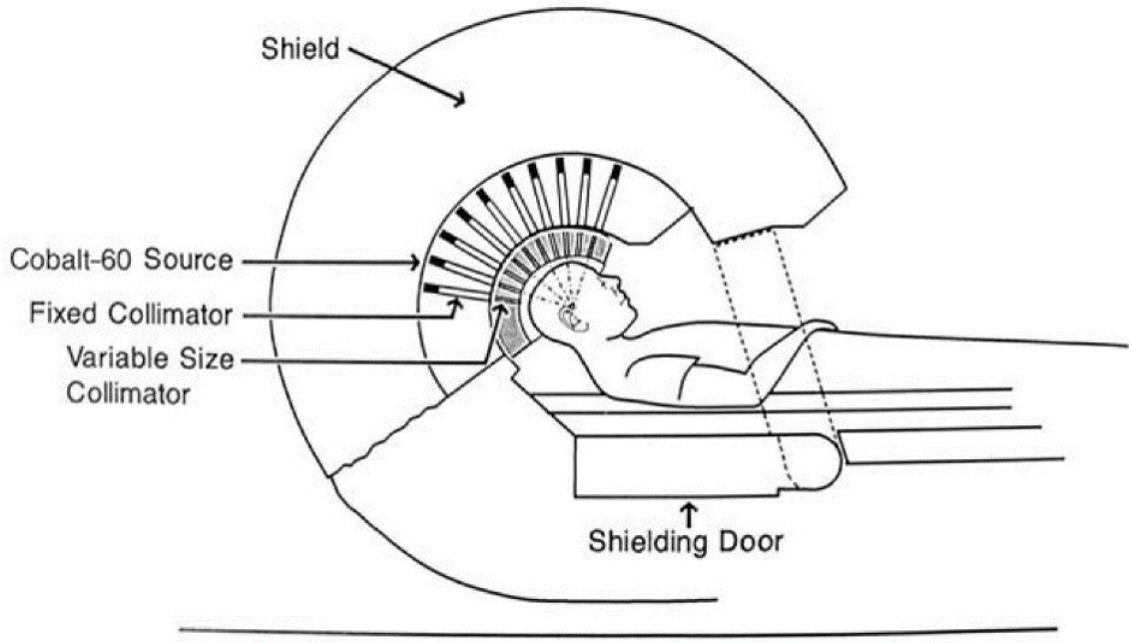

Figure 4.1: Schematic illustration of the working principle of a Gamma Knife [303]

Rotating Gamma Systems (RGS) are a recent development in radiosurgery [126, 304]. They use 30 cobalt-60 gamma radiation sources that rotate around the long axis of the patients body. Since they rotate around the patient, they mimic an infinite number of sources when compared to the discrete pencil beams of the gamma knife [128]. A Rotating Gamma System (RGS) has 30 cobalt-60 gamma radiation sources that rotate around the long axis of the patients body [126]. The collimators are part of two concentric hemispheres that rotate synchronously around the patients body with a constant angular velocity, producing a close to spherical dose distribution at the isocenter of the device. This device is able to produce a sharp fall-off of the dose giving us a narrow penumbra. It is sometimes desirable to move away from a spherical dose distribution, especially when treating areas close to critical organs such as the brain stem or the optic nerve. Intensity modulated radiation surgery (IMRS) can deliver both high conformity and high selectivity by providing a sculpted dose avoiding critical regions nearby. The RGS has the inherent capability to operate in IMRS mode by making the hemispheres move asynchronously. While this capability has been proposed in literature [305], it is yet to be studied dosimetrically. In our work, we describe our endeavor to model the IMRS mode of operation of an RGS system currently commissioned at the Rotating Gamma Institute in Debrecen, Hungary. In following sections, we describe our experimental and modelling procedures

and establish that the RGS has IMRS capabilities. We also propose an additional mode of operation of the RGS: the speed modulated radiation surgery (SMRS). This mode will have all the dosimetric advantages of the IMRS with the added benefit of shorter time required to deliver the same dose. With these two operating modes, it is now possible for the RGS to produce dose distributions that are geometrically much different from the spherical distribution that is obtained from the regular operating mode. This will not only improve the treatment times, it would also enable the RGS to operate near critical organs at risk.

4.1 The Rotating Gamma System

The Rotating Gamma Institute at Debrecen in Hungary has a RGS Vertex 360$^{\mathrm{TM}}$by American Radiosurgery Inc. in operation since 2007. Its geometry and design are similar to the instrument reported by Goetsch et al [126]. It consists of a hemispherical shell made of cast iron, which contains the 30 source bodies that houses the cobalt-60 sources and performs the primary collimation. The sources are placed in one sector with latitude angles ranging from 14.3^o to 52^o sector angle 72^o (Fig. 4.1). Another co-centric hemisphere houses the secondary collimators, which gives the emerging beams their final shapes: beam widths of 4 mm, 8 mm, 14 mm and 18 mm. An extra set of collimators are filled with tungsten plugs to block any radiation when the device is not in operation. This is the devices home position. Together, the two concentric hemispheres rotate in synchrony around the patients body with a pre-set constant angular velocity, producing a close to spherical dose distribution at the isocenter of the device. The sources and collimators are present in such a way that the isocenter is 3 cm away from the geometric center of the hemispheric shells, along the axis of rotation. This enables the device to perform near the upper regions of the neck. This device also comes with a patient positioning system that has freedom to move along three axes. The Rotating Gamma Institute at Debrecen in Hungary has an RGS Vertex 360$^{\mathrm{TM}}$by American Radiosurgery Inc. in operation since 2007. Its geometry and design are similar to the instrument reported by Goetsch et al [126]. It consists of a hemispherical shell made of cast iron, which contains the 30 source bodies that houses the cobalt-60 sources and performs the primary collimation. The sources are placed in one sector with latitude angles ranging from 14.3^o to 52^o sector angle 72^o. Another co-centric hemisphere houses the secondary collimators, which gives the emerging beams their final shapes: beam widths of 4 mm, 8 mm, 14 mm and 18 mm. An extra set of collimators are filled

with tungsten plugs to block any radiation when the device is not in operation. This is the devices home position. Together, the two concentric hemispheres rotate in synchrony around the patients body with a pre-set constant angular velocity, producing a close to spherical dose distribution at the isocenter of the device. The sources and collimators are present in such a way that the isocenter is 3 *cm* away from the geometric center of the hemispheric shells, along the axis of rotation. This enables the device to perform near the upper regions of the neck. This device also comes with a patient positioning system that has freedom to move along three axes.

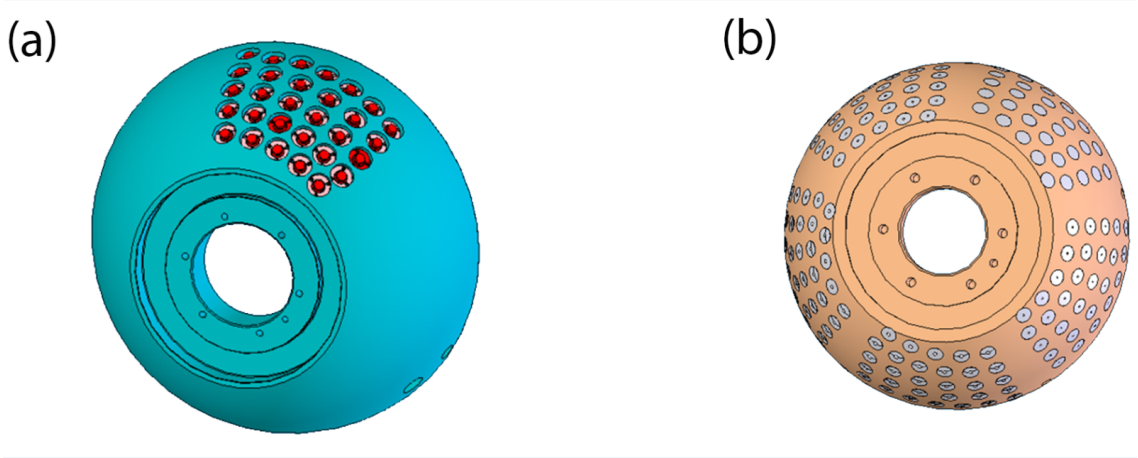

Figure 4.2: (a) The primary collimator body and (b) The secondary collimator body

4.2 Dosimetry and Proposed New Modes

4.2.1 Calibrating the RGS

To calibrate the RGS, absolute dose measurement was performed. A $3D$ pinpoint ion chamber coupled with an electrometer from PTW GmbH were used for this purpose. The ion chamber was filled with argon gas and had an active volume of 0.016 cm. cubed. Both were calibrated regularly by the manufacturer to an accuracy of 1.1. The ion chamber was placed inside a 16 *cm* water equivalent phantom and was irradiated with the 18 *mm* collimator for one minute and the absolute dose rate was inferred for this collimation setting. Ten such measurements were recorded an average value of 3.2 Gy/min was obtained. This was recorded into the treatment planning software (TPS) and was used for all experiments.

Spatial dose distribution was measured using Gafchromic EBT3 (External Beam Radiotherapy) films. A water equivalent phantom with a diameter of 16 cm was used and the films were placed at its center such that it would coincide with the isocenter of the RGS. The films were irradiated such that they receive a dose between 68 Gy with the rotational speed of the RGS varying between 14 $rpms$. The irradiated films were scanned using an Epson $V850$ pro scanner at 72 dpi, as was recommended by the manufacturer, and were evaluated using FilmQAPro to create the dosimetric distribution data.

For calibrating the films, comparison of dosimetric properties of films exposed to different pre-defined doses were used and were validated with ion chamber measurements. Measurement uncertainties were measured by comparing zero and high intensity reference films simultaneously. For the comparison of dosimetric profiles with those from simulation, data from the red channel of the RGB scanned image was use.

4.2.2 IMRS Mode of the RGS

A five-axis microcontroller governs the rotational motion of the source body and the secondary collimator. During the normal operation, both the hemispheres are rotated at a constant speed, locked at their home position. Once a collimator is selected, the micro controller changes the angular velocity to bring the required collimator in alignment with the source body, following which, both the hemispheres move in synchrony to continue delivering the dose which produces a spherical dose distribution. For a non-spherical dose distribution, we would be required to block the radiation from pre-selected directions. This can be achieved by bringing the collimator and the source body off-alignment at the regions where radiation needs to be blocked. The IMRS code was modified to allow for the IMRS operation of the RGS in compliance with the manufacturer. The treatment planning software was also modified to accommodate for the IMRS mode of operation. For studying the spatial distribution while the device is operating in IMRS mode the following angular regions were blocked: $61^o - 180^o$ and $241^o - 360^o$ and the same procedure as normal operation was followed to record the dosimetric distribution.

4.2.3 Monte Carlo Simulation

The Geant4 package was used to perform he simulations for this study. Geant4 is a Monte Carlo simulation toolkit for the simulation of passage of particles through matter [306, 307, 308, 306, 309]. It was developed to run simulations of high energy particles at $CERN$ but is also conducive in several other fields. The Palmetto cluster at Clemson University was used to take advantage of the parallel computing capabilities of Geant4.

A general particle source (GPS) was used to generate the gamma photons and setup the spectral, spatial and angular distribution similar to that of the RGS. The entire geometry of the RGS was reproduced following the blueprints that were made available to us. Native Geant4 elements such as Boolean solids and G4Polycone were used to create the geometry. The source tablets were also modelled after the manufacturer and positioned inside the source cavity, which is a hemispherical shell made of cast iron as shown in Fig. 4.3. To recreate the original machine, the GPS was programmed to generate two photons of energy: 1.33 MeV and 1.17 MeV, respectively, with angular isotropy [310] and tracked those photons that were within an angular distribution of 3 degrees to make the simulation more efficient [311]. We defined a three dimensional mesh similar to the film used in real life to get the results of our simulation. In Geant4, the scoring mesh exists in a parallel plane and does not interfere with the physical geometry within the simulation. A grid measuring 40 $mm \times 40\ mm \times 1\ mm$ was setup which was further split into $160 \times 160 \times 1$ cubic bins to record dose deposited in both Gy and MeV. Capitalizing the symmetry of the geometry, the mesh was rotated in place of the sources to further improve the efficiency of the code [311].

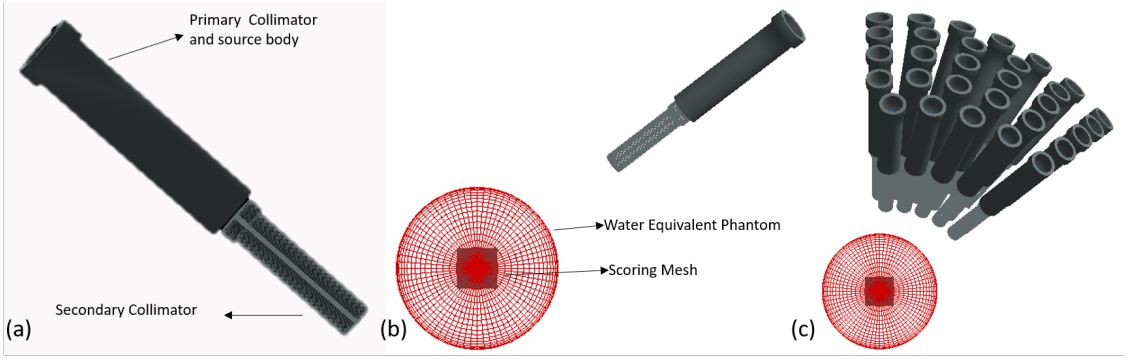

Figure 4.3: Illustration of (a) the Source along with the secondary collimator, (b) position of one source with respect to the water equivalent phantom and (c) position of all sources with respect to the phantom used in the simulation with detector at the center

A physics list suitable for medical physics applications, $QGSP\backslash BIC$ 4.0 $EM\ option3$ [312], was used. If the primary particle did not have enough energy to create a secondary particle that could travel at least 1 mm into the medium, a secondary particle is not produced and the primary particle loses energy via other modes. Thus, in Geant4, distance in place of energy, is used as a cutoff. The cutoff was set to 1 mm to further streamline the simulation. We used 3.6×10^{10} particles to model the RGS so that we could generate satisfactory statistics for evaluating the dose distributions. To validate our simulation model in Geant4, we compared experimental and simulation results from the normal mode of operation, where a spherical dose distribution was obtained. After verification of the normal mode of operation, the simulation was used to forecast the IMRS mode of operation of the RGS and compared with the experimental data. Finally, the simulation was used to predict the SMRS modality by using harmonic angle to speed functions.

4.3 Modeling Results

4.3.1 Normal Mode: Validation of the Model

Under the normal operating mode, the RGS produces approximately spherical dose distributions at the isocenter. To check the accuracy of the model, dose profiles and penumbrae were compared for dose delivered inside the water phantom. The measurements were made with the film in the X-Y position in a plane which is perpendicular to the patients axis. Comparison of the measured simulation and experimental data can be found in Fig. 4.4.

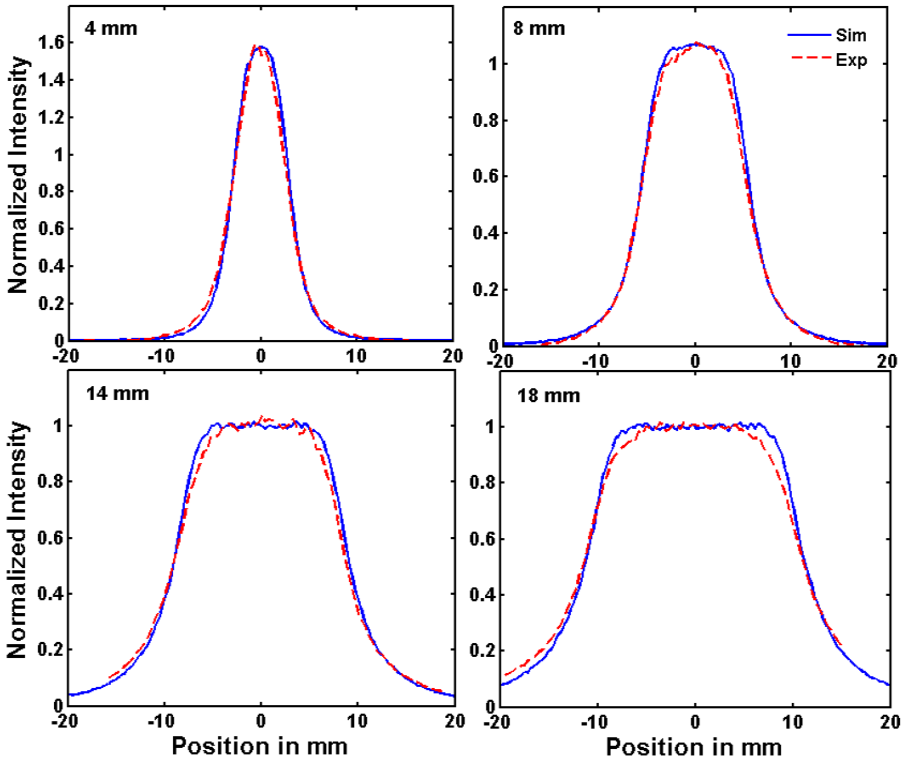

Figure 4.4: Profile comparison of the simulation and the experimental data of the X-axis of the XY plane for the four collimator sizes of the RGS; a: 4 mm, b: 8 mm, c: 14 mm, and d: 18mm

As we can see, the profile appears similar to previous simulation works in literature [128, 129]. The penumbra width was calculated after Kubo *et al* [127]. Table below lists the comparison of penumbra width at 90% and 50% intensities. We can clearly see that the agreement is close for the 4 and 8 *mm* collimator configurations. The profiles closely match near the region with 50% width. The experimental profile falls off faster near the top causing relatively larger changes in the values of the penumbra. A comparison of our work with previously published data is shown in Fig. 4.5.

Collimator Size	Experiment (mm)			Simulation (mm)		
	90%	50%	Penumbra	90%	50%	Penumbra
4	2.82	6.02	1.6	3.12	6.21	1.55
8	6.54	11.11	2.13	7.31	11.53	2.11
14	12.26	17.61	2.68	13.59	18.62	2.14
18	15.83	22.16	3.17	17.26	22.83	2.79

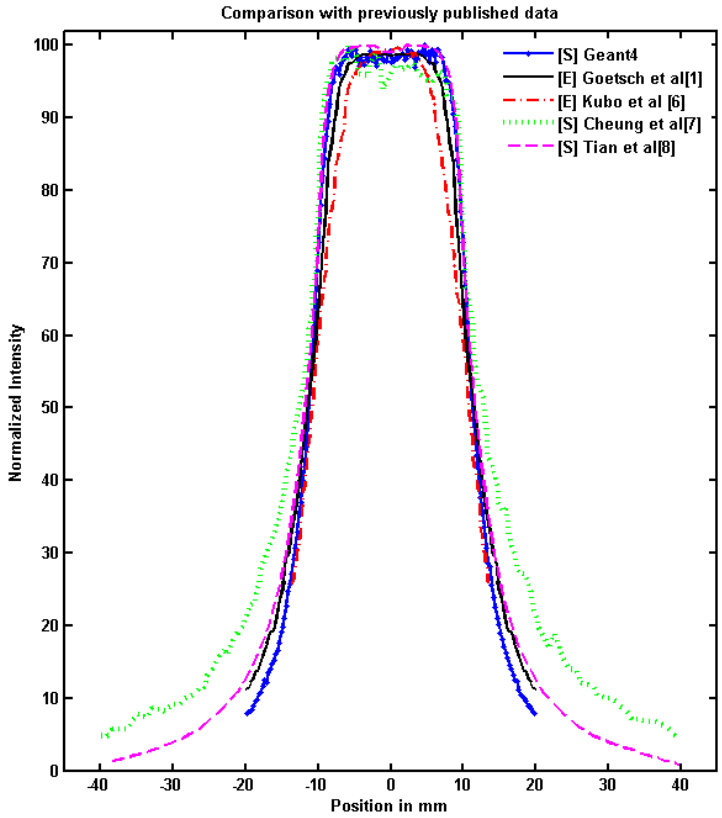

Figure 4.5: Comparison of X profiles of different RGS devices and their simulation. [S] represents simulation data and [E] represents experimental data

simulation results show a good agreement with those from the experiment, except for the device at UC Davis, which was modified onsite as described by Kubo *et al* [127].

4.3.2 Intensity Modulation

As explained before, the IMRS mode of operation included radiations blocked from the following angles: 61180 and 241360. The dose distribution was now an ellipsoid, deviating far from the spherical distribution obtained under normal mode of operation.

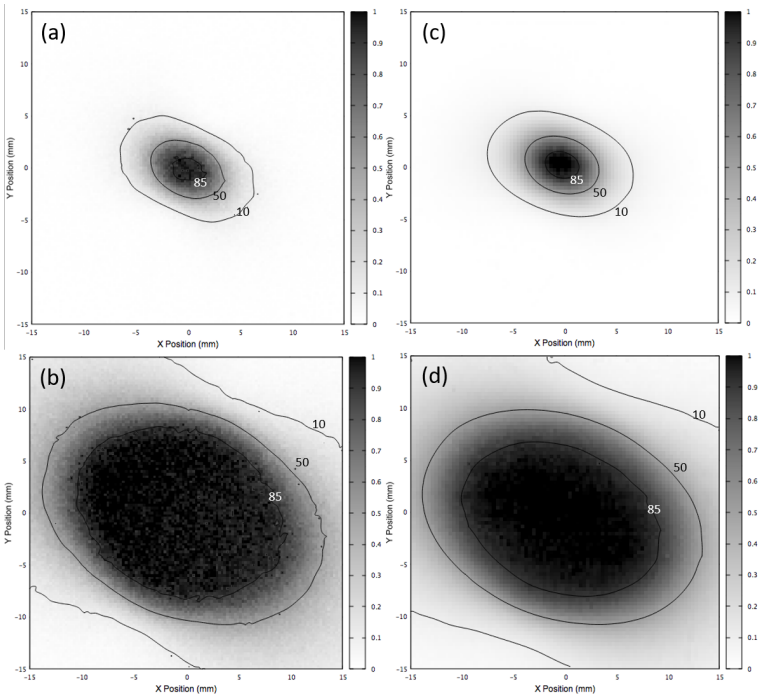

Figure 4.6: Intensity Modulated Radio Surgery (IMRS) mode of RGS comparing the dose delivered by the 4 mm and the 18mm Collimator between the Simulation (a), (b) and Experiment (c), (d)

A comparison of dose profiles is shown below.

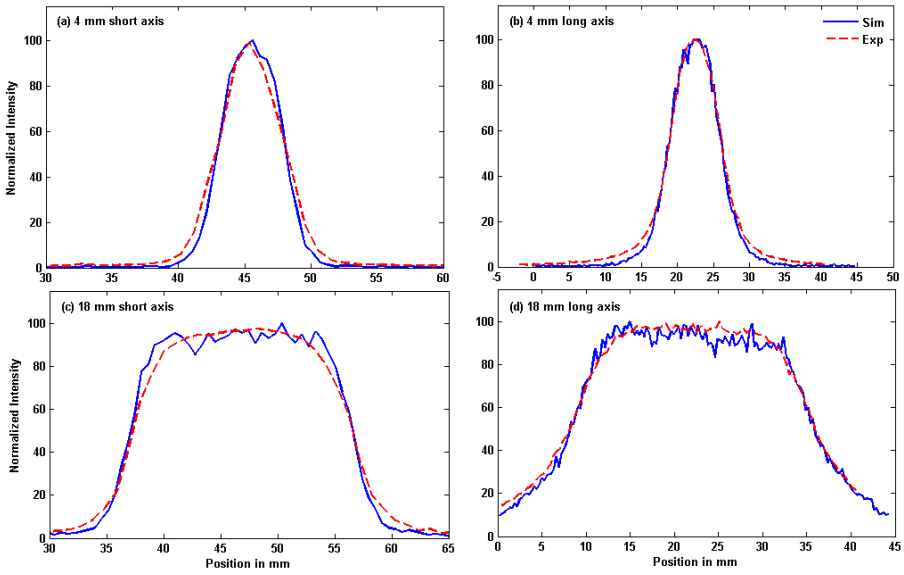

Figure 4.7: Profile comparison along the short and long axis for the intensity modulated operation in 4 mm (a), (b) and 18 mm (c), (d) configuration

The profile falls sharper along the directions which were blocked compared to the unblocked direction as can be seen in Fig. 4.6.

4.3.3 Speed Modulation

One disadvantage of the IMRS mode is that the radiation sources are off while they travel through the blocked regions. This results in a longer time to deliver the same dose when compared to normal operating mode. More angles blocked will result in even larger time to deliver the dose and in the above case, itd take 3 times longer to deliver the same dose which might make it unusable for cases requiring high doses. To overcome this difficulty, we propose the speed modulated radiosurgery (SMRS) mode. Rather than blocking radiation from directions it is not required, we propose to alter the speed of the radiation head in that region. The results are shown below for angular speeds that were a function of the angle around the patient.

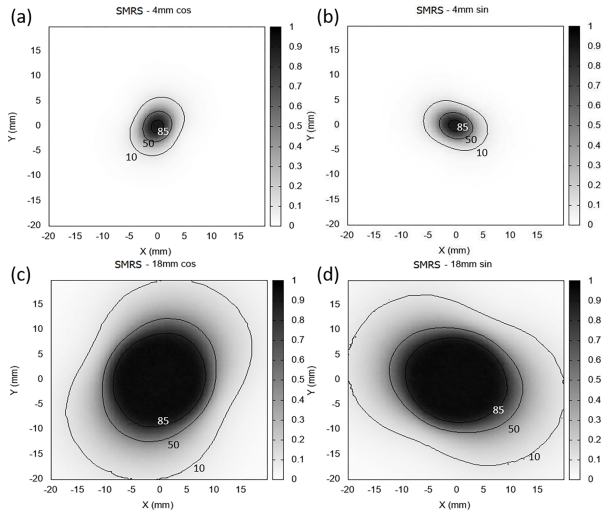

Figure 4.8: Simulation of Speed Modulated Radio Surgery (SMRS) mode of RGS. (a) and (c) show cosine modulation while (b) and (d) show sine modulation of the angles for 4 mm and 18 mm sizes of the collimator

The rotational speed of the collimators were a sine function for cases represented in Fig. 4.8 (a) and (c) and it was a cosine function in Fig. 4.8 (b) and (d). The dose distribution is similar to the IMRS mode of RGS and a comparison of the dose distribution along the major and minor axis is illustrated in Fig. 4.9 with the comparison of the penumbras shown in the following table.

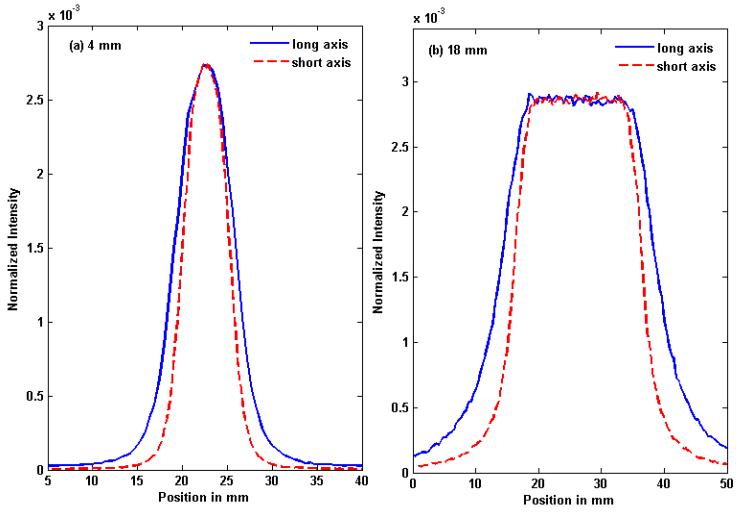

Figure 4.9: Profile comparison along the short and long axis for the speed modulated operation in (a) 4 mm and (b) 18 mm configuration

The comparison of profiles from the 4 mm collimator and the 18 mm collimator are shown in Fig. 4.9 (a) and (b) respectively.

4.4 Conclusion: Novel Operating Modes Of The RGS Introduced

In certain clinical cases it becomes perilous and impossible to perform radiosurgery to treat various lesions near critical organs and areas. While the blocked angle mode has been tested and proven effective to treat such cases for Gamma Knife [313], the same has not been done for the RGS. This work presents the first such systematic study on a RGS and presents two new possible working modes: the IMRS and the SMRS. First, our model was validated by comparing the results with the experimental dose profiles as can be seen in figure 3 and table 1 and our results are a closer

Collimator		IMRS (mm)			SMRS (mm)		
Size	Axis	90%	50%	Penumbra	90%	50%	Penumbra
4	Long	3.9	7.59	1.85	3.62	7.88	2.13
	Short	2.33	4.9	1.29	2.34	5.2	1.44
18	Long	20.31	27.59	3.64	19.85	27.61	3.87
	Short	16.03	19.33	1.52	15.98	19.21	1.61

match than previously published results. With the IMRS mode, it is possible to produce sharper dose fall off near critical organs at risk at an expense of increased time to deliver the dose. This can be overcome by operating in the SMRS mode which has similar dose fall-off but does not require longer time to deliver the dose. It is to be noted that the function used in SMRS in this work was chosen such that the results could be compared with the IMRS mode. Other intricate functions for orbital speed could be chosen to optimize tissue sparring, conformity, selectivity, target coverage and treatment times.

Chapter 5

Study the Effect of Low Dose Radiation on Cells

Low dose x-ray radiation is at once fairly common in everyday life and poorly understood in terms of its effects on the human body. Exposure to small amounts of x-rays can come from many sources including natural background radiation, cosmic radiation, disaster spill-out, diagnostic devices, and therapeutic devices. Within the scientific community, there is increasing concern for the possible dangers associated with cumulative exposure to these low dose sources [314, 315, 316] leading to assessment of carcinogenic risks [317] and safety studies from regulatory entities [318, 319, 320]. Medical imaging is of particular interest as its widespread use in the U.S. has reached approximately 70 million scans a year [236]. Such research also has applications in space travel as other recent experiments indicate potential long-term effects of exposure in space [321, 322].

The study of biological systems is challenging due to the large number of variables, time-varying feedback mechanisms, and initial conditions that need be considered to identify causation for any outcome. For instance, low dose experiments on cell samples have shown considerable variation in results with different cell types, radiation sources, and doses [323, 324, 325, 326, 327]. Some such studies suggest a threshold dose ($< 0.1\ Gy$) below which there is no cell response [323, 324]. Others dispute the claim that the effects are harmful, showing positive effects on a number of cell types and animal models [325, 326, 327]. Yet, many of these experiments lack sufficient and necessary information on experimental conditions affecting their reproducibility and dose determination —

Figure 5.1: Unconventional operation of a LINAC to accommodate the irradiation of cells. The cell cultures were placed 4.5 m away from the isocenter of the isocenter [328] near the wall of the room.

dose rate, radiation type, applied filters, geometry of both experiment and sample within sample container, and environmental conditions.

A major challenge in the study of the effect of low-dose radiation on cells is the setup used. In most of the aforementioned studies, the setup used to conduct these studies was from a clinic which is designed for treating patients. These devices use completely different energy beams, usually in the megavoltage range, during their regular operation. This makes them unsuitable for the study and the researcher is forced to resort to use of unconventional methods 5.1 to obtain dose rates identical to those that are due to natural sources of low-dose radiation. Most devices for therapy or diagnosis in the clinic have an extended source which is calibrated for dosage and heavy collimation or shielding is required to deliver a low-dose or low dose-rate. This again leads to added error margins in dose and dose-rate calculations. In most of these studies, the actual dose values received by the cell cultures are left obscure only, stating the dose received by the entire sample which includes both the cell culture and the nutritious media. Thus, the results on the effect of low-dose radiation from these experiments lose their merit. Due to these challenges, it was also impossible to study the effect of dose-rate and the energy of the beam on living cells in any of the prior studies.

For the purpose of analyzing the effects of low dose x-ray radiation on cell and tissue samples in a controlled environment, at the Medical Physics Lab of Clemson University we have designed, installed and tested an irradiator apparatus compatible with a commercial biological incubator. It makes use of the strong, quasi-monochromatic characteristic radiation produced by various exchangeable fluorescent plates upon interaction with bremsstrahlung x-rays to deliver a desired dose

to a small sample container. The irradiator setup — including bremsstrahlung source, fluorescent plate, sample container, and solid state detector — is shielded by a thick steel box and housed within the incubator. The single-photon counting detector provides continuous monitoring of x-rays incident on the sample while the incubator allows control of environmental conditions, increasing cell longevity to a maximum of 72 hours. These features and the preliminary geometrical, physical, and spectral calibrations result in well-characterized, reproducible experimental conditions.

As proof of concept, an experiment was performed observing the effects of a 2 mGy dose using characteristic x-rays of iron, copper, and calcium on the proliferation of rat vascular smooth muscle cells (VSMC). All irradiated samples showed proliferation greater than the control group at 48 hours post-treatment, but the degree of increase was spectrum-dependent with irons characteristic x-rays showing the most dramatic effect. The data obtained provide a positive proof of concept for the irradiation setup as well as a promising avenue of future bio-radiation research.

5.1 Radiation-Safe Cabinet

As previously mentioned, the irradiator setup consists of an x-ray fluorescence tube, fluorescent plate, sample container, and solid state detector. The x-ray tube has a power rating of 4 W and has maximum voltage and electron current of 50 kV and 40 μA respectively [329]. As illustrated in Fig. 5.2, the source is installed at an angle with respect to the target plate mount below. The nose of the x-ray tube is encased in a 4.44 cm wide solid steel cube to shield all but the target plate — ensuring that the only radiation incident on the sample container and detector is the quasi-monochromatic characteristic radiation the plate produces.

The target mount measures 10.3 $cm \times 10\ cm \times 3\ cm$ and is attached to a pivot point. Plates of various metallic composition may be used to provide characteristic x-rays. It is possible to paint or glue non-metallic elements onto the target in a thick enough layer to fully absorb incident bremmstrahlung radiation as well.

The sample holder located above the target mount was designed with a commercially-available self-assembled high-density polyethylene (HDPE) cup [330] in mind to contain samples. This container has a 6μm Mylar foil bottom to reduce x-ray attenuation before the radiation reaches the sample. In contrast to standard cell culture dishes, low-energy x-rays will pass through the Mylar relatively unimpeded and the very slight attenuation can be accounted for in dose calculations. To

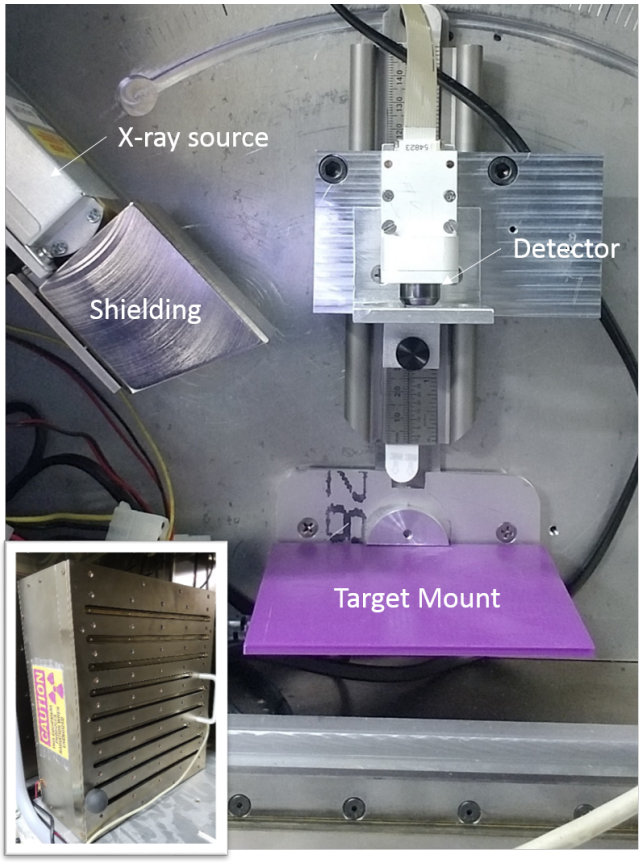

Figure 5.2: X-ray fluorescence source and the detector arrangement inside the cabinet. The detector is placed in the position of the biological sample for calibration.; Inset: The radiation box from outside showing the shielded opening slots.

aid in calibrations, the sample holder is fixed to a pivot point allowing for angular rotation, θ, with respect to the target mount and it is attached to rails to adjust distance from the mount $\vec{r}$. A protractor and ruler are built in for simplicity and accuracy of measurement.

The detector is a single photon counting Si-PIN diode detector that provides continuous monitoring during calibration and experiment [331]. For calibration purposes, the detector is placed in the sample holder for accurate determination of the amount of radiation reaching the sample during the subsequent experiment. During experiments, the detector is positioned 10 degree clockwise from the sample.

The incubator housing the irradiator cabinet allows for accurate temperature, humidity, and CO_2 composition monitoring and control without modification to the commercial design [332]. The custom irradiator cabinet consists of stainless-steel sheets 6 mm thick and has external dimensions

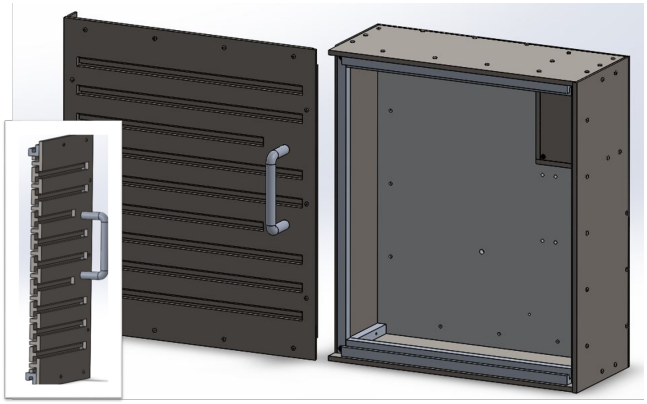

Figure 5.3: Illustration of the radiation safety box and the sliding door with the opening slots. Inset: a cut-out view of the radiation leak-proof door

of 42 $cm \times 36.8\ cm \times 15.7\ cm$. As seen in Fig, 5.3, radiation-safe slots on the front side sliding door expose the interior to the incubators internal atmosphere while maintaining radiation shielding. A PCIe slot fan is installed in a slit on top of the cabinet to aid in cooling the x-ray tube and maintaining desired atmospheric conditions. A secondary x-ray tube cooling fan is affixed below the tube with displacement brackets. In the upper right corner of the cabinet, there is a junction box that shields all cable connectors and external ports to prevent leaks.

5.2 Calibration of Source and Data Collection

First in the calibration process, a geometrical survey of fluorescent plate radiation was done with the x-ray tube voltage and current set at 15 keV and 75 μA respectively. The detector recorded single photon counts to obtain a spectrum. A copper fluorescent plate was used as the characteristic $Cu\ K_\alpha$ peak is easily identifiable. To determine the spatial dependence of the radiation field, the detector was fixed at distances from 10.1 cm to 13.1 cm in 1 cm increments. Detector position was then varied 20 *degree* on either side of the vertical in 2 *degree* increments. The resulting plot of $Cu\ K_\alpha$ peak intensity is shown in Fig. 5.4. As expected, it is evident that the field has no significant angular dependency, but there is a dependence on distance from the fluorescent plate.

To determine the energy associated with the photons detected and thereby the characteristic peaks, an energy calibration was performed using the known characteristic K peaks of copper, iron, nickel, and argon. Detected peaks were fitted with Gaussian functions of the pulse height

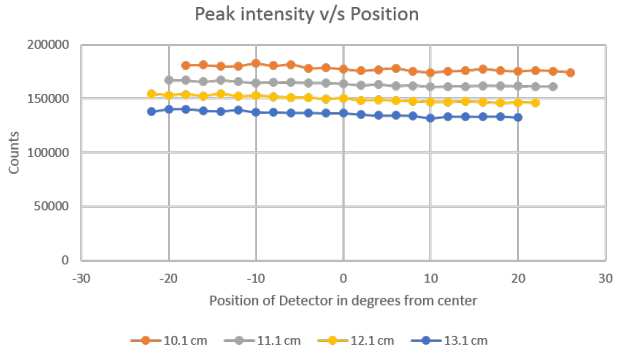

Figure 5.4: Intensity of the Cu K_α peak as a function of the detector's position

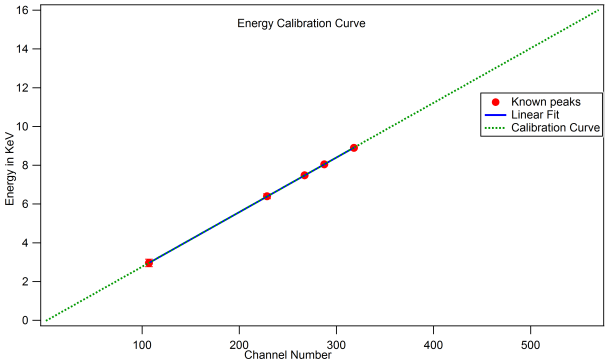

Figure 5.5: Energy calibration curve of the Si-PIN diode detector based on known K transition lines

distribution and peak position parameters were used to assign channel positions culminating in the calibration curve and spectrum seen in Figs. 5.5 and 5.6 for copper. The spectrum shows small contributions from scattered bremsstrahlung x-rays from the x-ray tube and characteristic x-rays from the surrounding surfaces, but it is dominated by the K_α and K_β peaks of Cu and Ni.

The total energy absorbed by the sample is determined by multiplying the number of photons in each calibrated channel by the x-ray energy associated with that channel. The number and energy of the counted photons are the basis for the dose rate and absorbed dose calculation. The uncertainty of the photon count in any channel is assumed to be the square root of that photon count as the detection method is a single photon count method.

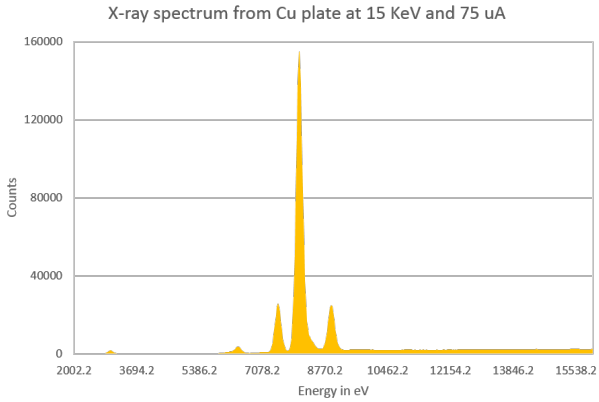

Figure 5.6: X-rays spectrum obtained using a copper plate with the detector in the position of the biological sample. A third order polynomial can approximate the small bremsstrahlung background radiation reaching the detector in this range.

The absorbed dose is defined as the expectation value of energy imparted to the matter per unit mass at a point [333]. However, there are several correction factors that must be accounted for as well. Such factors include photon absorption in other media, the dead-time of the detector, the detector surface area, the thickness of the cell culture medium, and indirect effects from x-ray absorption by the cell culture medium. Transmission rates for each medium encountered between the fluorescent plate and detector must be considered to establish the true number of photons emitted by the plate. The x-ray energy-dependent transmission coefficients were found from the mass absorption coefficients in a standard reference table, Table 5.1 [334]. Before arriving at the Si absorber within the detector, the emitted photons travel through a layer of air and then through a 12.5 μm thick Be window. There is also a period of time during which the detector is incapable of registering a new photon, called the dead-time of the detector. The combination of these two factors results in the actual photon count being higher than the number detected. After ascertaining the actual photon count produced by the target plate, the amount absorbed by the sample must be calculated. From the plate to the sample holder, photons again travel through a layer of air and then through the 6 μm thick Mylar sheet of the sample container. Corrections must then be made to the mass of the cells. The mass in the dose calculation corresponds to the mass of cells with surface area equal to the detector surface area and the thickness of the cell layer, which is typically 5 μm thick. Indirect effects of irradiation such as the production of free radicals may occur in the $1-2$ cm of nutritional medium above the cell layer. The physical properties of both the cell layer

Table 5.1: The absorption coefficients at x-ray energies that correspond to the main peaks of the spectrum

Signature	Energy in KeV	12.5 um Be Window	6 um mylar Sheet	5um Water
Ar K_α	2.96	0.95019	0.89266	0.89266
Ar K_β	3.19	0.96042	0.91301	0.91301
Fe K_α	6.4	0.99543	0.98912	0.98912
Fe K_β	7.06	0.99660	0.99197	0.99197
Ni K_α	7.47	0.99713	0.99326	0.99326
Cu K_α	8.05	0.99768	0.99461	0.99461
Ni K_β	8.26	0.99784	0.99504	0.99504
W L_α	8.4	0.99794	0.99530	0.99530
Cu K_β	8.91	0.99824	0.99606	0.99606
W L_β	9.67	0.99858	0.99695	0.99695

and the nutritional medium are approximately equivalent to water.

Thus, the absorbed dose as determined by the photon count in each energy channel can be written as

$$D = \frac{\sum_{i=1}^{n} N_i \times E_i \times C_i}{M}$$

where N_i is the photon count in each channel i, E_i is the x-ray energy corresponding to the channel, M is the mass of the biological sample corresponding to the detector's surface area, and C_i represents the applicable energy-dependent correction terms. The correction terms can be written as

$$C_i = \frac{T_{i_{Air_1}} \times T_{i_{mylar}} \times [1 - T_{i_{Water}}]}{T_{i_{Be}} \times T_{i_{Air_2}}} \times C_d$$

where T_i is the transmission coefficient for photons in each medium and C_d is the correction for the detector dead time. The transmission coefficients can be calculated from the mass absorption coefficients in Table 5.1 as detailed below.

$$T_i = \exp\left(\frac{-\mu_i \times x}{\rho_i}\right)$$

where x is the thickness of the medium (beryllium, mylar, water, or air), ρ is the density of the medium, and μ_i is the mass absorption coefficient at the photon energy corresponding to channel i.

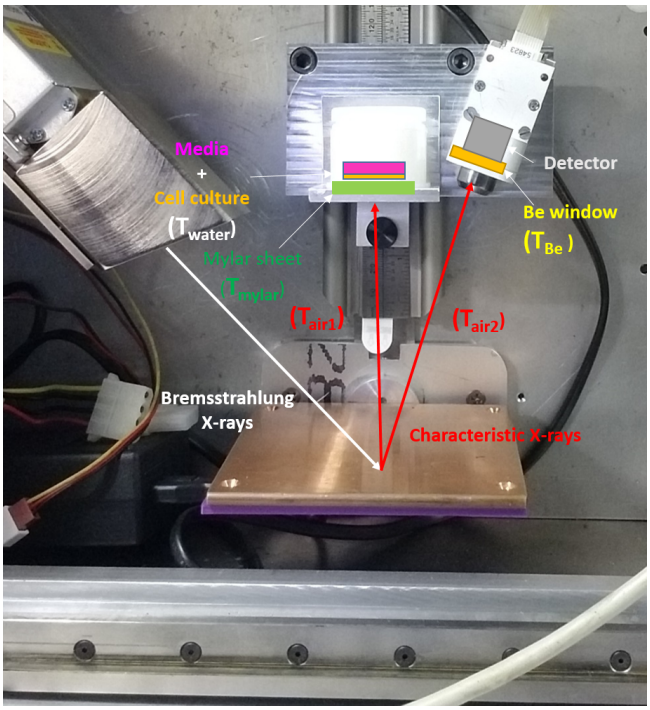

Figure 5.7: Illustration showing the propagation of x-rays and the corresponding transmission coefficients used in our calculation

The dose rate is also a useful quantity. It can be calculated by dividing the dose equation by the spectrum acquisition time. Each fluorescent plate and x-ray tube power setting combination will deliver a fixed dose rate and a desired dose can be administered by modifying the irradiation time. A sample spectrum is shown in Fig. 5.6. It was obtained with the detector in the sample container position, but placing the detector in its angled position would yield similar results. Using this method, the dose delivered per minute was found to be 6.79 $\mu Gy/min \pm 0.15\ \mu Gy/min$.

5.3 Experimental Data, Analysis, and Results

The proof of concept experiment was done on rat vascular smooth muscle cells (VSMC). Cells at a passage of 9 were plated in the sample containers. The nutritional medium consisted of 500 mL of Dulbeccos Modified Eagle Media (DMEM), 50 mL of Fetal Bovine Serum (FBS), and 10 mL of Antibiotic-Antimycotic. $100,000$ cells per Mylar cup were given 18 hours to attach prior to irradiation. Other cell types may resist attaching to the Mylar film such as cardiomyocytes, neurons, etc. For these cells or prolonged culture times, the film may need to be coated in an adherent protein (i.e., collagen) or peptide (i.e., RGD). In such cases, this layer must be accounted for in dose calculations.

In the experiment, the independent variable was the target plate material — iron, copper, and calcium. Four equal groups of cells received a 2 mGy dose — Group A with iron, Group B with copper, Group C with calcium, and Group D was left unirradiated as a control. To maintain consistent environmental conditions, all groups were stored together throughout the process.

As seen in Fig.5.7, proliferation assays were completed at 8, 24, and 48 hours post-irradiation. All proliferation assays had $n = 9$ except for the 24 hr iron which had 8 samples. Proliferation assays were also completed at 72 hours with $n = 0$ for each condition.

It should be noted that cells typically multiply at a slower rate after 36 to 48 hours due to the spatial limitations of the sample containers and all cultures reached confluence by 72 hours. For effects after 48 hr, the seed size can be reduced to $40,000$ cells. In future experiments, a collagen or fibronectic substrate is recommended to allow for better VSMC adherence as the Mylar film lacks the specific attachment moieties to allow for integrin binding.

Fig. 5.8 illustrates that every data set with the exception of 24 hr copper was statistically significant as determined by a paired Students t test where $p < .05$. The proliferation between hours

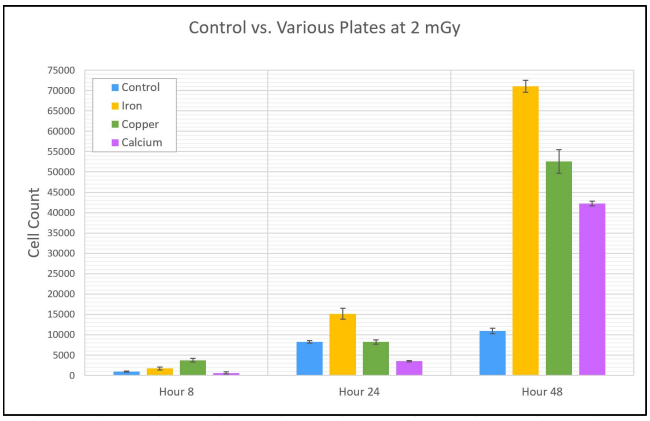

Figure 5.8: Cell response after radiation

24 and 48 is most pronounced as each irradiated group shows exponential growth compared to the control. Cell proliferation is also clearly spectrum-dependent at 48 hours and to a lesser degree $<$ 24 hours. The 2 mGy dose appears to be below the threshold to elicit apoptosis as no significant cell death was witnessed. This corroborates findings from an earlier iteration of the irradiator system where proliferation of 3T3 fibroblasts 48 hours post-irradiation with characteristic copper x-rays significantly outpaced that of the control group [335]. Future experiments to determine the influence of energy, dose rate, and cell type could be valuable as could additional tests like Polymerase Chain Reaction Analysis (PCR) to identify changes in genetic information due to irradiation.

5.4 Conclusion: Unique X-ray Irradiator Available for Research

We have designed and tested a temperature- and atmospheric- composition-controlled, radiation shielded incubator cabinet. The goal of the project was to provide a capability for the users of the device to analyze the effects of low dose x-ray radiation on biological tissues. Bremsstrahlung x-rays incident on fluorescence plates produce strong, quasi-monochromatic x-rays to irradiate tissues in a small sample container. The dose and dose-rate are highly characterized and have a low error margin. A standard mylar bottom plastic cup is used which makes it suitable to conduct experiments with a variety of cell culture types. A proof-of-principle experiment observed rat vascular smooth muscle cell proliferation after absorbing characteristic x-rays of iron, copper, and calcium.

The results show that all irradiated cells exhibit significantly increased growth compared to the control group. In this study, we investigated the effect of incident energy on the cell culture which was not possible in any prior studies. The results [Fig 5.7 bar graph] imply that the cells react to different incident energies in a contrasting manner. Investigation of the controlling mechanisms are left for future study. The experiment proves the efficacy of the apparatus and shows promise for future low dose bio-radiation analysis.

Chapter 6

Overall Conclusions and Scope for Future Work

The comparison of dose profiles from simulation and experiment show close agreement for the normal mode of operation thus validating our simulation model. The experimental value of the penumbras of the profile from the IMRS mode of operation also shows close agreement with the data obtained from our simulation. In the IMRS mode of operation, the dose modulation capability of the RGS is investigated and we see that the dose distribution is highly checked in the directions where radiation is blocked resulting in sharper penumbras. However, this mode of operation introduces a setback. Since the radiation is completely blocked, the total time to deliver the dose, that is the dose rate, is adversely affected. Our simulation of the SMRS mode suggests that dose sculpting like the IMRS mode is possible. As radiation is not completely blocked from any direction, the dose rate is not effected and treatment times stay low. With the introduction of the IMRS and the SMRS mode of operation, the RGS is now capable to treat areas near critical organs and areas at risk. With the SMRS mode, no compromise on treatment times are required.

We have designed a new setup to irradiate cells with highly-characterized, low-dose radiation to do a systematic study on the cells in a controlled environment. This setup complies with both the university and State radiation safety policies and was specifically designed keeping X-ray generation and detection in mind. Using the metal target, we are able to produce highly monochromatic X-ray radiations that will help in a systematic study. The X-ray source has a tunable capability and by

controlling the current we can control the intensity of X-ray photons produced, thereby modulating the dose delivered to the cells. An attachment is provided to accommodate live culture of cells in proper position during irradiation procedure. The ambient environment ensures that there are no external sources of stress for the cells. The setup is flexible and can accommodate tissue samples and tendons beside live cell cultures.

Our Monte Carlo simulation code was verified against experimental results. This proves the capability of our group to simulate the operation of devices that involve high intensity radiation. Now it is possible for our group to design and model radiosurgery devices with better characteristics that are capable to extending their operating capabilities to other parts of the body and near other critical organs. Although more studies are required to accommodate operational capabilities near critical regions that are in constant motion like the heart or the lung, the potential is quite promising.

With the irradiator setup, now we are able to deliver highly characterized low-dose radiation. This will help us to study the effect of low-dose radiation on cells. Due to the low output of the device, we can study scenarios to investigate for example the effect of space travel on human tissue. This will require very low doses of radiation, that were not available in our lab before. We could also tune the current going into the tube to study the effects of low-dose and low-dose-rate on the cells. The flexibility in choosing the energy of incident radiation by switching out the metal plates also gives us an opportunity to study the energy-dependence of radiation on cells.

Appendices

Appendix A

Publications

Intensity modulated operating mode of the rotating gamma system

Bishwambhar Sengupta
Department of Physics and Astronomy, Clemson University, Clemson, SC 29634, USA

Laszlo Gulyas
Rotating Gamma Institute, Debrecen H-4032, Hungary

Donald Medlin
Department of Physics and Astronomy, Clemson University, Clemson, SC 29634, USA

Tibor Koroknai, David Takacs, Gyorgy Filep, Peter Panko, and Bence Godo
Medikai Innovacio Kft, Debrecen H-4026, Hungary

Tamas Hollo
Rotating Gamma Institute, Debrecen H-4032, Hungary

Xiao Ran Zheng
Department of Physics and Astronomy, Clemson University, Clemson, SC 29634, USA

Imre Fedorcsak, Jozsef Dobai, and Laszlo Bognar
Department of Neurosurgery, University of Debrecen, Debrecen H-4032, Hungary

Endre Takacs[a)]
Department of Physics and Astronomy, Clemson University, Clemson, SC 29634, USA

(Received 5 January 2018; revised 19 February 2018; accepted for publication 6 March 2018; published 17 April 2018)

Purpose: The purpose of this work was to explore two novel operation modalities of the rotating gamma systems (RGS) that could expand its clinical application to lesions in close proximity to critical organs at risk (OAR).
Methods: The approach taken in this study consists of two components. First, a Geant4-based Monte Carlo (MC) simulation toolkit is used to model the dosimetric properties of the RGS Vertex 360™ for the normal, intensity modulated radiosurgery (IMRS), and speed modulated radiosurgery (SMRS) operation modalities. Second, the RGS Vertex 360™ at the Rotating Gamma Institute in Debrecen, Hungary is used to collect experimental data for the normal and IMRS operation modes. An ion chamber is used to record measurements of the absolute dose. The dose profiles are measured using Gafchromic EBT3 films positioned within a spherical water equivalent phantom.
Results: A strong dosimetric agreement between the measured and simulated dose profiles and penumbra was found for both the normal and IMRS operation modes for all collimator sizes (4, 8, 14, and 18 mm diameter). The simulated falloff and maximum dose regions agree better with the experimental results for the 4 and 8 mm diameter collimators. Although the falloff regions align well in the 14 and 18 mm collimators, the maximum dose regions have a larger difference. For the IMRS operation mode, the simulated and experimental dose distributions are ellipsoidal, where the short axis aligns with the blocked angles. Similarly, the simulated dose distributions for the SMRS operation mode also adopt an ellipsoidal shape, where the short axis aligns with the angles where the orbital speed is highest. For both modalities, the dose distribution is highly constrained with a sharper penumbra along the short axes.
Conclusions: Dose modulation of the RGS can be achieved with the IMRS and SMRS modes. By providing a highly constrained dose distribution with a sharp penumbra, both modes could be clinically applicable for the treatment of lesions in close proximity to critical OARs. © *2018 American Association of Physicists in Medicine* [https://doi.org/10.1002/mp.12887]

Key words: Geant4-based Monte Carlo simulation, intensity modulation, radiosurgery, rotating gamma system, speed modulation

1. INTRODUCTION

Stereotactic radiosurgery (SRS) is being used for the treatment of benign and malignant tumors, vascular malformations, and functional disorders. It employs 3D target localization to guide several finely collimated pencil radiation beams to deliver a single, precisely localized, high dose of targeted radiation. RGS Vertex 360™ rotating gamma system (RGS) apply 30 cobalt-60 gamma radiation sources that rotate around the long axis of the patient's body.[1] The

collimators are part of two concentric hemispheres that rotate in synchrony around the patient's body with a preset constant angular velocity, producing a close to spherical dose distribution at the isocenter of the device. The narrow penumbra of the machine is due to the sharp dose falloff resulting in the various entrance angles the rotation produces. The effect is comparable to the dose distribution delivered by the Gamma Knife® type devices that employ a large number of static sources.[2] Intracranial radio surgical treatments performed with various types of devices have been well documented in the literature,[2–5] but papers describing the dosimetric capabilities of the RGS-type machines are sparse.[1,6–8]

Highly accurate dose delivery representative of Gamma Knifes® and RGS devices is especially important for the treatment of cases near critical structures of the brain. Trigeminal neuralgia (TN), for example — a form of chronic, debilitating neuropathic pain — is one of the cases, where the use of these machines is desirable, but the application depends on the particular case due to the closeness of the brainstem. TN is caused by pressure on the trigeminal nerve from nearby blood vessels or tumors, by the damage of the trigeminal myelin sheath, or by nearby arteriovenous malformations.[9] If medications fail to reduce pain or lead to adverse side effects, then surgical techniques, including SRS, maybe applied.[10,11] The effective treatment of TN with SRS depends primarily on the precise delivery of a high dose of radiation, in the order of 75 to 90 Gy, to the trigeminus nerve, however, SRS can only be used for the treatment of TN when the dose spillage to the brain stem can be minimized.[12] In order to, create a sharp dose falloff (high selectivity), while depositing high dosage of radiation (high conformity) to treat TN and similar disorders near critical structures of the brain intensity modulated operation of the RGS has been proposed[13] (Intensity Modulated Radiation Surgery, IMRS).

IMRS can deliver both high selectivity and high conformity by providing a sculpted dose intensity distribution, as opposed to the spherical dose distribution. The shaping of the dose distribution can be achieved when the sources and collimators rotate asynchronously in certain angular positions to block the radiation beams at those angles. Although IMRS in connection with gamma knife[14] and various RGS devices has been proposed in the literature[13] as an intrinsic capability stemming from the rotation of the sources, this technique has not been studied dosimetrically or demonstrated in practice to date.

In this paper, we describe the efforts of the Medical Physics research group of the Department of Physics and Astronomy at Clemson University (CU) to model the IMRS operation of an RGS system in service at the Rotating Gamma Institute (RGI) in Debrecen, Hungary. In the following, we present our modeling and experimental procedures and demonstrate that adequately modified dose distributions can be produced by the IMRS operation of the RGS by blocking the radiation from certain directions. This method could potentially expand the applicability of the RGS to previously untreatable cases of trigeminal neuralgia and other similarly high-risk conditions. Results of the calculations have been compared with dosimetric measurements at RGI.

As an extension to the blocked angle IMRS mode, this paper also describes our studies of another operational modality of the RGS that could have a critical clinical impact. This modality is called Speed Modulated Radiation Surgery (SMRS) and works by modulating the rotational speed of the cobalt-60 sources with a predetermined mathematical function of the rotation angle. SMRS can produce dose distributions that are geometrically different from the spherical distribution created while operating at a constant angular velocity. The proposed SMRS modality of the RGS may increase the envelope, precision, and control of the dose distribution without compromising the penumbra achievable with IMRS with a greatly improved treatment time. This would enable the use of the RGS for cases of TN and other treatment indications in close proximity to critical tissues that the RGS could not treat otherwise.

2. MATERIALS AND METHODS

2.A. Rotating gamma system in Debrecen, Hungary

The rotating gamma system at the Rotating Gamma Institute in Hungary (RGS Vertex 360™ by American Radiosurgery Inc., San Diego, CA, USA) has been in operation since 2007. Its geometry and design are similar to the instrument reported by Goetsch et al.[1] It consists of a hemispherical shell made of cast iron, which contains the source body that houses the sources and performs the primary collimation. The sources are placed in one sector with latitude angles ranging from 14.3° to 52° sector angle 72° [Fig. 1(a)].

A second concentric hemispherical shell contains the secondary collimators to produce approximately spherical dose distributions with 50% width having diameters 4 mm, 8 mm, 14 mm, and 18 mm [Fig. 1(b)]. There is a fifth set of collimators in this shell, which contain tungsten plugs to block the radiation when aligned with the sources in the so-called "0" or home position. The sources and collimators are placed such that, when aligned, the intersection point of all the gamma beams is 3 cm outside from the center of the hemisphere along the axis of rotation of the shells to extend the reach of the instrument toward the upper neck region. The system incorporates a patient positioning system capable of movement along three directions.

2.B. Dosimetry of the RGS and analysis of experimental data

Absolute dose measurements were performed by a 3D pinpoint ion chamber together with an electrometer from PTW GmbH. The chamber has an active volume of 0.016 cm^3 filled with argon gas. The electrometer and the ion chamber

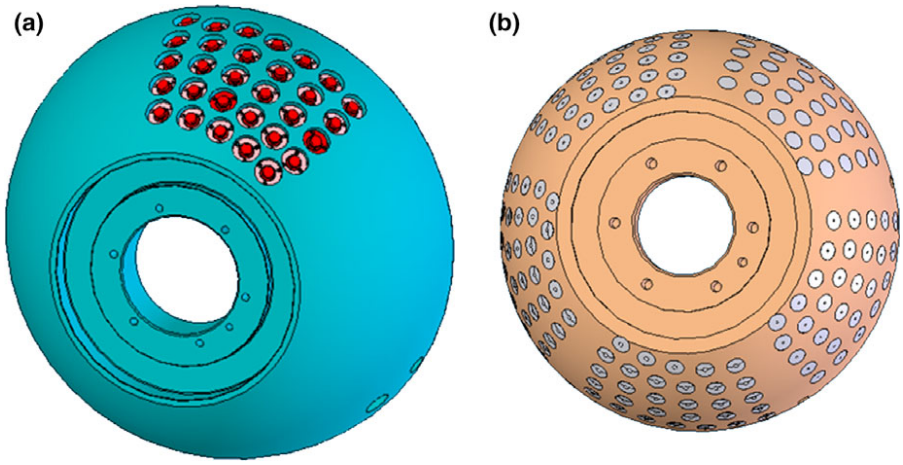

FIG. 1. (a) The primary collimator body and (b) the secondary collimator body. [Color figure can be viewed at wileyonlinelibrary.com]

were both calibrated by the manufacturer to an accuracy of 1.1%. The chamber was placed inside a 16 cm water equivalent phantom and was radiated for 1 min with the 18 mm collimator to infer the absolute dose rate achievable with this collimation. Ten independent dose rate measurements were taken with an average value of 3.2 Gy/min. This dose rate was entered into the Treatment Planning Software (TPS) and was used throughout these experiments.

In order to measure the spatial dose distribution, Gafchromic EBT3 (External Beam Radiotherapy, Ashland) films were used. The films were scanned using an Epson V850 Pro Scanner at 72 dpi resolution, as was recommended by the manufacturer. The films were placed at the center of the spherical 16 cm diameter water equivalent phantom and were positioned to the isocenter of the machine during the irradiations. The rotational speed of the RGS was between 1 and 4 rpms, and the films received a total dose between 6 and 8 Gy. The films were processed with the film evaluation software (FilmQAPro) provided by the vendor to generate the dosimetric distribution data.

Calibration of the films was performed by comparing the measured dosimetric properties obtained from films that were irradiated with predefined doses, which were validated with ionization chamber measurements. This was performed sequentially for six strips of film. For each measurement, scans of zero intensity and high-intensity reference films were also taken simultaneously to account for the measurement uncertainties. Data from the red channel of the scanned RGB color image were used for comparisons of the dosimetric profiles with those determined by simulation.

2.C. RGS operation in IMRS mode

The rotational motion of both the source body and the secondary collimator is controlled by a 5-axis microcontroller within the RGS's electronic control system. During normal operation, the microcontroller initially rotates both the primary and the secondary collimator bodies to their home position synchronously. The microcontroller selects the appropriate collimator by changing the angular velocity of the secondary collimator body until the desired collimator is aligned with the sources, after which both bodies are moved synchronously to maintain this alignment. These collimators

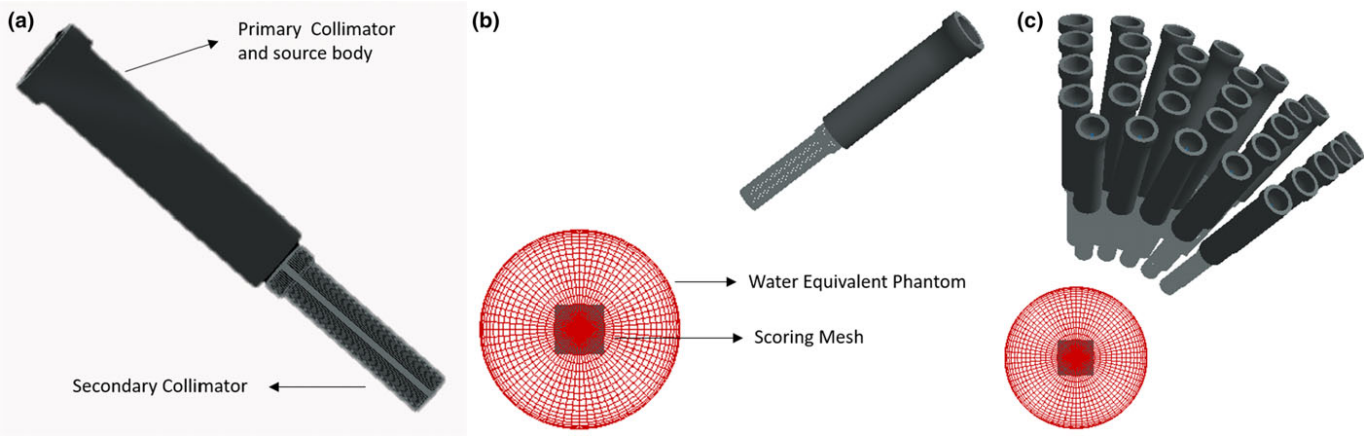

FIG. 2. Illustration of (a) the source along with the secondary collimator, (b) position of one source with respect to the water equivalent phantom, and (c) position of all sources with respect to the phantom used in the simulation with detector at the center. [Color figure can be viewed at wileyonlinelibrary.com]

are rotated around the axis of the hemispheres at a constant angular velocity, which produces a close to spherical dose distribution.

In contrast, nonspherical dose distributions can be achieved with the RGS while operating in the IMRS mode, where the radiation is blocked at preselected angular positions during the treatment. Blocking is achieved by misaligning the primary and secondary collimator bodies as they rotate through the angular regions where incoming radiation is not desired. In collaboration with the manufacturer, the microcontroller code was modified to allow for IMRS with the RGS. Modifications to the treatment planning software were also made to accommodate the IMRS mode; e.g., halting the timer whenever the radiation is blocked during the treatment to account for the proper dose delivery time.

Measurements to study the spatial dosimetric distribution of the IMRS mode were the same as described in the previous section with the angular regions between 61° and 180° and 241° and 360° blocked.

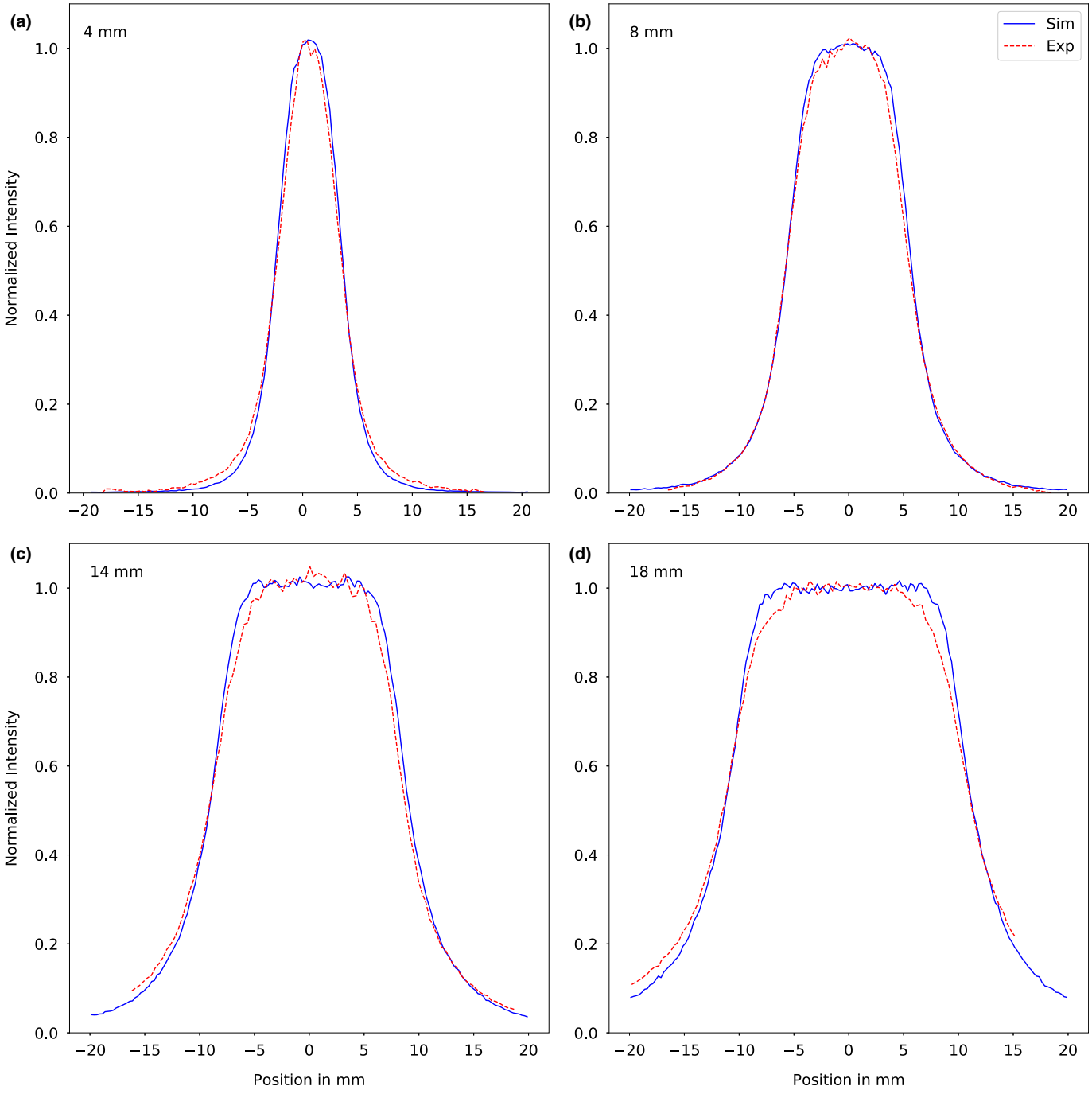

FIG. 3. Profile comparison of the simulation and the experimental data of the *X*-axis of the XY plane for the four collimator sizes of the RGS; (a) 4 mm, (b) 8 mm, (c) 14 mm, and (d) 18 mm. [Color figure can be viewed at wileyonlinelibrary.com]

2.D. Monte Carlo simulation

The simulations for this study were performed using the Geant4 simulation package, which is a Monte Carlo simulation toolkit developed and maintained by the Geant4 collaboration.[15–18] Its predecessor was developed to run simulations of high energy physics at CERN but it has also found applications in various other fields including medical physics. To reduce the simulation time, the parallel computing capabilities of the Geant4 package were taken advantage of by running it on the Palmetto Cluster of Clemson University.

Version 10.03.p01 of the Geant4 toolkit was used to for the dose calculations of the RGS. Similar to the Gamma Knife sample code provided with the toolkit, we introduced a general particle source (GPS), which defines the specifications of the spectral, spatial, and angular distribution of the primary source particles. The RGS geometry was modeled with the built-in Geant4 geometrical elements, which allows the user to specify the material, spatial position as well as the logical relations among the components. A combination of the G4Polycone class and Boolean solids worked best to precisely model the RGS geometry according to the manufacturer's design drawings.

The 30 Co-60 sources in the RGS were modeled with source cylinders of the exact same dimensions and were positioned within the source cavity inside the primary collimator made of cast iron. The secondary collimator body was positioned within the primary collimator body and the collimators were aligned with the center of the water equivalent phantom. The water equivalent phantom was placed at the center of the geometry world.

Generation of the primary particles (gamma photons) occurs inside the source capsules. The GPS allows the user to specify a volume of any dimension, location, and orientation, inside which the particles will be created. To accurately model the gamma photon generation, two GPS objects with mono-energetic distributions of energies 1.33 and 1.17 MeV[19] were generated. The primary particles were generated with an isotropic angular distribution, however, a limit of 3 degrees was placed on the θ distribution to increase the simulation's efficiency,[20] with the assumption that gamma photons leaving the source capsule in the real system outside this cone do not contribute much to the overall dose distribution at the isocenter.

Geant4 offers a command based scoring mechanism through the G4ScoringManager class. It utilizes parallel navigation in a parallel world volume, so the user can define a three-dimensional mesh and scoring independently from the physical geometry. To accurately model the Gafchromic films used to measure the experimental dose distributions, we created a scoring mesh with equivalent dimensions (40 mm × 40 mm × 1 mm) that was split into 160 × 160 × 1 cubic bins. The detectors were set to record the dose deposited in units of Gy along with the total energy in MeV. Exploiting the symmetry of device, the scoring mesh was rotated along its z-axis to model the rotation of the treatment head, which resulted in a considerable simplification of the geometry code.[20]

For tracking the photons and particles, the Reference Physics List simulation engine: QGSP\BIC 4.0 EMoption= 3 recommended for medical applications[21] was used. The primary particle loses energy by producing secondary electrons or gamma photons. In Geant4, the threshold for secondary particle production is defined in distance rather than energy. If the primary particle has insufficient energy to generate secondary particles that travel at least 1 mm into the surrounding material, then no secondary particles are produced and the primary particle loses energy due to continuous energy loss. Thus, the stopping location of the

TABLE I. Comparison of the profile widths between experiment and simulation. All penumbra values are calculated as (90% width – 50% width)/2 and are shown in mm.

	Experiment (mm)			Simulation (mm)		
Collimator size	90%	50%	Penumbra	90%	50%	Penumbra
4	2.82	6.02	1.6	3.12	6.21	1.55
8	6.54	11.11	2.13	7.31	11.53	2.11
14	12.26	17.61	2.68	13.59	18.62	2.14
18	15.83	22.16	3.17	17.26	22.83	2.79

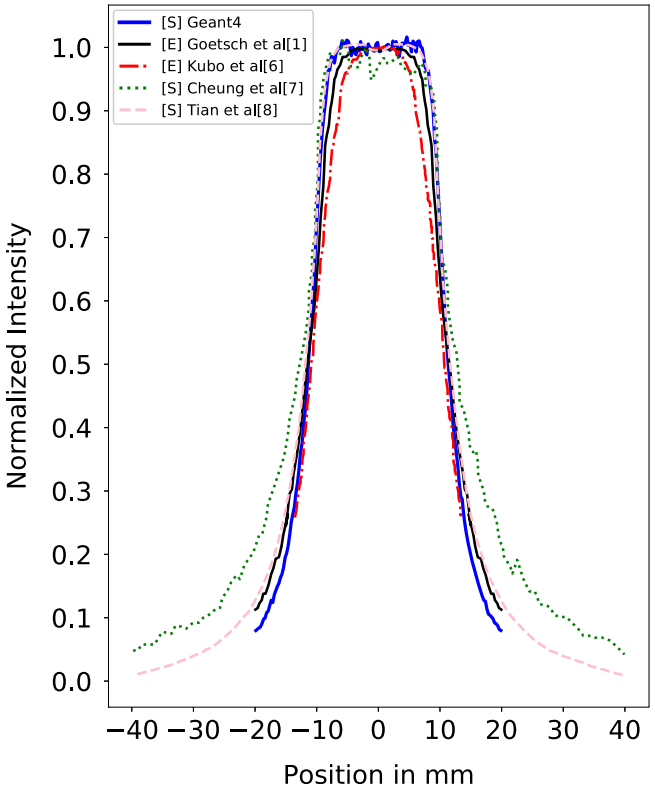

FIG. 4. Comparison of X profiles of different RGS devices and their simulation. [S] represents simulation data and [E] represents experimental data. [Color figure can be viewed at wileyonlinelibrary.com]

primary particle is accurate. This allows for the use of distance as the only parameter for the production threshold since the percentage depth dose (PDD) depends on the material. This distance was set to 1 mm after a series of experiments with different values to optimize our simulation time and provide accurate results given the statistical nature of the absorption.

Regarding the runtime, it takes approximately 3 h for an Intel®Xeon®CPUE5345 processor to run simulations with the generation of 10^7 primary particles. During the dosimetric modeling of the RGS, we generally used 3.6×10^{10} primary particles to create sufficient statistics for evaluating the dose distributions.

In order to validate the GEANT4 simulation package, we have compared the results with experimental data from the RGS during the normal operation mode, where the sources maintain a constant angular velocity and produce a close to spherical dose distribution. After validation, the simulation package was used to predict the dosimetric properties of the RGS for the IMRS operation mode and compared with experimental data. Lastly, the simulation platform was used to model the dose distribution of the RGS during the proposed SMRS modality by using harmonic angle-to-speed functions. A part of the geometry created by our code is shown in Fig. 2.

3. RESULTS

3.A. Normal operation mode of the RGS

In the normal operation mode, the RGS produces a near spherical dose distribution at the isocenter. To validate the accuracy of our simulation platform and RGS model, the simulated dose profiles and penumbrae in a water phantom were compared with those obtained experimentally for identical conditions. The dosimetric film was located in the XY plane, perpendicular to the longitudinal axis of the patient (Z), with the *Y*-axis in the vertical direction.

Comparisons of the measured and simulated results for the four collimators are shown in Fig. 3. Similar shapes near the top of the distribution have been observed in previous simulations.[7,8] The penumbra width was calculated by taking half the difference between the 90% and 50% widths, similar to Kubo et al.[6] Table I shows the tabulated values of the 50% and 90% widths for the experimental and simulated data.

As with the dose profiles, the agreement between the experimental and simulated penumbra widths are better for the 4 and 8 mm collimators compared to the 14 and 18 mm collimators. At the 50% width, the simulation and the experiment profiles closely match each other. Near the maximum dose regions, the experimental profile falls off faster causing

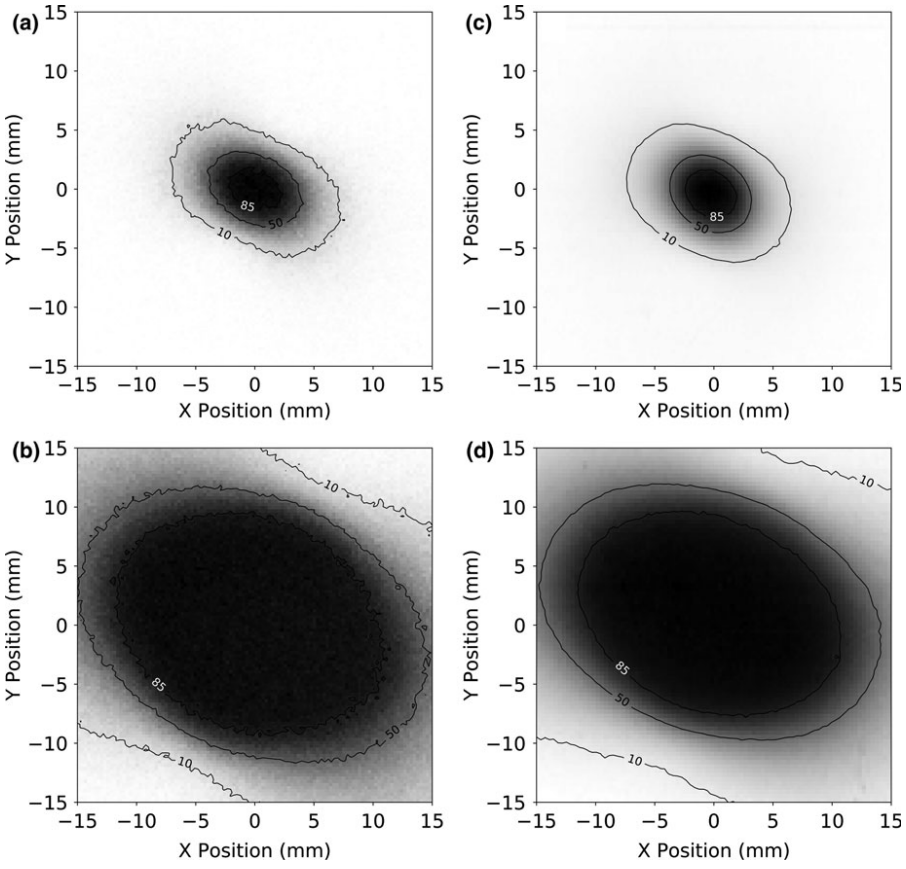

FIG. 5. Intensity modulated radio surgery (IMRS) mode of RGS comparing the dose delivered by the 4 mm and the 18 mm collimator between the Simulation (a), (b) and Experiment (c), (d).

the experimental penumbra to be slightly larger than that obtained from the simulations, with the maximum difference of 0.76 mm for the 18 mm collimator and minimum of 0.05 mm for the 8 mm collimator.

In order to compare different RGS devices and models described in the literature, we have included their 18 mm collimator X profiles in Fig. 4.

The experimental and simulated results from these studies show good agreement, which indicates that different RGS-type machines produce similar dose distributions with slight changes to the profile, as shown in Fig. 4. The UC Davis machine's design was changed on the site during installation which might have led to a narrower falloff as described in the work by Kubo et al.[6]

3.B. IMRS operation mode of the RGS

To study the dose distributions for the IMRS operation mode of the RGS, the radiation was blocked for orbital angles from 61° to 180° and 241° to 360° for both the simulated and experimental tests. The resulting dose distributions were no longer spherically symmetric since the incoming radiation is blocked from two opposite directions. The dose distributions adopted an ellipsoid shape as the irradiated region is shorter along the direction of the blocked angles than those for the unblocked angles. This is evident from the elliptic dose distribution displayed on the Gafchromic films shown in Figs. 5(a) and 5(b) for the 4 and 18 mm diameter collimators, respectively.

A comparison of the dose profiles along those two directions is shown in Fig. 6. The 90% and 50% widths along the blocked directions are shorter than those along the unblocked directions. Furthermore, the penumbra is considerably sharper along the short axis of the dose distribution than that of the long axis and those measured during the normal operation mode.

3.C. Speed modulation mode of the RGS

Even though the IMRS operation mode of the RGS offers a sharp falloff as demonstrated in the previous section, one apparent disadvantage is that the sources are off for a considerable fraction of the time. The additional time needed to deliver the desired dose will depend on the ratio of the total angles blocked to the total angles traversed. In this study, the use of the IMRS modality results in a threefold increase in delivery time, which is impractical for the treatment of conditions that require a high dose. To circumvent the increased treatment time while maintaining the benefits of the IMRS mode, we simulated a novel operation mode of the RGS, called the speed modulated radiosurgery (SMRS) mode. Instead of blocking the radiation at certain angles, in the SMRS mode, the orbital speed of the RGS is modulated as a function of its angle around the patient. Figure 7 shows the

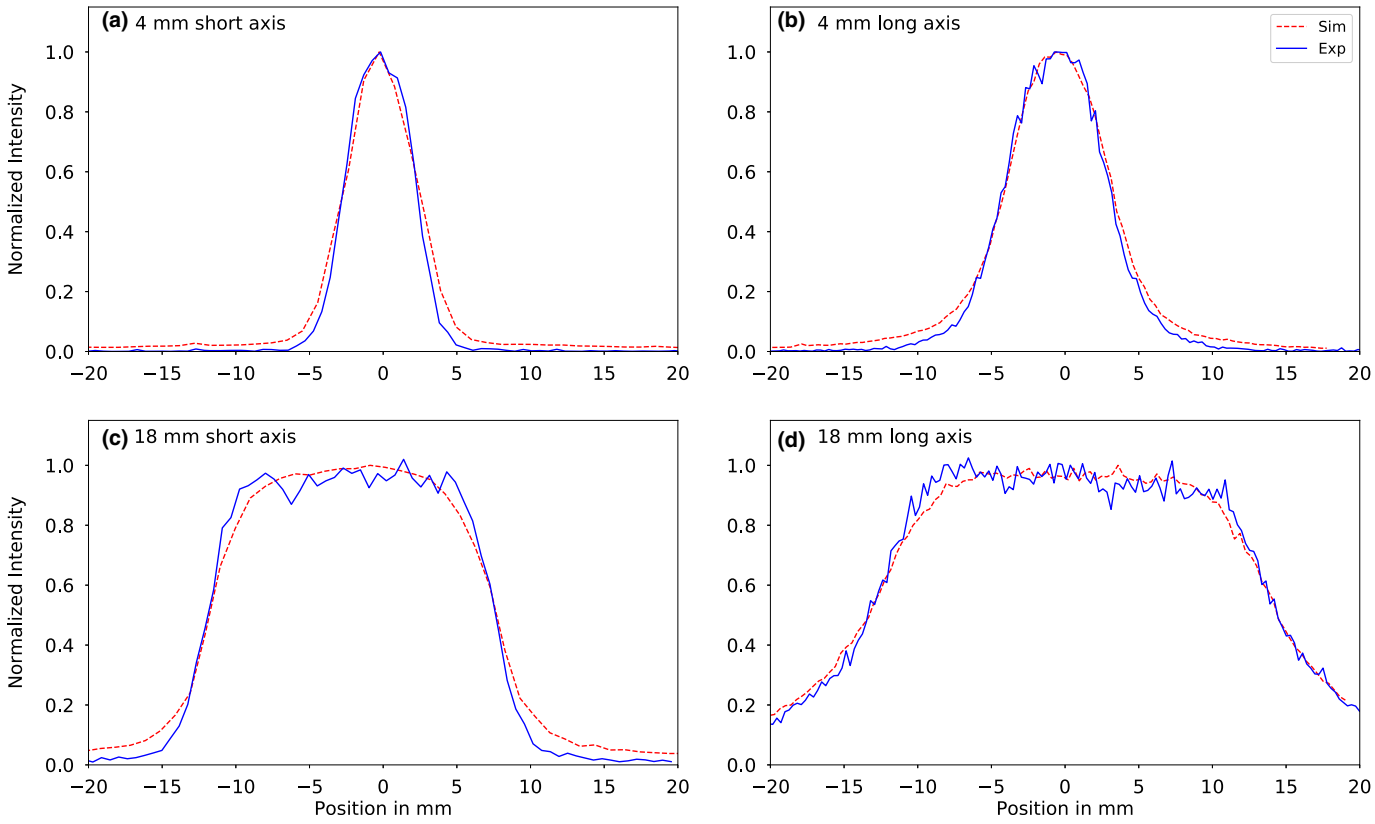

FIG. 6. Profile comparison along the short and long axis for the intensity modulated operation in 4 mm (a), (b) and 18 mm (c), (d) configuration. [Color figure can be viewed at wileyonlinelibrary.com]

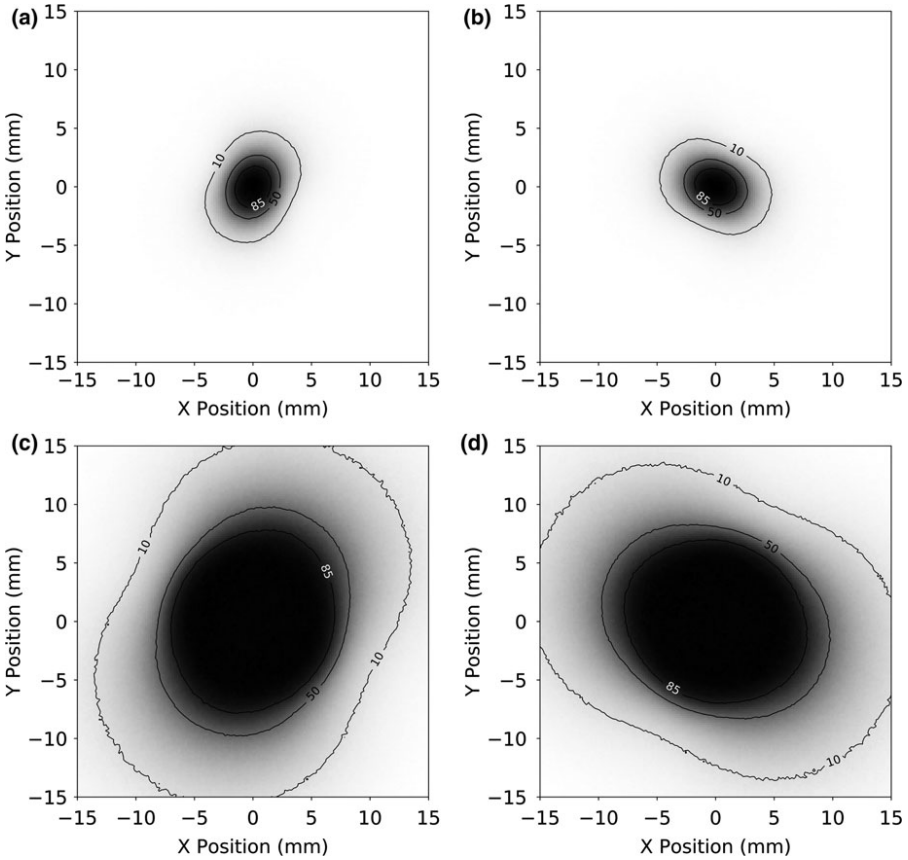

FIG. 7. Simulation of speed modulated radio surgery (SMRS) mode of RGS. (a) and (c) show cosine modulation, while (b) and (d) show sine modulation of the angles for 4 mm and 18 mm sizes of the collimator.

simulated dose distribution for the SMRS mode of the RGS. In Figs. 7(a) and 7(c), the rotational speed of the collimators was a sine function of the angle for the 4 and 18 mm collimators, respectively. For Figs. 7(b) and 7(d), a cosine function was used for the same collimators. The dose distributions produced are similar to the IMRS mode of the RGS. A comparison of the long and short axes of the dose distributions for the 4 and 18 mm collimators are shown in Fig. 8. Figure 8(a) has the comparison of the profiles from the 4 mm collimator configuration, while Fig. 8(b) shows the comparison of profiles from the 18 mm collimator configuration. The dose profile along the short axis has a sharper falloff compared to the dose profile along the long axis. This is similar to the dose profiles obtained from the IMRS mode described in the previous section; however, with a reduced irradiation time. The comparison of the penumbra produced by the IMRS and the SMRS mode are shown in Table II.

The penumbra varies approximately 0.28 mm for the 4 mm collimator configuration, while it varies less than 0.1 mm for the 18 mm collimator configuration.

4. DISCUSSION

Although the normal operation mode of the RGS can safely and effectively treat various lesions, dose spillage into surrounding healthy tissues makes it risky or impossible to treat cases near critical regions at risk. Blocked angle operating of the Gamma Knife® has been shown to effectively treat challenging skull based lesions[22]; however, alternative modalities have not been systematically studied for the RGS. This paper presents the first results of a systematic study of two novel RGS operation modes, IMRS, and SMRS. The normal operation and IMRS modalities were analyzed by comparing the experimental and simulated dose profiles and penumbra. Figure 3 shows that there is a systematic deviation between the simulated and experimental dose profiles, such that the agreement is better for the 4 and 8 mm collimators than for the 14 and 18 mm collimators. Specifically, the simulated falloff and maximum dose regions are in better agreement in the 4 and 8 mm collimators similar to previous model calculations.[8]

In contrast to simulations performed by Cheung et al.,[7] the current simulation shows considerable improvement, as the simulated results agree better with the experimental data as shown in Fig. 4. The percentage differences are more pronounced for the larger collimators; however, all profiles show good agreement. The agreement between the simulated dose profiles and experimental and published data validates the ability of our Geant4-based, Monte Carlo simulations for dose profile and penumbra calculations for the RGS and other SRS devices.

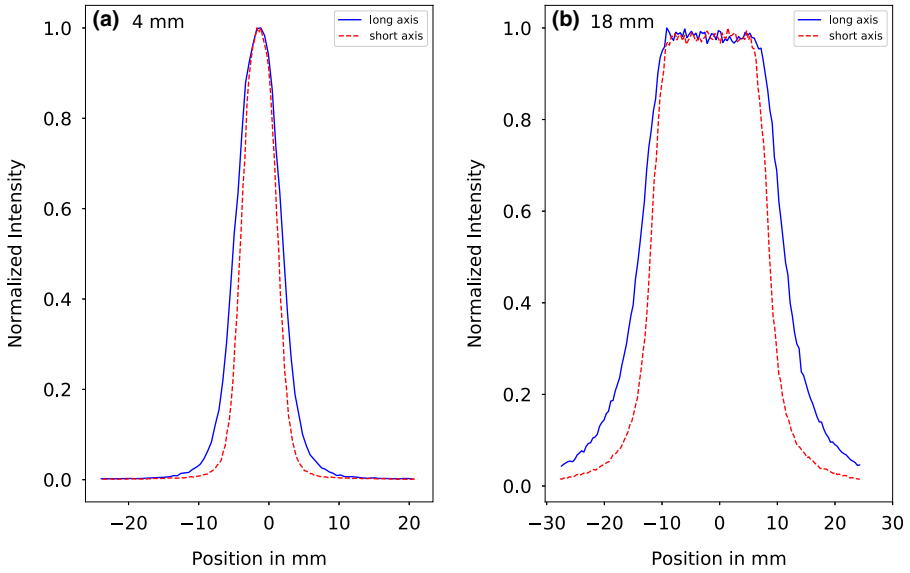

FIG. 8. Profile comparison along the short and long axis for the speed modulated operation in (a) 4 mm and (b) 18 mm configuration. [Color figure can be viewed at wileyonlinelibrary.com]

TABLE II. Comparison of the profile widths between simulations of IMRS and SMRS mode of operation. All penumbra values are calculated as (90% width – 50% width)/2 and are shown are in mm.

		IMRS (mm)			SMRS (mm)		
Collimator size	Axis	90%	50%	Penumbra	90%	50%	Penumbra
4	Long	3.9	7.59	1.85	3.62	7.88	2.13
	Short	2.33	4.9	1.29	2.34	5.2	1.44
18	Long	20.31	27.59	3.64	19.85	27.61	3.87
	Short	16.03	19.33	1.52	15.98	19.21	1.61

The IMRS modality exhibits a sharper dose falloff in the regions where the radiation is blocked. However, the dose delivery time increases in comparison with the normal operation mode. Nonetheless, our results suggest that the RGS IMRS mode could be used to safely target cases near critical regions, such as TN, that it cannot during normal operation.

Results from the SMRS simulations show that this modality produces a sharper penumbra than the normal operation mode in the regions where the orbital speed is increased. However, unlike the IMRS mode where the desired dose accumulates in an intermittent manner, in the SMRS mode the dose accumulates continuously, and thus decreases the time to achieve the desired dose in the center. The speed modulation functions for this study were chosen to allow for comparisons with the IMRS mode; however, we anticipate that more sophisticated functions could further improve critical tissue sparing, as well as target coverage, conformity, and treatment times. In contrast to the spherical shot placement method currently used for the RGS, SMRS may eventually be used to perform a continuous "dose sculpting" procedure for lesions near critical regions, such as the optic nerve and the brainstem, while reducing the overall treatment time.

5. CONCLUSION

The simulated dose profiles and penumbra were found to be in strong agreement with those obtained from measurements for the normal operation mode of the RGS. MC calculations of the dose profiles and penumbra for the IMRS operation mode also show a good agreement with the measurements. When operating in the IMRS mode, the RGS is capable of dose modulation where the dose distribution is highly restrained with sharper penumbra in the regions where the radiation is blocked. Due to the complete blockage of radiation during the procedure, the average dose rate can be factors lower, depending on the size of angular regions blocked. IMRS with the RGS could thus be clinically applicable for the treatment of lesions near vital regions at risk. The SMRS MC calculations reveal that this novel operation mode produces a sharper penumbra in regions where the orbital speed is increased. Unlike the IMRS mode, however, the SMRS mode does not increase the dose delivery time. More sophisticated functions could allow for the continuous delivery of radiation, which would reduce treatment times substantially.

CONFLICT OF INTEREST

The authors have no conflict to disclose.

[a)]Author to whom correspondence should be addressed. Electronic mail: etakacs@g.clemson.edu

REFERENCES

1. Goetsch SJJ, Murphy BDD, Schmidt R, et al. Physics of rotating gamma systems for stereotactic radiosurgery. *Int J Radiat Oncol Biol Phys*. 1999;43:689–696.
2. Wu A, Lindner G, Maitz AH, et al. Physics of gamma knife approach on convergent beams in stereotactic radiosurgery. *Int J Radiat Oncol Biol Phys*. 1990;18:941–949.
3. Lindquist C, Paddick I. The Leksell gamma knife perfexion and comparison with its predecessors. *Oper Neurosurg*. 2007;61(suppl 3):130–141.
4. Régis J, Tamura M, Guillot C, et al. Radiosurgery with the world's first fully robotized Leksell gamma knife perfexion in clinical use. *Neurosurgery*. 2009;64:346–356.
5. Lindquist C, Kihlström L, Hellstrand E. Functional neurosurgery – A future for the gamma knife? *Stereotact Funct Neurosurg*. 1992;57:72–81.
6. Kubo HD, Araki F. Dosimetry and mechanical accuracy of the first rotating gamma system installed in North America. *Med Phys*. 2002;29:2497–2505.
7. Cheung JYC, Yu KN. Rotating and static sources for gamma knife radiosurgery systems: Monte Carlo studies. *Med Phys*. 2006;33:2500–2505.
8. Tian Y, Wang H, Xu Y, et al. Comparison of dosimetric characteristics between stationary and rotational gamma ray stereotactic radiosurgery systems based on Monte Carlo simulation. *Biomed Phys Eng Express*. 2016;2:45014.
9. NINDS. *NINDS: trigeminal neuralgia fact sheet*. https://www.ninds.nih.gov/Disorders/Patient-Caregiver-Education/Fact-Sheets/Trigeminal-Neuralgia-Fact-Sheet. Published 2013. Accessed August 8, 2017.
10. Rogers CLL, Shetter AG, Fiedler JA, Smith KA, Han PP, Speiser BL. Gamma knife radiosurgery for trigeminal neuralgia: the initial experience of the Barrow Neurological Institute. *Int J Radiat Oncol Biol Phys*. 2000;47:1013–1019.
11. Varela-Lema L, Lopez-Garcia M, Maceira-Rozas M, Munoz-Garzon V. Linear accelerator stereotactic radiosurgery for trigeminal neuralgia. *Pain Phys*. 2015;18:15–27.
12. Singh R, Davis J, Sharma S. Stereotactic radiosurgery for trigeminal neuralgia: a retrospective multi-institutional examination of treatment outcomes. *Cureus*. 2016;8:e554.
13. Mammoo D. *Monte Carlo simulation and film dosimetry of rotating gamma system gamma ART-6000 output factors*, 2008. https://search.proquest.com/openview/0ed092111cab3d74faedff1b92363d2c/1?pq-origsite=gscholar&cbl=18750&diss=y
14. Luan S, Swanson N, Chen Z, Ma L. Dynamic gamma knife radiosurgery. *Phys Med Biol*. 2009;54:1579–1591.
15. Allison J, Amako K, Apostolakis J, et al. Geant4 developments and applications. *IEEE Trans Nucl Sci*. 2006;53:270–278.
16. Agostinelli S, Allison J, Amako K, et al. Geant4 – A simulation toolkit. *Nucl Instrum Methods Phys Res A*. 2003;506:250–303.
17. Apostolakis J, Asai M, Bogdanov AG, et al. Geometry and physics of the Geant4 toolkit for high and medium energy applications. *Radiat Phys Chem*. 2009;78:859–873.
18. Allison J, Amako K, Apostolakis J, et al. Recent developments in Geant4. *Nucl Instrum Methods Phys Res A*. 2016;835:186–225.
19. Raman S. A note on 60Co decay. *Zeitschrift für Phys*. 1969;228:387–390.
20. Romano F, Sabini MG, Cuttone G, Russo G, Mongelli V, Foroni R. Geant4-based Monte Carlo simulation of the Leksell Gamma Knife. In: Yu B, ed. *Nuclear Science Symposium Conference Record, Nuclear Science Symposium*. Honolulu, HI, Oct 26–Nov 3, 2007. IEEE; 2007:2581–2586.
21. GEANT4 Collaboration. *Reference physics lists*, 2013. http://geant4.cern.ch/support/proc_mod_catalog/physics_lists/referencePL.shtml. Accessed October 2, 2017.
22. Nakamura JL, Pirzkall A, Carol MP, et al. Comparison of intensity-modulated radiosurgery with gamma knife radiosurgery for challenging skull base lesions. *Int J Radiat Oncol*. 2003;55:99–109.

X-ray cabinet to deliver highly characterized low-dose X-ray radiation to bio-samples

Bishwambhar Sengupta[1], Donald Medlin[1], Michael Sprunk*, Justin Napolitano[2],
Jaclyn D'Avanzo[1], Xiao Ran Zheng[1], Delphine Dean[2], and Endre Takacs[1]
[1]*Department of Physics and Astronomy, Clemson University, Clemson, SC - 29634, USA*
[2]*Department of Bioengineering, Clemson University, Clemson, SC - 29634, USA and*
**Currently at the Department of Mechanical Engineering, Auburn University, Auburn - 36849 AL, USA*
(Dated: July 11, 2019)

We have designed and tested a climate-controlled, radiation-shielded incubator cabinet for the purpose of analyzing the effects of low dose X-ray radiation on biological tissues and cell cultures. Bremsstrahlung X-rays incident on exchangeable fluorescence plates produce strong, quasi-monochromatic radiation directed toward a small sample container. X-ray source, sample, and detector are enclosed in the incubator – maintaining the optimal environment for biological samples to increase longevity to a maximum 72 hours. An example experiment is performed observing rat Vascular Smooth Muscle Cell growth after using characteristic X-rays of iron, copper, and calcium to impart a dose of 2 *mGy*. All irradiated cultures show significant increases in cell number over controls at 48hrs. Interestingly, the increases were spectrum dependent. although the total dose was the same, the cultures irradiated with characteristic x-rays from iron had significantly more cells than the other irradiated culture conditions. The experiment lends credence to the efficacy of the apparatus and shows promise for future low dose bio-radiation analysis.

Note: This article has been submitted to Review of Scientific Instruments. After it has been accepted and published, it will be found at https://aip.scitation.org/journal/rsi

The effect of low dose radiation on tissues and organs is an ongoing debate within the radiation biology community. It is an important research area due to the many common low dose sources that can produce these effects such as X-ray and CT diagnostic devices, therapeutic instruments, naturally-occurring background radiation, cosmic radiation, and even spill-outs from disaster areas like Fukushima. Medical imaging, for example, has now become a routine procedure in the US with approximately 70 million scans carried out each year [1]. Concerns regarding risks from the cumulative exposure to ionizing radiation that originate from these sources are being raised [2–4]. As a result, scientific societies are assessing carcinogenic risks [5] and regulatory bodies have initiated safety studies [6–8] related to radiation. Recent experiments have also suggested that exposure to low-dose radiation in space may have long-term effects on astronauts or space travelers [9, 10].

The difficulty of these studies stems from the fact that the subjects are biological systems (from cells to animal models) with complex time-varying feedback mechanisms and the outcome strongly depends on the initial conditions. Low-dose radiation on cells, for example, has shown wide ranges of results due to the variation in cell types, radiation source, and doses [11–15]. Some studies have shown no effect below a certain dose threshold ($< 0.1\ Gy$) [11, 12] while others suggested the appearance of positive effects on certain cell types and in animal models [13–15]. Some of these experiments, however, are difficult to reproduce due to the lack of sufficient information about the exposure conditions including the radiation type, dose-rate, geometry, filters used, arrangement of tissues in containers, and other environmental conditions that might affect the dose delivered to the sample.

In order to carry out related research in our lab, we have designed and built an X-ray irradiator device that allows the control and measurement of radiation and external conditions during the irradiation of cell cultures. One of the unique features of the instrument is that the irradiator was designed to operate inside an incubator, which provides better control over the environmental conditions for the cell culture samples. It also incorporates a single-photon counting X-ray detector that continuously monitors the arrival of X-rays, which together with preceding geometrical, physical, and spectral calibration procedures provide well characterized and reproducible radiation conditions.

The present paper describes the design, calibration procedures, and one of the initial experiments of the X-ray irradiator that was put into operation at the Medical Physics Lab of Clemson University.

I. SETUP

The components of the irradiator setup were designed to fit inside a commercial biological incubator cabinet with precise temperature and atmospheric control. The temperature, humidity, and CO_2 composition are being monitored and controlled by the built-in sensors and electronics that did not require further modifications once the irradiator with a radiation safety box was placed inside.

The irradiator itself is an X-ray fluorescence source with replaceable fluorescence plates that produce strong characteristic quasi-monochromatic radiation upon irradiation from bremsstrahlung X-rays from a source. The geometry of the irradiator box can be seen on Fig.1. The X-ray source has a power rating of 4 W and is capable of handling a maximum tube voltage of 50 kV and a maximum electron current of 40 μA[16].

Since the objective was to build a radiation-safe X-ray irradiator device to perform experiments involving low-dose of X-rays, the X-ray tube, the metal reflector plate, holder of biological samples, and the detector were placed inside a custom designed steel cabinet. The cabinet was made from

6 *mm* thick stainless-steel sheets with external dimensions of 42 $cm \times 36.8\ cm \times 15.7\ cm$. The front side has a sliding door to access the inner area with radiation safe slots design to allow the temperature and environment to be controlled by the incubator while preventing any X-rays from escaping. A small slit at the top of the cabinet allowed the installation of a PCIe slot fan with dual purpose — provide airflow to maintain the incubator environmental conditions and cool the X-ray tube. The design of the radiation safety box can be seen on Fig. 2.

The X-ray tube is mounted on a stand fixed in place at an angle facing the X-ray fluorescent plate holder. There is a secondary fan installed below the holder with some displacement brackets to further help the cooling of the X-ray tube. The fluorescent plate has dimensions of $10.3\ cm \times 10\ cm \times 0.3\ cm$ and is fixed on a rotatable pivot point. Different metal plates have been tested as targets providing characteristic X-ray peaks according to their material. Non-metallic elements can be painted or glued onto the plates provided that they have the necessary thickness to fully absorb the incoming bremsstrahlung X-ray beam to avoid the appearance of X-ray peaks from the base plate.

The holder for the biological sample cup was designed to position a plastic cup with a mylar foil above the fluorescent plate. The selection of the commercially available self-assembled high-density polyethylene (HDPE) cup[17] with a 6 μm thick mylar foil bottom was made to allow the low energy X-rays to reach the cell cultures without considerable attenuation. This is a critical feature of these experiments as low-energy X-rays show strong absorption even in thin layers of material, therefore standard cell culture dishes would not work. Attenuation of radiation through the mylar bottom was considered in the final dose rate calculations.

A Si-PIN diode solid-state X-ray detector was chosen to monitor the X-ray radiation during the irradiation and in preceding calibration measurements[18]. During the irradiation the detector and the sample holder are at fixed angle of 10 degrees apart. The detector holder plate is mounted on a linear rail attached to an arced groove to enable the change of its distance and direction from the fluorescent plate. In the absence of the biological sample cup holder in place, the detector can be placed exactly at the position of the tissue samples. This position allows the measurement of X-rays right at the location of the tissues, while rotated to the side allows for the continuous monitoring of the radiation during the irradiation process.

During the calibration of the geometrical arrangement, the detector setup can be pivoted around the fluorescent plate that enables the angular rotation θ of the detector setup with respect to the plate and it can slide along the rails for adjusting the distance $\vec{r}$. A metal ruler is attached to the rails so that we can measure the distance of the detector from the reflector plate. The nose with the front window of the X-ray tube is enclosed in a solid steel cube of side 4.44 *cm* to shield the sample and the detector from any direct radiation from the tube. The only radiation reaching the sample is monochromatic X-ray florescence from the fluorescent plate. There is a junction box at the top of the cabinet which houses all cable connectors from outside and also shields all external ports thereby avoiding any leaks through the power and data ports. This cabinet is housed in an incubator[19] that maintains the designed temperature and CO_2 levels for the cell cultures. The incubator was tested for leaks by powering on the tube and measuring the leakage with a survey detector to make sure that there was no stray radiation coming out of the incubator.

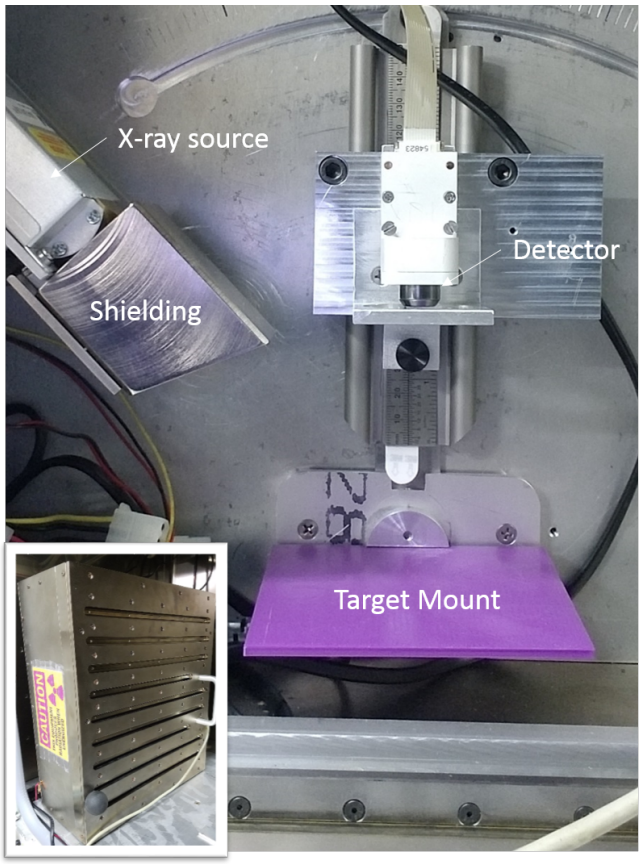

FIG. 1. X-ray fluorescence source and the detector arrangement inside the cabinet. The detector is placed in the position of the biological sample for calibration.; Inset: The radiation box from outside showing the shielded opening slots.

II. DETECTOR CALIBRATION AND TRANSMISSION CORRECTIONS

For the geometrical survey of the radiation emitted by the fluorescent plate the X-ray tube was powered with a voltage of 15 *keV* and a current of 75 μA. Single X-ray photon counts were detected and acquired as a spectrum. Characteristic X-ray peaks of copper were identified and used to characterize the spatial dependence of the X-ray radiation field. The detector was placed at distances between 10.1 *cm* and 13.1 *cm* from the plate with 1 *cm* increments and 20 degrees on either side of the central position with 2-degree increments. The intensity of the $Cu\ K_\alpha$ peak was plotted on Fig. 3. shows that there is not much variation in the photon count with respect to the angular position of the detector as X-ray fluorescence

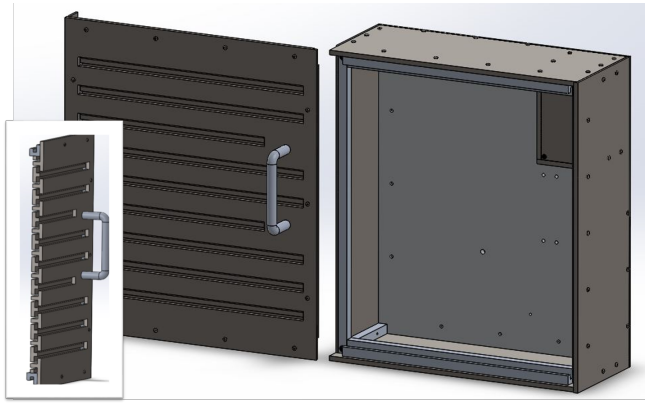

FIG. 2. Illustration of the radiation safety box and the sliding door with the opening slots. Inset: a cut-out view of the radiation leak-proof door

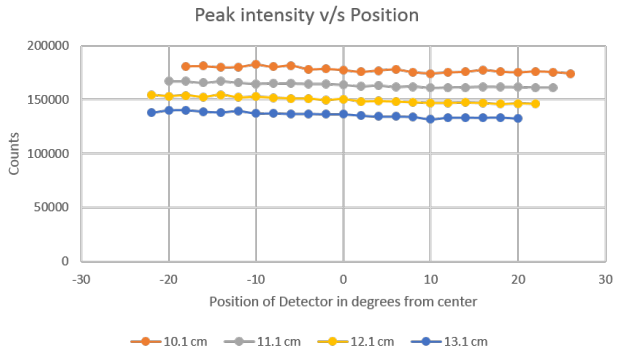

FIG. 3. Intensity of the $Cu\ K_\alpha$ peak as a function of the detector's position

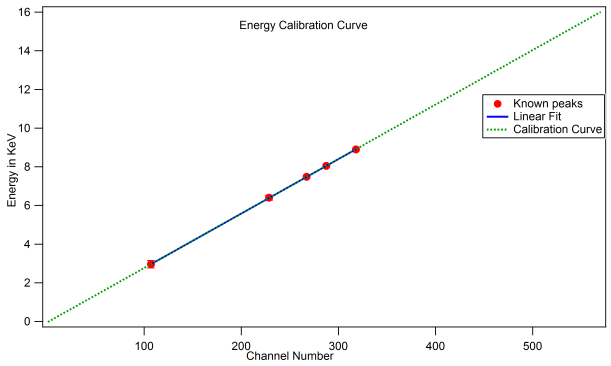

FIG. 4. Energy calibration curve of the Si-PIN diode detector based on known K transition lines

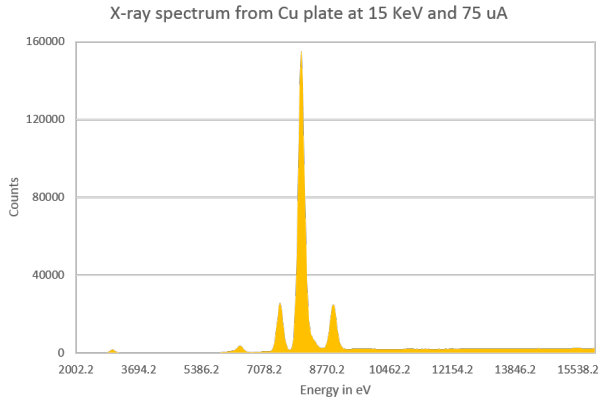

FIG. 5. X-rays spectrum obtained using a copper plate with the detector in the position of the biological sample. A third order polynomial can approximate the small bremsstrahlung background radiation reaching the detector in this range.

from the metal plate does not vary strongly in the range of 20 degrees on either side of the central axis. The count rate drops as a function of detector distance from the fluorescent plate.

In order to identify the characteristic peaks and assign energy to the individually detected photons the energy calibration of the detector was based on the known energies of the characteristic K peaks of copper, iron, nickel, and argon. X-ray peaks were fitted with Gaussian functions of the pulse height distribution and the channel positions were assigned according to the peak position parameters. The calibration curve obtained is shown on Fig. 4 and the calibrated spectrum on Fig. 5. It can be seen that the fluorescence spectrum originating from the copper plate is dominated by the K_α and K_β peaks of Cu and Ni with smaller contributions from scattered bremsstrahlung X-rays from the tube and smaller characteristic peaks from neighboring surfaces.

The number of photons in each calibrated channel allows for the determination of the absorbed energy at the X-ray energy corresponding to the particular channel. This is the basic input that goes into the dose and dose rate determination. Due to the single photon nature of the detection method, the uncertainty of the dose determination can also be estimated by assuming that the uncertainty of the photon count in a certain channel is square root of that number.

The definition of the absorbed dose is the expectation value of energy imparted into matter per unit mass at a point [20]. In order to determine the dose absorbed by the biological sample medium, we must first find out the number of photons that would be stopped in the medium given the number of photons counted on the detector. In addition, there are certain corrections that need to be considered based on the absorption of X-rays both during the detection and the irradiation.

X-ray counts obtained from the detector must be corrected for the transmission rate of X-ray photons through different media that they encounter before reaching the detector. For example, before reaching the Si absorber within the detector, the photons must pass through a 12.5 μm thick Be window and a layer of air between the plate and detector. Thus, the count we obtain is less than the actual count due to absorption in these materials. We should also accommodate the dead time of the detector when its electronics is not capable of receiving a photon. During the irradiation of the biological samples, the

photons travel through air and the mylar sheet under the cell culture which is approximately 6 μm thick. In order to include this correction, for each medium, the energy dependent X-ray transmission coefficients from a standard reference table [21] were used to correct for the final photon count and uncertainty. The final photon count was then converted to its corresponding energy deposition and the dose absorbed was calculated by dividing this with the mass of the cell culture medium.

III. DOSE RATE AND ABSORBED DOSE CALCULATIONS

In order to calculate the required irradiation time for a particular cell culture experiment the dose rate resulting from the use of a certain fluorescent plate and X-ray source setting needs to be obtained. The actual received dose can be accurately determined after the experiment using a similar method and the X-ray data collected during the irradiation.

A sample spectrum on Fig. 5 was obtained with the detector in the position of the biological tissue sample. A similar spectrum can be obtained during the irradiation with the detector at an off angle position. To calculate the energy deposition the total X-ray counts at every energy bin needs to be corrected for the dead time of the detector, the absorption due to the Be window in front of the detector, the absorption through the layers of air between the fluorescent plate and the detector window and the plate and the cell culture sample, the absorption by the mylar sheet below the cells, and the thickness of the cell culture medium.

In order to calculate the dose, the detector surface area also need to be considered. This will enter into the calculation of the mass of the absorbing sample. The last piece of correction that need to be accounted for comes from the geometric location of the detector during the data collection. The layer of cell cultures is usually about 5 μm thick and the nutrition media on top of the cells is about 1-2 centimeters. X-ray absorption directly effecting the cells take place within the cell culture layer, but indirect effects (e.g. via free radical production in the media) can originate from the thicker layer. For the purposes of our calculation we can approximate the properties of both layers with those of water. The absorption coefficients at X-ray energies that correspond to the main peaks of the spectrum on Figure 5 of different materials are shown in Table 1[21].

The formula that calculates the average dose received by the sample as a function of the photon counts in each energy bins of the detector can be written as below. In order to calculate the dose rate this needs to be divided by the total acquisition time of the spectrum.

$$D = \frac{\sum_{i=1}^{n} N_i \times E_i \times C_i}{M}$$

where N_i is the counts at each channel, E_i is the X-ray energy of the corresponding channel, M is the mass of the biological sample (either the cell culture for the direct absorption or the nutritional media) corresponding to the detector's surface area. C_i contains the correction terms discussed above

TABLE I. The absorption coefficients at X-ray energies that correspond to the main peaks of the spectrum

Signature	Energy in KeV	12.5 um Be Window	6 um mylar Sheet	5um Water
Ar K_α	2.96	0.95019	0.89266	0.89266
Ar K_β	3.19	0.96042	0.91301	0.91301
Fe K_α	6.4	0.99543	0.98912	0.98912
Fe K_β	7.06	0.99660	0.99197	0.99197
Ni K_α	7.47	0.99713	0.99326	0.99326
Cu K_α	8.05	0.99768	0.99461	0.99461
Ni K_β	8.26	0.99784	0.99504	0.99504
W L_α	8.4	0.99794	0.99530	0.99530
Cu K_β	8.91	0.99824	0.99606	0.99606
W L_β	9.67	0.99858	0.99695	0.99695

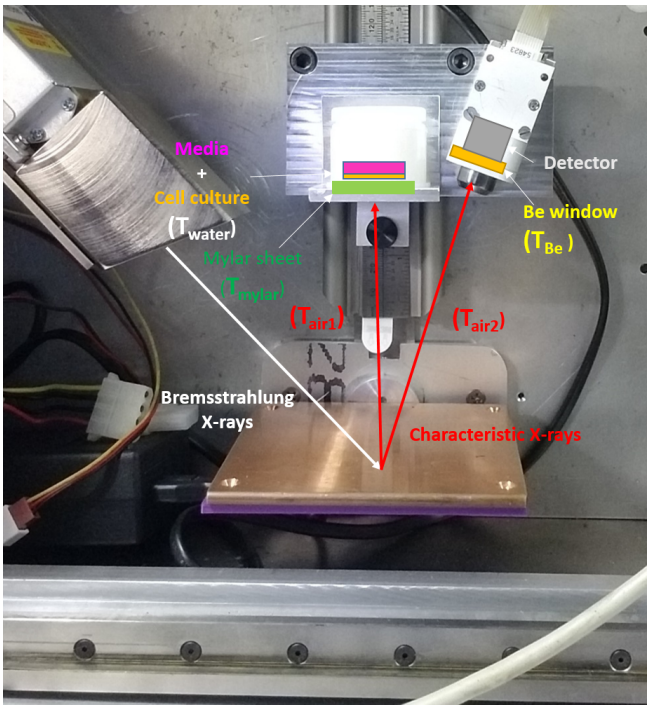

FIG. 6. Illustration showing the propagation of X-rays and the corresponding transmission coefficients used in our calculation

that depend on the energy of the X-ray photon.

$$C_i = \frac{T_{i_{mylar}} \times T_{i_{Air_1}} \times [1 - T_{i_{Water}}]}{T_{i_{Be}} \times T_{i_{Air_2}}} \times C_d$$

The photon transmission coefficients T_i in the above equation can be calculated from the tabulated mass absorption coefficients[21] as follows:

$$T_i = \exp\left(\frac{-\mu_i \times x}{\rho_i}\right)$$

where x is the thickness of the material (beryllium, mylar, Water or Air), ρ is the density of the material, and μ_i is the mass absorption coefficient at the photon energy corresponding to

bin i.
C_d is the correction term due to detector's dead time. Given photon counts in the sample spectrum of Fig. 5, the dose absorbed per minute by the cells was $6.79 \mu Gy/min \pm 0.15\ \mu Gy/min$.

IV. CELL CULTURE IRRADIATION EXPERIMENT

Experiments were done on a variety of cell types. The below example used Vascular Smooth Muscle Cells $[VSMCs]$ which are derived from rats. These cells were at a passage of 9 when plated onto the mylar film. The cells were cultured in media made from 500 mL of Dulbecco's Modified Eagle Media $[DMEM]$, 50 mL of Fetal Bovine Serum $[FBS]$, and 10 mL of Antibiotic-Antimycotic. The cultures were seeded at $10,000$ cells per mylar cup and were allowed 18 hours to attach before being irradiated. It should be noted that not all cell types will attach and grow well on mylar. For less adherent cells (cardiomyocytes, neurons, etc) or for longer culture times, coating the mylar with an adherent peptide (e.g., RGD) or protein (e.g., collagen) may be necessary. For those cultures the thickness of the protein layer needs to be accounted for in the dose calculation.

The variable tested in this experiment was the average soft X-ray energy that depended on the type of fluorescent plate used. In each case cells were set to receive a fixed dose of $2m\ Gy$. The cells were split into four equal groups, and each group was given a different energy irradiation. Group A was dosed via an iron plate, Group B via a copper plate, Group C via a calcium plate, and Group D was left unirradiated as control. All cells traveled together and were stored together, even those not receiving irradaition.

Proliferation assays were completed 8, 24, and 48 hours after irradiation. The results can be seen in Fig. 6. It has been observed that after 36 to 48 hours, the cells multiply at a slower rate. This is expected due to crowding of the cultures with confluency. Figure 6 shows the results of the proliferation assay with n = 9 for each condition and time point, except the iron irradiation at 24hr which only had 8 samples.

A proliferation assay was also completed at 72 hours, n=0 for each condition. However, as previously mentioned, the cultures reached confluence at this time for all conditions. The cells covered most of the culture surface in a solid monolayer. To explore the effect of radiation on longer term (>48hr) VSMC cell growth, in future experiments, the initial cell count per sample will be reduced. In the future, the initial cell seeding can be reduced to $40,000$. This will allow experiments to successfully continue up until 72 hours. It should be noted that only a small portion of the cells plated actually initially stick to the mylar surface. This is likely due to the fact that while VSMCs are adherent, the mylar surface lacks the specific attachment moieties to allow for integrin binding. Coating the substrate with collagen or fibronectic could aid in initial cell attachment.

Every data set, when compared to its corresponding control set, was found statistically significant via a paired Student's t test where $p < .05$, with the exception of Copper at the 24 hours post irradiation. The growth from 24 hour to 48 hour is most prominent, where all irradiated samples grow exponentially faster than the control. It is also clear that the changing of the plate used has an impact on the treated cells. Based on this data, we can say that cell proliferation depended on the plate used for irradiation (Iron>Copper>Calcium>Control) by 48 hours whereas the differences at <24 hours were not as pronounced. There was no significant cell death seen in any of the culture conditions indicating that the low $2mGy$ dose was well under the threshold to elicit apoptosis. This is consistent with our previous findings with an earlier version of our irradiation system, where we showed increased proliferation of 3T3 fibroblasts 48hrs after irradiation with characteristic copper X-rays[22], that irradiated cells proliferate faster than their control counterparts. We have started a new set of experiments to isolate energy and dose rate dependence, to determine which variable, if not both, is causing the cells to produce the observed time dependence pattern. Additionally, other cell types are being tested in order to confirm if the impact of the radiation is dependent on the cell type. Polymerase Chain Reaction Analysis $[PCR]$ will be performed to determine if there is any change in the genetic information of the cells, which we believe could be the cause of this change in growth.

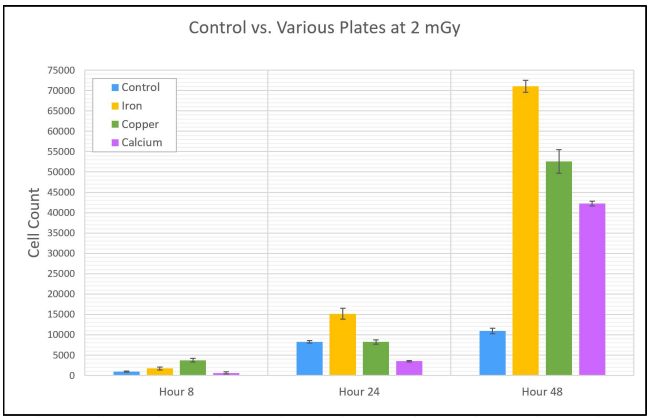

FIG. 7. Cell response after radiation

V. CONCLUSION

The design of a new environmentally controlled X-ray setup allows the irradiation of different cell cultures for well-characterized, systematic experiments. The entire irradiator box is small and can easily fit inside a standard incubator. Radiation safety, X-ray generation and detection considerations drove the development of the configuration. X-ray fluorescence radiation from the metal plate is carefully characterized and offers tunability in energy and dose rate. When the tube is operating at 15 keV and 75 μA settings, at a distance of 10 cm from the plate, a cell culture layer of $5\mu m$ received a direct dose rate of $6.79\ \mu Gy/min \pm 0.15\ \mu Gy/min$. As the biological samples are prepared in a standard mylar bottom plastic cup, it offers the flexibility of a wide range of cell types

and the use of different nutritional media. Larger samples like tendons and small tissues can also be irradiated after considerations of the geometrical arrangements. The setup allows us to perform a systematic study of the effect of low-dose X-ray radiation on cells under well-controlled conditions.

ACKNOWLEDGMENTS

We wish to acknowledge the support of Moxtek, Inc. for providing us their experimental X-ray tube for this project and for their continued support during the duration of the project.

Note: This article has been submitted to Review of Scientific Instruments. After it has been accepted and published, it will be found at https://aip.scitation.org/journal/rsi

[1] F. A. Mettler, M. Bhargavan, K. Faulkner, D. B. Gilley, J. E. Gray, G. S. Ibbott, J. A. Lipoti, M. Mahesh, J. L. McCrohan, M. G. Stabin, B. R. Thomadsen, and T. T. Yoshizumi, Radiology **253**, 520 (2009).

[2] D. J. Brenner, R. Doll, D. T. Goodhead, E. J. Hall, C. E. Land, J. B. Little, J. H. Lubin, D. L. Preston, R. J. Preston, J. S. Puskin, E. Ron, R. K. Sachs, J. M. Samet, R. B. Setlow, and M. Zaider, Proceedings of the National Academy of Sciences of the United States of America **100**, 13761 (2003).

[3] D. J. Brenner and E. J. Hall, New England Journal of Medicine **357**, 2277 (2007).

[4] R. Smith-Bindman, New England Journal of Medicine **363**, 1 (2010).

[5] E. S. Amis, P. F. Butler, K. E. Applegate, S. B. Birnbaum, L. F. Brateman, J. M. Hevezi, F. A. Mettler, R. L. Morin, M. J. Pentecost, G. G. Smith, K. J. Strauss, and R. K. Zeman, Journal of the American College of Radiology **4**, 272 (2007).

[6] H. B. Harvey and P. V. Pandharipande, Radiology **262**, 391 (2012).

[7] C. f. D. Health and Radiological, .

[8] M. Wintermark and M. H. Lev, AJNR. American journal of neuroradiology **31**, 2 (2010).

[9] T. Lu, Y. Zhang, M. Wong, A. Feiveson, R. Gaza, N. Stoffle, H. Wang, B. Wilson, L. Rohde, L. Stodieck, F. Karouia, and H. Wu, Life Sciences in Space Research **12**, 24 (2017).

[10] M. Boerma, G. A. Nelson, V. Sridharan, X.-W. Mao, I. Koturbash, and M. Hauer-Jensen, World Journal of Cardiology **7**, 882 (2015).

[11] H. Jiang, W. Li, X. Li, L. Cai, and G. Wang, Journal of Radiation Research **49**, 219 (2008).

[12] A. Kiuru, M. Kämäräinen, S. Heinävaara, K. Pylkäs, K. Chapman, A. Koivistoinen, T. Parviainen, R. Winqvist, M. Kadhim, V. Launonen, and C. Lindholm, PLoS ONE **9**, e93211 (2014).

[13] M. Chen, Q. Huang, W. Xu, C. She, Z.-G. Xie, Y.-T. Mao, Q.-R. Dong, and M. Ling, PLoS ONE **9**, e104016 (2014).

[14] X. Liang, J. Gu, D. Yu, G. Wang, L. Zhou, X. Zhang, Y. Zhao, X. Chen, S. Zheng, Q. Liu, L. Cai, J. Cui, and W. Li, Dose-Response **14**, 155932581562217 (2016).

[15] F. R. Tang, W. K. Loke, and B. C. Khoo, Journal of Radiation Research **58**, 165 (2017).

[16] S. Cornaby and K. Kozaczek, in *Encyclopedia of Analytical Chemistry* (John Wiley & Sons, Ltd, Chichester, UK, 2016) pp. 1–25.

[17] "HDPE cup, Chemplex Industries Inc., Palm City, FL,".

[18] "XPIN-13XT X-Ray Detector, Moxtek Inc., Orem, Utah,".

[19] "Isotemp Microbiological Incubator, Fisher Scientific,".

[20] F. H. Attix and Wiley InterScience (Online service), *Introduction to radiological physics and radiation dosimetry* (Wiley, 1986) p. 607.

[21] B. Henke, E. Gullikson, and J. Davis, Atomic Data and Nuclear Data Tables **54**, 181 (1993).

[22] K. Truong, S. Bradley, B. Baginski, J. R. Wilson, D. Medlin, L. Zheng, R. K. Wilson, M. Rusin, E. Takacs, and D. Dean, PLOS ONE **13**, e0190330 (2018).

Bibliography

[1] NCI. What Is Cancer? - National Cancer Institute, 2015.

[2] GBD 2015 Disease GBD 2015 Disease and Injury Incidence and Prevalence Collaborators, Injury Incidence, and Prevalence. Global, regional, and national incidence, prevalence, and years lived with disability for 310 diseases and injuries, 1990-2015: a systematic analysis for the Global Burden of Disease Study 2015. *Lancet (London, England)*, 388(10053):1545–1602, 2016.

[3] Bernard W. Stewart, Chris Wild, International Agency for Research on Cancer, and World Health Organization. *World cancer report 2014*. International Agency for Research on Cancer, Leyon Cedex, 2014.

[4] GBD 2015 Mortality GBD 2015 Mortality and Causes of Death Collaborators and Causes of Death. Global, regional, and national life expectancy, all-cause mortality, and cause-specific mortality for 249 causes of death, 1980-2015: a systematic analysis for the Global Burden of Disease Study 2015. *Lancet (London, England)*, 388(10053):1459–1544, oct 2016.

[5] Siddhartha. Mukherjee. *The emperor of all maladies : a biography of cancer*. Scribner, 2010.

[6] NIH. Cancer of Any Site - Cancer Stat Facts, 2016.

[7] NIH. Edwin Smith's Surgical Papyrus.

[8] Heather (Science) Pringle. Mummy Has Oldest Case of Prostate Cancer in Ancient Egypt — Science — AAAS, 2011.

[9] H K Biesalski, B Bueno de Mesquita, A Chesson, F Chytil, R Grimble, R J Hermus, J Köhrle, R Lotan, K Norpoth, U Pastorino, and D Thurnham. European Consensus Statement on Lung Cancer: risk factors and prevention. Lung Cancer Panel. *CA: a cancer journal for clinicians*, 48(3):167–76; discussion 164–6, 1998.

[10] H Kuper, H-O Adami, and P Boffetta. Tobacco use, cancer causation and public health impact. *Journal of internal medicine*, 251(6):455–66, jun 2002.

[11] H Kuper, P Boffetta, and H-O Adami. Tobacco use and cancer causation: association by tumour type. *Journal of internal medicine*, 252(3):206–24, sep 2002.

[12] Preetha Anand, Ajaikumar B. Kunnumakara, Chitra Sundaram, Kuzhuvelil B. Harikumar, Sheeja T. Tharakan, Oiki S. Lai, Bokyung Sung, Bharat B. Aggarwal, and Bharat B Aggarwal. Cancer is a Preventable Disease that Requires Major Lifestyle Changes. *Pharmaceutical Research*, 25(9):2097–2116, sep 2008.

[13] Lawrence H Kushi, Tim Byers, Colleen Doyle, Elisa V Bandera, Marji McCullough, Anne McTiernan, Ted Gansler, Kimberly S Andrews, Michael J Thun, and American Cancer Society 2006 Nutrition and Physical Activity Guidelines Advisory Committee. American Cancer Society Guidelines on Nutrition and Physical Activity for cancer prevention: reducing the risk of cancer with healthy food choices and physical activity. *CA: a cancer journal for clinicians*, 56(5):254–81; quiz 313–4, 2006.

[14] Krishnan Bhaskaran, Ian Douglas, Harriet Forbes, Isabel Dos-Santos-Silva, David A Leon, and Liam Smeeth. Body-mass index and risk of 22 specific cancers: a population-based cohort study of 5·24 million UK adults. *The Lancet*, 384(9945):755–765, aug 2014.

[15] John B Little. Ionizing Radiation. In R.E. Bast, R.C. Jr.; Kufe, D.W.; Pollock, editor, *Cancer Medicine*, chapter 14. BCDecker, NY, 5th edition, 2000.

[16] NCI. Risk Factors: Radiation - National Cancer Institute, 2019.

[17] James E. Cleaver and David L. Mitchell. Ultraviolet Radiation Carcinogenesis. In R.E. Bast, R.C. Jr.; Kufe, D.W.; Pollock, editor, *Cancer medicine*, chapter 15. BCDecker, NY, 5th edition, 2000.

[18] Joseph S. Pagano, Martin Blaser, Marie-Annick Buendia, Blossom Damania, Kamel Khalili, Nancy Raab-Traub, and Bernard Roizman. Infectious agents and cancer: criteria for a causal relation. *Seminars in Cancer Biology*, 14(6):453–471, dec 2004.

[19] Suzana Ljubojevic and Mihael Skerlev. HPV-associated diseases. *Clinics in Dermatology*, 32(2):227–234, mar 2014.

[20] Dimitrios H Roukos. Genome-wide association studies: how predictable is a person's cancer risk? *Expert Review of Anticancer Therapy*, 9(4):389–392, apr 2009.

[21] David Cunningham, Wendy Atkin, Heinz-Josef Lenz, Henry T Lynch, Bruce Minsky, Bernard Nordlinger, and Naureen Starling. Colorectal cancer. *The Lancet*, 375(9719):1030–1047, mar 2010.

[22] Michele L. Coté, Mei Liu, Stefano Bonassi, Monica Neri, Ann G. Schwartz, David C. Christiani, Margaret R. Spitz, Joshua E. Muscat, Gad Rennert, Katja K. Aben, Angeline S. Andrew, Vladimir Bencko, Heike Bickeböller, Paolo Boffetta, Paul Brennan, Hermann Brenner, Eric J. Duell, Eleonora Fabianova, John K. Field, Lenka Foretova, Søren Friis, Curtis C. Harris, Ivana Holcatova, Yun-Chul Hong, Dolores Isla, Vladimir Janout, Lambertus A. Kiemeney, Chikako Kiyohara, Qing Lan, Philip Lazarus, Jolanta Lissowska, Loic Le Marchand, Dana Mates, Keitaro Matsuo, Jose I. Mayordomo, John R. McLaughlin, Hal Morgenstern, Heiko Müeller, Irene Orlow, Bernard J. Park, Mila Pinchev, Olaide Y. Raji, Hedy S. Rennert, Peter Rudnai, Adeline Seow, Isabelle Stucker, Neonila Szeszenia-Dabrowska, M. Dawn Teare, Anne Tjønnelan, Donatella Ugolini, Henricus F.M. van der Heijden, Erich Wichmann, John K. Wiencke, Penella J. Woll, Ping Yang, David Zaridze, Zuo-Feng Zhang, Carol J. Etzel, and Rayjean J. Hung. Increased risk of lung cancer in individuals with a family history of the disease: A pooled analysis from the International Lung Cancer Consortium. *European Journal of Cancer*, 48(13):1957–1968, sep 2012.

[23] Deborah Watkins Bruner, Dirk Moore, Alicia Parlanti, Joanne Dorgan, and Paul Engstrom. Relative risk of prostate cancer for men with affected relatives: Systematic review and meta-analysis. *International Journal of Cancer*, 107(5):797–803, dec 2003.

[24] Donald W. Kufe, James F. Holland, Emil Frei, and American Cancer Society. *Cancer medicine 6*. BC Decker, 2003.

[25] M.J. Lind. Principles of cytotoxic chemotherapy. *Medicine*, 36(1):19–23, jan 2008.

[26] Kevin A. Camphausen and R. Coia Lawrence. Principles of Radiation Therapy. *Oncology*, 2009.

[27] L Leksell. Stereotactic radiosurgery. *Journal of Neurology, Neurosurgery & Psychiatry*, 46(9):797–803, sep 1983.

[28] Alain Gerbaulet. *The GEC ESTRO handbook of brachytherapy*. ESTRO, Brussel, 2002.

[29] D Hanahan and R A Weinberg. The hallmarks of cancer. *Cell*, 100(1):57–70, 2000.

[30] P Fedi, S R Tronick, and S A Aaronson. Growth factors. *Cancer medicine*, pages 41–64, 1997.

[31] D J Slamon, G M Clark, S G Wong, W J Levin, A Ullrich, and W L McGuire. Human breast cancer: correlation of relapse and survival with amplification of the HER-2/neu oncogene. *Science (New York, N.Y.)*, 235(4785):177–82, jan 1987.

[32] Yosef Yarden and Axel Ullrich. Growth Factor Receptor Tyrosine Kinases. *Annual Review of Biochemistry*, 57(1):443–478, jun 1988.

[33] P P Di Fiore, J H Pierce, M H Kraus, O Segatto, C R King, and S A Aaronson. erbB-2 is a potent oncogene when overexpressed in NIH/3T3 cells. *Science (New York, N.Y.)*, 237(4811):178–82, jul 1987.

[34] M E Lukashev and Z Werb. ECM signalling: orchestrating cell behaviour and misbehaviour. *Trends in cell biology*, 8(11):437–41, nov 1998.

[35] F G Giancotti and E Ruoslahti. Integrin signaling. *Science (New York, N.Y.)*, 285(5430):1028–32, aug 1999.

[36] Tony Hunter. Oncoprotein Networks. *Cell*, 88(3):333–346, feb 1997.

[37] K W Kinzler and B Vogelstein. Lessons from hereditary colorectal cancer. *Cell*, 87(2):159–70, oct 1996.

[38] Christian Rommel and Ernst Hafen. Ras - a versatile cellular switch. *Current Opinion in Genetics & Development*, 8(4):412–418, aug 1998.

[39] Julian Downward. Mechanisms and consequences of activation of protein kinase B/Akt. *Current Opinion in Cell Biology*, 10(2):262–267, apr 1998.

[40] M Skobe and N E Fusenig. Tumorigenic conversion of immortal human keratinocytes through stromal cell activation. *Proceedings of the National Academy of Sciences of the United States of America*, 95(3):1050–5, feb 1998.

[41] Kenneth W Kinzler and Bert Vogelstein. Landscaping the cancer terrain. *Science (New York, N.Y.)*, 280(5366):1036–7, 1998.

[42] A F Olumi, G D Grossfeld, S W Hayward, P R Carroll, T D Tlsty, and G R Cunha. Carcinoma-associated fibroblasts direct tumor progression of initiated human prostatic epithelium. *Cancer research*, 59(19):5002–11, oct 1999.

[43] J. D. Hudson, M A Shoaibi, R Maestro, A Carnero, G J Hannon, and D H Beach. A Proinflammatory Cytokine Inhibits p53 Tumor Suppressor Activity. *Journal of Experimental Medicine*, 190(10):1375–1382, nov 1999.

[44] L. M. Coussens, W. W. Raymond, G. Bergers, M. Laig-Webster, O. Behrendtsen, Z. Werb, G. H. Caughey, and D. Hanahan. Inflammatory mast cells up-regulate angiogenesis during squamous epithelial carcinogenesis. *Genes & Development*, 13(11):1382–1397, jun 1999.

[45] C. Cordon-Cardo and C Prives. At the Crossroads of Inflammation and Tumorigenesis. *Journal of Experimental Medicine*, 190(10):1367–1370, nov 1999.

[46] Robert A Weinberg. The retinoblastoma protein and cell cycle control. *Cell*, 81(3):323–330, may 1995.

[47] H L Moses, E Y Yang, and J A Pietenpol. TGF-beta stimulation and inhibition of cell proliferation: new mechanistic insights. *Cell*, 63(2):245–7, oct 1990.

[48] Gregory J. Hannon and David Beach. pl5INK4B is a potentia— effector of TGF-β-induced cell cycle arrest. *Nature*, 371(6494):257–261, sep 1994.

[49] M B Datto, P P Hu, T F Kowalik, J Yingling, and X F Wang. The viral oncoprotein E1A blocks transforming growth factor beta-mediated induction of p21/WAF1/Cip1 and p15/INK4B. *Molecular and cellular biology*, 17(4):2030–7, apr 1997.

[50] T M Fynan and M Reiss. Resistance to inhibition of cell growth by transforming growth factor-beta and its role in oncogenesis. *Critical reviews in oncogenesis*, 4(5):493–540, 1993.

[51] M Schutte, R H Hruban, L Hedrick, K R Cho, G M Nadasdy, C L Weinstein, G S Bova, W B Isaacs, P Cairns, H Nawroz, D Sidransky, R A Casero, P S Meltzer, S A Hahn, and S E Kern. DPC4 gene in various tumor types. *Cancer research*, 56(11):2527–30, jun 1996.

[52] Lynda Chin, Jason Pomerantz, and Ronald A DePinho. The INK4a/ARF tumor suppressor: one genetwo productstwo pathways. *Trends in Biochemical Sciences*, 23(8):291–296, aug 1998.

[53] Lin Zuo, John Weger, Qingbei Yang, Alisa M. Goldstein, Margaret A. Tucker, Graeme J. Walker, Nicholas Hayward, and Nicholas C. Dracopoli. Germline mutations in the p16INK4a binding domain of CDK4 in familial melanoma. *Nature Genetics*, 12(1):97–99, jan 1996.

[54] N Dyson, P M Howley, K Münger, and E Harlow. The human papilloma virus-16 E7 oncoprotein is able to bind to the retinoblastoma gene product. *Science (New York, N.Y.)*, 243(4893):934–7, feb 1989.

[55] S Markowitz, J Wang, L Myeroff, R Parsons, L Sun, J Lutterbaugh, R S Fan, E Zborowska, K W Kinzler, and B Vogelstein. Inactivation of the type II TGF-beta receptor in colon cancer cells with microsatellite instability. *Science (New York, N.Y.)*, 268(5215):1336–8, jun 1995.

[56] P Kahn, L Frykberg, C Brady, I Stanley, H Beug, B Vennström, and T Graf. v-erbA cooperates with sarcoma oncogenes in leukemic cell transformation. *Cell*, 45(3):349–56, may 1986.

[57] K W Kinzler and B Vogelstein. Lessons from hereditary colorectal cancer. *Cell*, 87(2):159–70, oct 1996.

[58] K P Foley and R N Eisenman. Two MAD tails: what the recent knockouts of Mad1 and Mxi1 tell us about the MYC/MAX/MAD network. *Biochimica et biophysica acta*, 1423(3):M37–47, may 1999.

[59] A H Wyllie, J F Kerr, and A R Currie. Cell death: the significance of apoptosis. *International review of cytology*, 68:251–306, 1980.

[60] Y Ishizaki, L Cheng, A W Mudge, and M C Raff. Programmed cell death by default in embryonic cells, fibroblasts, and cancer cells. *Molecular Biology of the Cell*, 6(11):1443–1458, nov 1995.

[61] G Evan and T Littlewood. A matter of life and cell death. *Science (New York, N.Y.)*, 281(5381):1317–22, aug 1998.

[62] A Ashkenazi and V M Dixit. Apoptosis control by death and decoy receptors. *Current opinion in cell biology*, 11(2):255–60, apr 1999.

[63] Alison J Butt, Sue M Firth, and Robert C Baxter. The IGF axis and programmed cell death. *Immunology and Cell Biology*, 77(3):256–262, jun 1999.

[64] J Lotem and L Sachs. Control of apoptosis in hematopoiesis and leukemia by cytokines, tumor suppressor and oncogenes. *Leukemia*, 10(6):925–31, jun 1996.

[65] D R Green and J C Reed. Mitochondria and apoptosis. *Science (New York, N.Y.)*, 281(5381):1309–12, aug 1998.

[66] N A Thornberry and Y Lazebnik. Caspases: enemies within. *Science (New York, N.Y.)*, 281(5381):1312–6, aug 1998.

[67] J F R Kerr, A H Wyllie, and A R Currie. Apoptosis: A Basic Biological Phenomenon with Wideranging Implications in Tissue Kinetics. *British Journal of Cancer*, 26(4):239–257, aug 1972.

[68] Gerhard Christofori, Paul Naik, and Douglas Hanahan. A second signal supplied by insulin-like growth factor II in oncogene-induced tumorigenesis. *Nature*, 369(6479):414–418, jun 1994.

[69] Andreas Strasser, Alan W. Harris, Mary L. Bath, and Suzanne Cory. Novel primitive lymphoid tumours induced in transgenic mice by cooperation between myc and bcl-2. *Nature*, 348(6299):331–333, nov 1990.

[70] S J Korsmeyer. Chromosomal Translocations in Lymphoid Malignancies Reveal Novel Proto-Oncogenes. *Annual Review of Immunology*, 10(1):785–807, apr 1992.

[71] David L. Vaux, Suzanne Cory, and Jerry M. Adams. Bcl-2 gene promotes haemopoietic cell survival and cooperates with c-myc to immortalize pre-B cells. *Nature*, 335(6189):440–442, sep 1988.

[72] Timothy J. McDonnell and Stanley J. Korsmeyer. Progression from lymphoid hyperplasia to high-grade malignant lymphoma in mice transgenic for the t(14;18). *Nature*, 349(6306):254–256, jan 1991.

[73] Robert M. Pitti, Scot A. Marsters, David A. Lawrence, Margaret Roy, Frank C. Kischkel, Patrick Dowd, Arthur Huang, Christopher J. Donahue, Steven W. Sherwood, Daryl T. Baldwin, Paul J. Godowski, William I. Wood, Austin L. Gurney, Kenneth J. Hillan, Robert L. Cohen, Audrey D. Goddard, David Botstein, and Avi Ashkenazi. Genomic amplification of a decoy receptor for Fas ligand in lung and colon cancer. *Nature*, 396(6712):699–703, dec 1998.

[74] J Downward. Mechanisms and consequences of activation of protein kinase B/Akt. *Current opinion in cell biology*, 10(2):262–7, apr 1998.

[75] G Evan and T Littlewood. A matter of life and cell death. *Science (New York, N.Y.)*, 281(5381):1317–22, aug 1998.

[76] A O Hueber, M Zörnig, D Lyon, T Suda, S Nagata, and G I Evan. Requirement for the CD95 receptor-ligand pathway in c-Myc-induced apoptosis. *Science (New York, N.Y.)*, 278(5341):1305–9, nov 1997.

[77] Curtis C. Harris. COMMENTARY: p ⁵³ Tumor suppressor gene: from the basic research laboratory to the clinican abridged historical perspective. *Carcinogenesis*, 17(6):1187–1198, 1996.

[78] A J Levine. p53, the cellular gatekeeper for growth and division. *Cell*, 88(3):323–31, feb 1997.

[79] H Symonds, L Krall, L Remington, M Saenz-Robles, S Lowe, T Jacks, and T Van Dyke. p53-dependent apoptosis suppresses tumor growth and progression in vivo. *Cell*, 78(4):703–11, aug 1994.

[80] L Hayflick. Mortality and immortality at the cellular level. A review. *Biochemistry. Biokhimiia*, 62(11):1180–90, nov 1997.

[81] C M Counter, A A Avilion, C E LeFeuvre, N G Stewart, C W Greider, C B Harley, and S Bacchetti. Telomere shortening associated with chromosome instability is arrested in immortal cells which express telomerase activity. *The EMBO journal*, 11(5):1921–9, may 1992.

[82] W E Wright, O M Pereira-Smith, and J W Shay. Reversible cellular senescence: implications for immortalization of normal human diploid fibroblasts. *Molecular and cellular biology*, 9(7):3088–92, jul 1989.

[83] G Bergers, D Hanahan, and L M Coussens. Angiogenesis and apoptosis are cellular parameters of neoplastic progression in transgenic mouse models of tumorigenesis. *The International journal of developmental biology*, 42(7):995–1002, 1998.

[84] M A Shibata, I G Maroulakou, C L Jorcyk, L G Gold, J M Ward, and J E Green. p53-independent apoptosis during mammary tumor progression in C3(1)/SV40 large T antigen transgenic mice: suppression of apoptosis during the transition from preneoplasia to carcinoma. *Cancer research*, 56(13):2998–3003, jul 1996.

[85] H Symonds, L Krall, L Remington, M Saenz-Robles, S Lowe, T Jacks, and T Van Dyke. p53-dependent apoptosis suppresses tumor growth and progression in vivo. *Cell*, 78(4):703–11, aug 1994.

[86] A H Wyllie, J F Kerr, and A R Currie. Cell death: the significance of apoptosis. *International review of cytology*, 68:251–306, 1980.

[87] J.W. Shay and S. Bacchetti. A survey of telomerase activity in human cancer. *European Journal of Cancer*, 33(5):787–791, apr 1997.

[88] Tracy M Bryan and Thomas R Cech. Telomerase and the maintenance of chromosome ends. *Current Opinion in Cell Biology*, 11(3):318–324, jun 1999.

[89] T M Bryan, A Englezou, J Gupta, S Bacchetti, and R R Reddel. Telomere elongation in immortal human cells without detectable telomerase activity. *The EMBO journal*, 14(17):4240–8, sep 1995.

[90] M Serrano, A W Lin, M E McCurrach, D Beach, and S W Lowe. Oncogenic ras provokes premature cell senescence associated with accumulation of p53 and p16INK4a. *Cell*, 88(5):593–602, mar 1997.

[91] J A Varner and D A Cheresh. Integrins and cancer. *Current opinion in cell biology*, 8(5):724–30, oct 1996.

[92] R O Hynes and D D Wagner. Genetic manipulation of vascular adhesion molecules in mice. *Journal of Clinical Investigation*, 98(10):2193–2195, nov 1996.

[93] William G. Stetler-Stevenson. Matrix metalloproteinases in angiogenesis: a moving target for therapeutic intervention. *Journal of Clinical Investigation*, 103(9):1237–1241, may 1999.

[94] N Bouck, V Stellmach, and S C Hsu. How tumors become angiogenic. *Advances in cancer research*, 69:135–74, 1996.

[95] D Hanahan and J Folkman. Patterns and emerging mechanisms of the angiogenic switch during tumorigenesis. *Cell*, 86(3):353–64, aug 1996.

[96] Louis M. Sherwood, Edith E. Parris, and Judah Folkman. Tumor Angiogenesis: Therapeutic Implications. *New England Journal of Medicine*, 285(21):1182–1186, nov 1971.

[97] Tanja Veikkola and Kari Alitalo. VEGFs, receptors and angiogenesis. *Seminars in Cancer Biology*, 9(3):211–220, jun 1999.

[98] K. Jin Kim, Bing Li, Jane Winer, Mark Armanini, Nancy Gillett, Heidi S. Phillips, and Napoleone Ferrara. Inhibition of vascular endothelial growth factor-induced angiogenesis suppresses tumour growth in vivo. *Nature*, 362(6423):841–844, apr 1993.

[99] Birgit Millauer, Laura K. Shawver, Karl H. Plate, Werner Risaui, and Axel Ullrich. Glioblastoma growth inhibited in vivo by a dominant-negative Flk-1 mutant. *Nature*, 367(6463):576–579, feb 1994.

[100] G Bergers, K Javaherian, K M Lo, J Folkman, and D Hanahan. Effects of angiogenesis inhibitors on multistage carcinogenesis in mice. *Science (New York, N.Y.)*, 284(5415):808–12, apr 1999.

[101] K M Dameron, O V Volpert, M A Tainsky, and N Bouck. Control of angiogenesis in fibroblasts by p53 regulation of thrombospondin-1. *Science (New York, N.Y.)*, 265(5178):1582–4, sep 1994.

[102] J Rak, J Filmus, G Finkenzeller, S Grugel, D Marmé, and R S Kerbel. Oncogenes as inducers of tumor angiogenesis. *Cancer metastasis reviews*, 14(4):263–77, dec 1995.

[103] Patrick H. Maxwell, Michael S. Wiesener, Gin-Wen Chang, Steven C. Clifford, Emma C. Vaux, Matthew E. Cockman, Charles C. Wykoff, Christopher W. Pugh, Eamonn R. Maher, and Peter J. Ratcliffe. The tumour suppressor protein VHL targets hypoxia-inducible factors for oxygen-dependent proteolysis. *Nature*, 399(6733):271–275, may 1999.

[104] S. Gately, P. Twardowski, M. S. Stack, D. L. Cundiff, D. Grella, F. J. Castellino, J. Enghild, H. C. Kwaan, F. Lee, R. A. Kramer, O. Volpert, N. Bouck, and G. A. Soff. The mechanism of cancer-mediated conversion of plasminogen to the angiogenesis inhibitor angiostatin. *Proceedings of the National Academy of Sciences*, 94(20):10868–10872, sep 1997.

[105] John M. Whitelock, Alan D. Murdoch, Renato V. Iozzo, and P. Anne Underwood. The Degradation of Human Endothelial Cell-derived Perlecan and Release of Bound Basic Fibroblast Growth Factor by Stromelysin, Collagenase, Plasmin, and Heparanases. *Journal of Biological Chemistry*, 271(17):10079–10086, apr 1996.

[106] NCI. Metastatic Cancer - National Cancer Institute, 2017.

[107] M B Sporn. The war on cancer. *Lancet (London, England)*, 347(9012):1377–81, may 1996.

[108] A E Aplin, A Howe, S K Alahari, and R L Juliano. Signal transduction and signal modulation by cell adhesion receptors: the role of integrins, cadherins, immunoglobulin-cell adhesion molecules, and selectins. *Pharmacological reviews*, 50(2):197–263, jun 1998.

[109] G Christofori and H Semb. The role of the cell-adhesion molecule E-cadherin as a tumour-suppressor gene. *Trends in biochemical sciences*, 24(2):73–6, feb 1999.

[110] J P Johnson. Cell adhesion molecules of the immunoglobulin supergene family and their role in malignant transformation and progression to metastatic disease. *Cancer metastasis reviews*, 10(1):11–22, may 1991.

[111] Ulrich Kaiser, Bernhard Auerbach, and Marcus Oldenburg. The neural cell adhesion molecule NCAM in multiple myeloma. *Leukemia & Lymphoma*, 20(5-6):389–395, jan 1996.

[112] P Fogar, D Basso, C Pasquali, M De Paoli, C Sperti, G Roveroni, S Pedrazzoli, and M Plebani. Neural cell adhesion molecule (N-CAM) in gastrointestinal neoplasias. *Anticancer research*, 17(2B):1227–30, 1997.

[113] Anne-Karina Perl, Ulf Dahl, Petra Wilgenbus, Harold Cremer, Henrik Semb, and Gerhard Christofori. Reduced expression of neural cell adhesion molecule induces metastatic dissemination of pancreatic β tumor cells. *Nature Medicine*, 5(3):286–291, mar 1999.

[114] L M Coussens and Z Werb. Matrix metalloproteinases and the development of cancer. *Chemistry & biology*, 3(11):895–904, nov 1996.

[115] A. F. Chambers and L. M. Matrisian. Changing views of the role of matrix metalloproteinases in metastasis. *JNCI Journal of the National Cancer Institute*, 89(17):1260–1270, sep 1997.

[116] Z Werb. ECM and cell surface proteolysis: regulating cellular ecology. *Cell*, 91(4):439–42, nov 1997.

[117] M Johnsen, L R Lund, J Rømer, K Almholt, and K Danø. Cancer invasion and tissue remodeling: common themes in proteolytic matrix degradation. *Current opinion in cell biology*, 10(5):667–71, oct 1998.

[118] CDC. FastStats - Health Expenditures, 2016.

[119] Cathy J Bradley, K Robin Yabroff, Bassam Dahman, Eric J Feuer, Angela Mariotto, and Martin L Brown. Productivity costs of cancer mortality in the United States: 2000-2020. *Journal of the National Cancer Institute*, 100(24):1763–70, dec 2008.

[120] M.N. Tsao, D. Rades, A. Wirth, S.S. Lo, B.L. Danielson, A. Vichare, C. Hahn, and E.L. Chang. International Practice Survey on the Management of Brain Metastases: Third International Consensus Workshop on Palliative Radiotherapy and Symptom Control. *Clinical Oncology*, 24(6):e81–e92, aug 2012.

[121] A A F De Salles, A A Gorgulho, M Selch, J De Marco, and N Agazaryan. Radiosurgery from the brain to the spine: 20 years experience. *Acta neurochirurgica. Supplement*, 101:163–8, 2008.

[122] Andrew Wu, G. Lindner, A. H. Maitz, A. M. Kalend, L. D. Lunsford, J. C. Flickinger, and W. D. Bloomer. Physics of gamma knife approach on convergent beams in stereotactic radiosurgery. *International Journal of Radiation Oncology, Biology, Physics*, 18(4):941–949, apr 1990.

[123] Christer Lindquist and Ian Paddick. The Leksell Gamma Knife Perfexion and comparisons with its predecessors. *Operative Neurosurgery*, 61(September):130–141, 2007.

[124] Jean Régis, Manabu Tamura, Cécile Guillot, Shoji Yomo, Xavier Muraciolle, Mariko Nagaje, Yasser Arka, and Denis Porcheron. Radiosurgery with the world's first fully robotized leksell gamma knife perfeXion in clinical use: A 200-patient prospective, randomized, controlled comparison with the gamma knife 4C. *Neurosurgery*, 64(2):346–355, 2009.

[125] Christer Lindquist, Lars Kihlström, and Erik Hellstrand. Functional Neurosurgery - A Future for the Gamma Knife? *Stereotactic and Functional Neurosurgery*, 57(1-2):72–81, feb 1992.

[126] S.J. J. Goetsch, B.D. D. Murphy, R. Schmidt, J. Micka, L. De Werd, Y. Chen, and S. Shockley. Physics of rotating gamma systems for stereotactic radiosurgery. *International Journal of Radiation Oncology Biology Physics*, 43(3):689–696, 1999.

[127] Hideo D. Kubo and Fujio Araki. Dosimetry and mechanical accuracy of the first rotating gamma system installed in North America. *Medical Physics*, 29(11), oct 2002.

[128] J. Y. C. Cheung and K. N. Yu. Rotating and static sources for gamma knife radiosurgery systems: Monte Carlo studies. *Medical Physics*, 33(7Part1):2500–2505, jun 2006.

[129] Yuan Tian, Huidong Wang, Yingjie Xu, Hui Yan, Yixin Song, Kuo Men, Pan Ma, Xinxin Ren, Minghui Li, Ke Zhang, and Jianrong Dai. Comparison of dosimetric characteristics between stationary and rotational gamma ray stereotactic radiosurgery systems based on Monte Carlo simulation. *Biomedical Physics & Engineering Express*, 2(4):045014, aug 2016.

[130] Jolyon H Hendry, Steven L Simon, Andrzej Wojcik, Mehdi Sohrabi, Werner Burkart, Elisabeth Cardis, Dominique Laurier, Margot Tirmarche, and Isamu Hayata. Human exposure to high natural background radiation: what can it teach us about radiation risks? *Journal of Radiological Protection*, 29(2A):A29–A42, jun 2009.

[131] Richard Dean. Burns and Joseph M. Siracusa. *A global history of the nuclear arms race : weapons, strategy, and politics*. Praeger, 2013.

[132] H. Dolk and R. Nichols. Evaluation of the impact of Chernobyl on the prevalence of congenital anomalies in 16 regions of Europe. EUROCAT Working Group. *International Journal of Epidemiology*, 28(5):941–948, oct 1999.

[133] Douglas Almond, Lena Edlund, and Mårten Palme. Chernobyl's Subclinical Legacy: Prenatal Exposure to Radioactive Fallout and School Outcomes in Sweden [*]. *Quarterly Journal of Economics*, 124(4):1729–1772, nov 2009.

[134] Ray Appleyard. The birth of UNSCEARthe midwife's tale. *Journal of Radiological Protection*, 30(3):621–626, sep 2010.

[135] M. Krishnan Nair, K. S. V. Nambi, N. Sreedevi Amma, P. Gangadharan, P. Jayalekshmi, S. Jayadevan, Varghese Cherian, and K. Nair Reghuram. Population Study in the High Natural Background Radiation Area in Kerala, India. *Radiation Research*, 152(6):S145, dec 1999.

[136] Mehdi Sohrabi. The state-of-the-art on worldwide studies in some environments with elevated naturally occurring radioactive materials (NORM). *Applied Radiation and Isotopes*, 49(3):169–188, mar 1998.

[137] Mira Maalouf, Marco Durante, and Nicolas Foray. Biological Effects of Space Radiation on Human Cells: History, Advances and Outcomes. *Journal of Radiation Research*, 52(2):126–146, mar 2011.

[138] Carl Alexander Lindburg, Jeffrey S. Willey, and Delphine Dean. Effects of low dose X-ray irradiation on porcine articular cartilage explants. *Journal of Orthopaedic Research*, 31(11):n/a–n/a, aug 2013.

[139] Eun-Hee Hong, Su-Jae Lee, Jae-Sung Kim, Kee-Ho Lee, Hong-Duck Um, Jae-Hong Kim, Song-Ja Kim, Jong-Il Kim, and Sang-Gu Hwang. Ionizing radiation induces cellular senescence of articular chondrocytes via negative regulation of SIRT1 by p38 kinase. *The Journal of biological chemistry*, 285(2):1283–95, jan 2010.

[140] Jeffrey S. Willey, David L. Long, Kadie S. Vanderman, and Richard F. Loeser. Ionizing radiation causes active degradation and reduces matrix synthesis in articular cartilage. *International Journal of Radiation Biology*, 89(4):268–277, apr 2013.

[141] Maria Kyriakidou, Andreas F Mavrogenis, Stylianos Kyriazis, Athina Markouizou, Theophile Theophanides, and Jane Anastassopoulou. An FT-IR Spectral Analysis of the Effects of γ-Radiation on Normal and Cancerous Cartilage. *In vivo (Athens, Greece)*, 30(5):599–604, sep 2016.

[142] T Matsumoto, K Iwasaki, and H Sugihara. Effects of radiation on chondrocytes in culture. *Bone*, 15(1):97–100, 2012.

[143] B. S. Margulies, J. A. Horton, Y. Wang, T. A. Damron, and M. J. Allen. Effects of Radiation Therapy on Chondrocytes In Vitro. *Calcified Tissue International*, 78(5):302–313, may 2006.

[144] Eun-Hee Hong, Jie-Young Song, Su-Jae Lee, In-Chul Park, Hong-Duck Um, Jong Kuk Park, Kee-Ho Lee, Seon Young Nam, and Sang-Gu Hwang. Low-dose γ-radiation inhibits IL-1β-induced dedifferentiation and inflammation of articular chondrocytes via blockage of catenin signaling. *IUBMB Life*, 66(2):128–137, feb 2014.

[145] Paul K. Holden, Chao Li, Victor Da Costa, Chung-Ho Sun, Susan V. Bryant, David M. Gardiner, and Brian J.F. Wong. The effects of laser irradiation of cartilage on chondrocyte gene expression and the collagen matrix. *Lasers in Surgery and Medicine*, 41(7):487–491, sep 2009.

[146] Ian D. Hutchinson, John Olson, Carl A. Lindburg, Valerie Payne, Boyce Collins, Thomas L. Smith, Michael T. Munley, Kenneth T. Wheeler, and Jeffrey S. Willey. Total-body irradiation produces late degenerative joint damage in rats. *International Journal of Radiation Biology*, 90(9):821–830, sep 2014.

[147] C Steffen, C Müller, K Stellamor, and J Zeitlhofer. Influence of x-ray treatment on antigen-induced experimental arthritis. *Annals of the rheumatic diseases*, 41(5):532–7, oct 1982.

[148] Shane Cloude. *An Introduction to Electromagnetic Wave Propagation and Antennas*. Springer Science and Business Media, 1995.

[149] Alessandro Bettini. *A Course in Classical Physics, Vol. 4 - Waves and Light*. Springer, 2016.

[150] David J. Griffiths. *Introduction to Electrodynamics*. Pearson, 4th edition, 2013.

[151] Gosta Ekspong. The dual nature of light as reflected in the Nobel archives, 2017.

[152] Richard Feynman. *QED: The strange theory of light and matter*. Princeton University Press, 2006.

[153] Paul A. Tipler. *Physics for Scientists and Engineers: Vol. 1: Mechanics, Oscillations and Waves, Thermodynamics*. MacMillan, 1999.

[154] C. Cohen-Tannoudji. *Quantum Mechanics*. Wiley, second edition, 1977.

[155] Walter Greiner. *Quantum Mechanics: An Introduction*. Springer, 2001.

[156] Manjit Kumar. *Quantum: Einstein, Bohr, and the Great Debate about the Nature of Reality (Reprint ed.)*. W. W. Norton & Company, 2011.

[157] Berkley Lab. Electromagnetic Spectrum.

[158] Glenn F. Knoll. *Radiation detection and Measurement*. John Wiley & Sons, Ltd, second edition, 1989.

[159] J. R. (Jerry R.) Williams and D. I. Thwaites. *Radiotherapy physics–in practice*. Oxford University Press, 2000.

[160] John. Daintith and Oxford University Press. *A dictionary of physics*. Oxford University Press, 2009.

[161] A. Allisy. Henri Becquerel: The Discovery of Radioactivity. *Radiation Protection Dosimetry*, 68(1):3–10, nov 1996.

[162] Jake Blanchard. Pure Beta Emitters.

[163] Michael F.L'Annunziata. Radiation Physics and Radionuclide Decay. In *Handbook of Radioactivity Analysis*, pages 1–162. Academic Press, jan 2012.

[164] Kenneth S. Krane and David Halliday. *Introductory nuclear physics*. Wiley, 1988.

[165] Radioactive Decay Data.

[166] Peter Lux. Very Heavy Atoms Fission — Peter Lux.

[167] J.P. Mason. A 6130 keV gamma-ray source using the 13C(α, n)16O reaction. *Nuclear Instruments and Methods in Physics Research Section A: Accelerators, Spectrometers, Detectors and Associated Equipment*, 241(1):207–209, nov 1985.

[168] X-rays.

[169] X-Ray Transition Energies Database — NIST.

[170] Lucien Pages, Evelyne Bertel, Henri Joffre, and Laodamas Sklavenitis. Energy loss, range, and bremsstrahlung yield for 10-keV to 100-MeV electrons in various elements and chemical compounds. *Atomic Data and Nuclear Data Tables*, 4:1–27, mar 1972.

[171] T. Mukoyama. Range of electrons and positrons. *Nuclear Instruments and Methods*, 134(1):125–127, apr 1976.

[172] Glenn F. Knoll. Neutron Sources for Basic Physics and Applications. *Radioisotope Neutron Sources*, 1983.

[173] Michael C Lederer and Virginia S Shirley, editors. *Table of Isotopes*. Wiley, New York, 7th edition, 1978.

[174] Robley D. Evans. *The Atomic Nucleus*. Krieger, New York, 1982.

[175] Douglas Wagenaar. 7.1.3 The Bragg Curve. *Radiation Physics Principles*, 1995.

[176] Berend Wilken and Theodore A. Fritz. Energy distribution functions of low energy ions in silicon absorbers measured for large relative energy losses. *Nuclear Instruments and Methods*, 138(2):331–343, oct 1976.

[177] US Department of Health. Radiological health handbook : United States. Bureau of Radiological Health : Internet Archive, 1970.

[178] Hans Henrik. Andersen and J. F. (James F.) Ziegler. *Hydrogen stopping powers and ranges in all elements*. Pergamon Press, 1977.

[179] C. Williamson, J. Boujot, and J. Picard. Tables of range and stopping power of chemical elements for charged particles of energy 0.5 to 500 MeV, 1966.

[180] Claus Hanke and Jens Laursen. Stopping cross sections for α particles from 1.0 to 8.5 MeV in H2, He, N2, O2, Ne, Kr and Xe. *Nuclear Instruments and Methods*, 151(1-2):253–260, may 1978.

[181] Walter H. Barkas and Martin J. Berger. Tables of energy losses and ranges of heavy charged particles. In *Studies in Penetration of Charged Particles in Matter - National Research Council (U.S.). Committee on Nuclear Science*, chapter 7, page 398. National Research Council, 1964.

[182] L.C. Northcliffe and R.F. Schilling. Range and stopping-power tables for heavy ions. *Atomic Data and Nuclear Data Tables*, 7(3-4):233–463, jan 1970.

[183] 7_2.2 Scaling Laws.

[184] T. Tabata, R. Ito, and S. Okabe. An empirical equation for the backscattering coefficient of electrons. *Nuclear Instruments and Methods*, 94(3):509–513, jul 1971.

[185] The Nobel Prize in Physics 1921.

[186] G. Harding and E. Harding. Compton scatter imaging: A tool for historical exploration. *Applied Radiation and Isotopes*, 68(6):993–1005, jun 2010.

[187] Interaction of Gamma Radiation with Matter.

[188] DoITPoMS - TLP Library Materials for Nuclear Power Generation - Cross-Sections.

[189] Faiz M. Khan. *The physics of radiation therapy*. Lippincott Williams & Wilkins, 2014.

[190] Erythema and skin injuries — IAEA.

[191] International Commission on Radiation Units and Measurements (ICRU).

[192] F W Spiers. Radiation units and the measurement of ionizing radiation. *Physics Education*, 6(5):001, sep 1971.

[193] A. McNair. ICRU Report 33 - Radiation Quantities and Units Pub: International Commission on Radiation Units and Measurements, Washington D.C. USA issued 15 April 1980, pp.25. *Journal of Labelled Compounds and Radiopharmaceuticals*, 18(9):1398–1398, sep 1981.

[194] M Boutillon and A M Perroche-Roux. Re-evaluation of the W value for electrons in dry air. *Physics in Medicine and Biology*, 32(2):213–219, feb 1987.

[195] Robert Loevinger. A formalism for calculation of absorbed dose to a medium from photon and electron beams. *Medical Physics*, 8(1):1–12, jan 1981.

[196] T.P Loftus and J.T. Weaver. Standardization of 60Co and 137Cs gamma-ray beams in terms of exposure. *Journal of Research of the National Bureau of Standards*, 78A(4):465, 1974.

[197] AAPM. A protocol for the determination of absorbed dose from high-energy photon and electron beams. *Medical Physics*, 10(6):741–771, nov 1983.

[198] NRC: Home Page.

[199] National Council on Radiation Protection & Measurements — Bethesda, MD.

[200] National Council on Radiation Protection and Measurements. *Limitation of exposure to ionizing radiation : recommendations of the National Council on Radiation Protection and Measurements.* The Council, 1993.

[201] International Atomic Energy Agency — Atoms for Peace and Development.

[202] IAEA. *IAEA Safety Glossary.* Non-serial Publications. INTERNATIONAL ATOMIC ENERGY AGENCY, Vienna, 2007.

[203] United Nations. Scientific Committee on the Effects of Atomic Radiation. *Sources and effects of ionizing radiation : United Nations Scientific Committee on the Effects of Atomic Radiation : UNSCEAR 2008 report to the General Assembly, with scientific annexes.* United Nations, 2010.

[204] National Council on Radiation Protection and Measurements., National Council on Radiation Protection and Measurements. Scientific Committee 6-2 on Radiation Exposure of the U.S. Population., and National Council on Radiation Protection and Measurements. *Ionizing radiation exposure of the population of the United States.* National Council on Radiation Protection and Measurements, 2009.

[205] US_EPA_OAR. *A Citizen's Guide to Radon: The Guide to Protecting Yourself and Your Family from Radon.* EPA, 2016.

[206] D A Schauer and O W Linton. NCRP Report No. 160, Ionizing Radiation Exposure of the Population of the United States, medical exposure–are we doing less with more, and is there a role for health physicists? *Health physics*, 97(1):1–5, jul 2009.

[207] Taishitsu.or.jp. Annual terrestrial radiation doses in the world, 2007.

[208] UNSCEAR. Sources and effects of ionizing radiation. Technical report, United Nations Scientific Committee of Effect of Atomic Radiation, 1993.

[209] Su-ping Zhang, Zhao-zhao Wu, Yan-wen Wu, Shi-biao Su, and Jian Tong. [Mechanism study of adaptive response in high background radiation area of Yangjiang in China]. *Zhonghua yu fang yi xue za zhi [Chinese journal of preventive medicine]*, 44(9):815–9, sep 2010.

[210] A.C. Freitas and A.S. Alencar. Gamma dose rates and distribution of natural radionuclides in sand beachesIlha Grande, Southeastern Brazil. *Journal of Environmental Radioactivity*, 75(2):211–223, jan 2004.

[211] Danilo C. Vasconcelos, Arno H. Oliveira, Mario R. S. Silva, Rodrigo Penna, Talita O. Santos, Claubia Pereira, Zildete Rocha, and Maaria Angela B. C. Menezes. Natural Radioactivity in extreme south of Bahia, Brazil using gamma-ray spectrometry. In *International Nuclear Atlantic Conference*, Rio de Janeiro, 2009.

[212] UNSCEAR. Sources and Effects of Ionizing Radiation. Technical report, United Nations Scientific Committee of Effect of Atomic Radiation, 2008.

[213] V.P. Bond, R.E. Albert, A.W. Guy, J. Kastner, and R.O. McClellan. Perceptions of Risk. In *Proceedings of the National Council on Radiation Protection and Measurements, Washington, DC; 1980*, Bethesda, MD, 1980.

[214] P J Oksanen. Estimated individual annual cosmic radiation doses for flight crews. *Aviation, space, and environmental medicine*, 69(7):621–5, jul 1998.

[215] W Friedberg, K Copeland, F E Duke, K O'Brien, and E B Darden. Radiation exposure during air travel: guidance provided by the Federal Aviation Administration for air carrier crews. *Health physics*, 79(5):591–5, nov 2000.

[216] M Waters, T F Bloom, and B Grajewski. The NIOSH/FAA Working Women's Health Study: evaluation of the cosmic-radiation exposures of flight attendants. Federal Aviation Administration. *Health physics*, 79(5):553–9, nov 2000.

[217] J F Bottollier-Depois, Q Chau, P Bouisset, G Kerlau, L Plawinski, and L Lebaron-Jacobs. Assessing exposure to cosmic radiation during long-haul flights. *Radiation research*, 153(5 Pt 1):526–32, may 2000.

[218] Ying-jin Feng, Wei-ru Chen, Tian-ping Sun, Shi-ying Duan, Bao-shan Jia, and Hai-li Zhang. [Estimated cosmic radiation doses for flight personnel]. *Hang tian yi xue yu yi xue gong cheng = Space medicine & medical engineering*, 15(4):265–9, aug 2002.

[219] Background Radiation and Other Sources of Exposure, 2016.

[220] Radiation in Everyday Life — IAEA.

[221] Health Physics Society. Are Our Bodies Radioactive?, 2016.

[222] UNSCEAR. Ionizing Radiation: Sources and Biological effects. Technical report, UNSCEAR, 1982.

[223] R E Toohey, A T Keane, and J Rundo. Measurement techniques for radium and the actinides in man at the Center for Human Radiobiology. *Health physics*, 44 Suppl 1:323–41, 1983.

[224] Yuri Kageyama. A-bombs vs. H-bombs: What's thedifference? - The Globe and Mail, 2016.

[225] Natural Resource Defense Council. NRDC: Nuclear Data - Table of Known Nuclear Tests Worldwide, 1945-1996, 2007.

[226] Atomic Heritage Foundation. Limited or Partial Test Ban Treaty (LTBT/PTBT) — Atomic Heritage Foundation, 2016.

[227] US Department of State. Limited Test Ban Treaty.

[228] UNSCEAR. Vol. I: Sources and Effects of Ionizing Radiation. Technical report, United Nations Scientific Committee on the effect of Atomic Radiation, 2000.

[229] Zhores A. Medvedev. *The legacy of Chernobyl*. W.W. Norton & Co, 1992.

[230] Michael Winter. Report: Emissions from Japan plant approach Chernobyl levels, 2011.

[231] Deborah MacKenzie. Fukushima radioactive fallout nears Chernobyl levels — New Scientist, 2011.

[232] Ken O Buesseler, Steven R Jayne, Nicholas S Fisher, Irina I Rypina, Hannes Baumann, Zofia Baumann, Crystaline F Breier, Elizabeth M Douglass, Jennifer George, Alison M Macdonald, Hiroomi Miyamoto, Jun Nishikawa, Steven M Pike, and Sashiko Yoshida. Fukushima-derived radionuclides in the ocean and biota off Japan. *Proceedings of the National Academy of Sciences of the United States of America*, 109(16):5984–8, apr 2012.

[233] Lauren Tousignant. Radiation from Fukushima disaster reaches the US, 2016.

[234] Matthew L. Wald. Low Levels of Radiation Found in American Milk - The New York Times, 2011.

[235] B. F. Wall. Ionising radiation exposure of the population of the United States: NCRP Report No. 160. *Radiation Protection Dosimetry*, 136(2):136–138, sep 2009.

[236] Fred A. Mettler, Mythreyi Bhargavan, Keith Faulkner, Debbie B. Gilley, Joel E. Gray, Geoffrey S. Ibbott, Jill A. Lipoti, Mahadevappa Mahesh, John L. McCrohan, Michael G. Stabin, Bruce R. Thomadsen, and Terry T. Yoshizumi. Radiologic and Nuclear Medicine Studies in the United States and Worldwide: Frequency, Radiation Dose, and Comparison with Other Radiation Sources19502007. *Radiology*, 253(2):520–531, nov 2009.

[237] B F Wall and D Hart. Revised radiation doses for typical X-ray examinations. Report on a recent review of doses to patients from medical X-ray examinations in the UK by NRPB. National Radiological Protection Board. *The British journal of radiology*, 70(833):437–9, may 1997.

[238] D. (David) Hart, B. F. Wall, and Great Britain. National Radiological Protection Board. *Radiation exposure of the UK population from medical and dental X-ray examinations*. National Radiological Protection Board, 2002.

[239] RSNA and ACR. Patient Safety - Radiation Dose in X-Ray and CT Exams.

[240] United Nations. Report of the United Nations Scientific Committee on the Effects of Atomic Radiation. Technical report, United Nations Scientific Committee on the Effect of Atomic Radiation, 1958.

[241] United Nations. Report of the United Nations Scientific Committee on the Effects of Atomic Radiation. Technical report, United Nations Scientific Committee on the Effect of Atomic Radiation, 1962.

[242] United Nations. Report of the United Nations Scientific Committee on the Effects of Atomic Radiation. Technical report, United Nations Scientific Committee on the Effect of Atomic Radiation, 1966.

[243] United Nations. Report of the United Nations Scientific Committee on the effects of Atomic Radiation. Technical report, United Nations Scientific Committee on the Effect of Atomic Radiation, 1969.

[244] United Nations. Effects of atomic radiation., 1969.

[245] CDC. CDC Radiation Emergencies — Acute Radiation Syndrome: A Fact Sheet for Physicians.

[246] Kate-Louise D Gottfried and Gary Penn, editors. *Radiation in Medicine: A Need for Regulatory Reform*. The National Academies Press, Washington, DC, 1996.

[247] Inge Schmitz-Feuerhake, Christopher Busby, and Sebastian Pflugbeil. Genetic radiation risks: a neglected topic in the low dose debate. *Environmental health and toxicology*, 31:e2016001, 2016.

[248] National Research Council (U.S.). Committee to Assess Health Risks from Exposure to Low Level of Ionizing Radiation. *Health risks from exposure to low levels of ionizing radiation : BEIR VII, Phase 2*. National Academies Press, 2006.

[249] Kedar N Prasad, William C Cole, and Gerald M Hasse. Health risks of low dose ionizing radiation in humans: a review. *Experimental biology and medicine (Maywood, N.J.)*, 229(5):378–82, may 2004.

[250] Bernard L. Cohen. Cancer Risk from Low-Level Radiation. *American Journal of Roentgenology*, 179(5):1137–1143, nov 2002.

[251] The Cancer Risk From Low Level Radiation: A Review of Recent Evidence.

[252] R L Brent. The effect of embryonic and fetal exposure to x-ray, microwaves, and ultrasound: counseling the pregnant and nonpregnant patient about these risks. *Seminars in oncology*, 16(5):347–68, oct 1989.

[253] V BIER. Other Somatic and Fetal Effects. Technical report, National Research Council (US) Committee on the Biological Effects of Ionizing Radiation (BEIR V), Washington, D.C., 1990.

[254] Cynthia H. McCollough, Beth A. Schueler, Thomas D. Atwell, Natalie N. Braun, Dawn M. Regner, Douglas L. Brown, and Andrew J. LeRoy. Radiation Exposure and Pregnancy: When Should We Be Concerned? *RadioGraphics*, 27(4):909–917, jul 2007.

[255] Palma Shaw, Audra Duncan, Ageliki Vouyouka, and Kathleen Ozsvath. Radiation exposure and pregnancy. *Journal of Vascular Surgery*, 53(1):28S–34S, jan 2011.

[256] Alex Comfort. Natural Aging and the Effects of Radiation. *Radiation Research Supplement*, 1:216, 1959.

[257] Richard B Richardson. Ionizing radiation and aging: rejuvenating an old idea. *Aging*, 1(11):887–902, nov 2009.

[258] Laia Hernández, Mariona Terradas, Jordi Camps, Marta Martín, Laura Tusell, and Anna Genescà. Aging and radiation: bad companions. *Aging cell*, 14(2):153–61, apr 2015.

[259] Ronald Kathren. Historical Development of the Linear Nonthreshold Dose-Response Model as Applied to Radiation. *The University of New Hampshire Law Review*, 1(1), dec 2002.

[260] James F. Crow and Seymour Abrahamson. Seventy Years Ago: Mutation Becomes Experimental. *Genetics*, 147(4), 1997.

[261] H. J. Muller. ARTIFICIAL TRANSMUTATION OF THE GENE. *Science*, 66(1699):84–87, jul 1927.

[262] Paul Langley. Muller's Nobel lecture , December 12, 1946 The Production of Mutations — Paul Langley's Nuclear History Blog, 2013.

[263] Egon Lorenz, Joanne Weikel Hollcroft, Eliza Miller, Charles C. Congdon, and Robert Schweisthal. Long-Term Effects of Acute and Chronic Irradiation in Mice. I. Survival and Tumor Incidence Following Chronic Irradiation of 0.11 r Per Day. *JNCI: Journal of the National Cancer Institute*, 15(4):1049–1058, feb 1955.

[264] Maurice Tubiana, Ludwig E. Feinendegen, Chichuan Yang, and Joseph M. Kaminski. The Linear No-Threshold Relationship Is Inconsistent with Radiation Biologic and Experimental Data. *Radiology*, 251(1):13–22, apr 2009.

[265] UNSCEAR. The Effects of Atomic Radiation. Technical report, United Nations Scientific Committee on the Effects of Atomic Radiation, 1958.

[266] NRC. *Health Risks from Exposure to Low Levels of Ionizing Radiation: BEIR VII Phase 2*. The National Academies Press, Washington, DC, 2006.

[267] A C Upton. Radiobiological effects of low doses. Implications for radiological protection. *Radiation research*, 71(1):51–74, jul 1977.

[268] J. Martin Brown. The Shape of the Dose-Response Curve for Radiation Carcinogenesis: Extrapolation to Low Doses. *Radiation Research*, 71(1):34, jul 1977.

[269] H R Withers. Response of tissues to multiple small dose fractions. *Radiation research*, 71(1):24–33, jul 1977.

[270] M M Elkind. The initial part of the survival curve. Implications for low-dose, low-dose-rate radiation responses. *Radiation research*, 71(1):9–23, jul 1977.

[271] Antony M. Hooker, Madhava Bhat, Tanya K. Day, Joanne M. Lane, Sarah J. Swinburne, Alexander A. Morley, and Pamela J. Sykes. The Linear No-Threshold Model does not Hold for Low-Dose Ionizing Radiation. *Radiation Research*, 162(4):447–452, oct 2004.

[272] S.M.J. Mortazavi, M. Ghiassi-Nejad, and M. Rezaiean. Cancer risk due to exposure to high levels of natural radon in the inhabitants of Ramsar, Iran. *International Congress Series*, 1276:436–437, feb 2005.

[273] Alireza Mosavi-Jarrahi, Mohammadali Mohagheghi, Suminori Akiba, Bahareh Yazdizadeh, Nilofar Motamedi, and Ali Shabestani Monfared. Mortality and morbidity from cancer in the population exposed to high level of natural radiation area in Ramsar, Iran. *International Congress Series*, 1276:106–109, feb 2005.

[274] Raghu Ram K Nair, Balakrishnan Rajan, Suminori Akiba, P Jayalekshmi, M Krishnan Nair, P Gangadharan, Taeko Koga, Hiroshige Morishima, Seiichi Nakamura, and Tsutomu Sugahara. Background radiation and cancer incidence in Kerala, India-Karanagappally cohort study. *Health physics*, 96(1):55–66, jan 2009.

[275] Hiroshi Tanooka. Meta-analysis of non-tumour doses for radiation-induced cancer on the basis of dose-rate. *International Journal of Radiation Biology*, 87(7):645–652, jul 2011.

[276] Mehdi Sohrabi and Mozhgan Babapouran. New public dose assessment from internal and external exposures in low- and elevated-level natural radiation areas of Ramsar, Iran. *International Congress Series*, 1276:169–174, feb 2005.

[277] V Odlind and A Ericson. Incidence of legal abortion in Sweden after the Chernobyl accident. *Biomedicine & Pharmacotherapy*, 45(6):225–228, jan 1991.

[278] Mikko Myrskylä, Karri Silventoinen, Per Tynelius, and Finn Rasmussen. Is Later Better or Worse? Association of Advanced Parental Age With Offspring Cognitive Ability Among Half a Million Young Swedish Men. *American Journal of Epidemiology*, 177(7):649–655, apr 2013.

[279] J. Little. The Chernobyl accident, congenital anomalies and other reproductive outcomes. *Paediatric and Perinatal Epidemiology*, 7(2):121–151, apr 1993.

[280] Mark S Pearce, Jane A Salotti, Mark P Little, Kieran McHugh, Choonsik Lee, Kwang Pyo Kim, Nicola L Howe, Cecile M Ronckers, Preetha Rajaraman, Alan W Craft, Louise Parker, and Amy Berrington de González. Radiation exposure from CT scans in childhood and subsequent risk of leukaemia and brain tumours: a retrospective cohort study. *The Lancet*, 380(9840):499–505, aug 2012.

[281] John D Mathews, Anna V Forsythe, Zoe Brady, Martin W Butler, Stacy K Goergen, Graham B Byrnes, Graham G Giles, Anthony B Wallace, Philip R Anderson, Tenniel A Guiver, Paul McGale, Timothy M Cain, James G Dowty, Adrian C Bickerstaffe, and Sarah C Darby. Cancer risk in 680,000 people exposed to computed tomography scans in childhood or adolescence: data linkage study of 11 million Australians. *BMJ (Clinical research ed.)*, 346:f2360, may 2013.

[282] Teresa Neumaier, Joel Swenson, Christopher Pham, Aris Polyzos, Alvin T Lo, PoAn Yang, Jane Dyball, Aroumougame Asaithamby, David J Chen, Mina J Bissell, Stefan Thalhammer, and Sylvain V Costes. Evidence for formation of DNA repair centers and dose-response nonlinearity in human cells. *Proceedings of the National Academy of Sciences of the United States of America*, 109(2):443–8, jan 2012.

[283] Frank P. Castronovo. Teratogen update: Radiation and chernobyl. *Teratology*, 60(2):100–106, aug 1999.

[284] Edward J. Calabrese and Michael K. O'Connor. Estimating Risk of Low Radiation Doses A Critical Review of the BEIR VII Report and its Use of the Linear No-Threshold (LNT) Hypothesis. *Radiation Research*, 182(5):463–474, nov 2014.

[285] Y Tabarraie, S Refahi, M.H. Dehghan, and M Mashoufi. Impact of High Natural Background Radiation on Woman's Primary Infertility. *Research Journal of Biological Sciences*, 3(5):534–536, 2008.

[286] F. Zakeri, M. R. Rajabpour, S. A. Haeri, R. Kanda, I. Hayata, S. Nakamura, T. Sugahara, and M. J. Ahmadpour. Chromosome aberrations in peripheral blood lymphocytes of individuals living in high background radiation areas of Ramsar, Iran. *Radiation and Environmental Biophysics*, 50(4):571–578, nov 2011.

[287] G J Heyes, A J Mill, and M W Charles. Authors' reply. *The British Journal of Radiology*, 79(946):855–857, oct 2006.

[288] Andre Aurengo, Dietrich Averbeck, Andre Bonnin, Bernard Le Guen, Roland Masse, Roger Monier, Maurice Tubiana, Alain-Jacques Valleron, and Florent de Vathaire. Dose-effect relationship and estimation of the carcinogenic effects of low doses of ionizing radiation. Technical report, Académie des Sciences, Académie Nationale de Médecine, 2005.

[289] Brett (Health Physics Society) Burk. Radaition Risk in Perspective: Position statement of Health Physics Society, 2010.

[290] ANS. Health effects of low-level radaition, 2001.

[291] HPS. Society News Archive: BEIR VII Report Supports LNT Model.

[292] NRC. Low Levels of Ionizing Radiation May Cause Harm. Technical report, National Research Council, 2005.

[293] NIH. Stereotactic radiosurgery - CyberKnife: MedlinePlus Medical Encyclopedia, 2018.

[294] Lars Leksell. Stereotactic radiosurgery. *Journal of Neurology, Neurosurgery & Psychiatry*, 46(9):797–803, sep 1983.

[295] TheFreeDictionary. Stereotaxy - definition of stereotaxy by The Free Dictionary.

[296] David A. Larson. Introduction to Stereotactic Radiosurgery and Stereotactic Body Radiotherapy. In *Handbook of Evidence-Based Stereotactic Radiosurgery and Stereotactic Body Radiotherapy*, pages 1–7. Springer International Publishing, Cham, 2016.

[297] Lars Leksell. The stereotaxic method and radiosurgery of the brain. *Acta chirurgica Scandinavica*, 102(4):316–9, dec 1951.

[298] Rajni A. Sethi, Igor J. Barani, David A. Larson, and Mack Roach, III, editors. *Handbook of Evidence-Based Stereotactic Radiosurgery and Stereotactic Body Radiotherapy*. Springer International Publishing, Cham, 2016.

[299] Elekta. Clinical solutions for treating cancer and brain disorders, 2019.

[300] Stanley H. Benedict, Frank J. Bova, Brenda Clark, Steven J. Goetsch, William H. Hinson, Dennis D. Leavitt, David J. Schlesinger, and Kamil M. Yenice. Anniversary Paper : The role of medical physicists in developing stereotactic radiosurgery. *Medical Physics*, 35(9):4262–4277, aug 2008.

[301] Elekta. Gamma Knife Treatment Process, 2019.

[302] B Sarby. Cerebral radiation surgery with narrow gamma beams; physical experiments. *Acta radiologica: therapy, physics, biology*, 13(5):425–45, oct 1974.

[303] Josef (Na Homolce Hospital) Novotny. Radiosurgery by Leksell Gamma Knife. In *AAPM training course, Prague 2008*, Prague, 2008. AAPM training course.

[304] ARI. American Radiosurgery Inc. American Radiosurgery Inc., 2019.

[305] Daniel Mammoo. *Monte Carlo simulation and Film dosimetry of Rotating Gamma System Gamma ART-6000 output factors*. PhD thesis, Rosalind Frankin University of Medicine and Science, 2008.

[306] S. Agostinelli, J. Allison, K. Amako, J. Apostolakis, H. Araujo, P. Arce, M. Asai, D. Axen, S. Banerjee, G. Barrand, F. Behner, L. Bellagamba, J. Boudreau, L. Broglia, A. Brunengo, H. Burkhardt, S. Chauvie, J. Chuma, R. Chytracek, G. Cooperman, G. Cosmo, P. Degtyarenko, A. Dell'Acqua, G. Depaola, D. Dietrich, R. Enami, A. Feliciello, C. Ferguson, H. Fesefeldt, G. Folger, F. Foppiano, A. Forti, S. Garelli, S. Giani, R. Giannitrapani, D. Gibin, J.J. Gómez Cadenas, I. González, G. Gracia Abril, G. Greeniaus, W. Greiner, V. Grichine, A. Grossheim, S. Guatelli, P. Gumplinger, R. Hamatsu, K. Hashimoto, H. Hasui, A. Heikkinen, A. Howard, V. Ivanchenko, A. Johnson, F.W. Jones, J. Kallenbach, N. Kanaya, M. Kawabata, Y. Kawabata, M. Kawaguti, S. Kelner, P. Kent, A. Kimura, T. Kodama, R. Kokoulin, M. Kossov, H. Kurashige, E. Lamanna, T. Lampén, V. Lara, V. Lefebure, F. Lei, M. Liendl, W. Lockman, F. Longo, S. Magni, M. Maire, E. Medernach, K. Minamimoto, P. Mora de Freitas, Y. Morita, K. Murakami, M. Nagamatu, R. Nartallo, P. Nieminen, T. Nishimura, K. Ohtsubo, M. Okamura, S. O'Neale, Y. Oohata, K. Paech, J. Perl, A. Pfeiffer, M.G. Pia, F. Ranjard, A. Rybin, S. Sadilov, E. Di Salvo, G. Santin, T. Sasaki, N. Savvas, Y. Sawada, S. Scherer, S. Sei, V. Sirotenko, D. Smith, N. Starkov, H. Stoecker, J. Sulkimo, M. Takahata, S. Tanaka, E. Tcherniaev, E. Safai Tehrani, M. Tropeano, P. Truscott, H. Uno, L. Urban, P. Urban, M. Verderi, A. Walkden, W. Wander, H. Weber, J.P. Wellisch, T. Wenaus, D.C. Williams, D. Wright, T. Yamada, H. Yoshida, and D. Zschiesche. Geant4a simulation toolkit. *Nuclear Instruments and Methods in Physics Research Section A: Accelerators, Spectrometers, Detectors and Associated Equipment*, 506(3):250–303, 2003.

[307] J. Allison, K. Amako, J. Apostolakis, H. Araujo, P. Arce Dubois, M. Asai, G. Barrand, R. Capra, S. Chauvie, R. Chytracek, G.A.P. Cirrone, G. Cooperman, G. Cosmo, G. Cuttone, G.G. Daquino, M. Donszelmann, M. Dressel, G. Folger, F. Foppiano, J. Generowicz, V. Grichine, S. Guatelli, P. Gumplinger, A. Heikkinen, I. Hrivnacova, A. Howard, S. Incerti, V. Ivanchenko, T. Johnson, F. Jones, T. Koi, R. Kokoulin, M. Kossov, H. Kurashige, V. Lara, S. Larsson, F. Lei, O. Link, F. Longo, M. Maire, A. Mantero, B. Mascialino, I. McLaren, P. Mendez Lorenzo, K. Minamimoto, K. Murakami, P. Nieminen, L. Pandola, S. Parlati, L. Peralta, J. Perl, A. Pfeiffer, M.G. Pia, A. Ribon, P. Rodrigues, G. Russo, S. Sadilov, G. Santin, T. Sasaki, D. Smith, N. Starkov, S. Tanaka, E. Tcherniaev, B. Tome, A. Trindade, P. Truscott, L. Urban, M. Verderi, A. Walkden, J.P. Wellisch, D.C. Williams, D. Wright, and H. Yoshida. Geant4 developments and applications. *IEEE Transactions on Nuclear Science*, 53(1):270–278, feb 2006.

[308] J. Allison, K. Amako, J. Apostolakis, P. Arce, M. Asai, T. Aso, E. Bagli, A. Bagulya, S. Banerjee, G. Barrand, B.R. Beck, A.G. Bogdanov, D. Brandt, J.M.C. Brown, H. Burkhardt, Ph. Canal, D. Cano-Ott, S. Chauvie, K. Cho, G.A.P. Cirrone, G. Cooperman, M.A. Cortés-Giraldo, G. Cosmo, G. Cuttone, G. Depaola, L. Desorgher, X. Dong, A. Dotti, V.D. Elvira, G. Folger, Z. Francis, A. Galoyan, L. Garnier, M. Gayer, K.L. Genser, V.M. Grichine, S. Guatelli, P. Guèye, P. Gumplinger, A.S. Howard, I. Hivnáčová, S. Hwang, S. Incerti, A. Ivanchenko, V.N. Ivanchenko, F.W. Jones, S.Y. Jun, P. Kaitaniemi, N. Karakatsanis, M. Karamitros, M. Kelsey, A. Kimura, T. Koi, H. Kurashige, A. Lechner, S.B. Lee, F. Longo, M. Maire, D. Mancusi, A. Mantero, E. Mendoza, B. Morgan, K. Murakami, T. Nikitina, L. Pandola, P. Paprocki, J. Perl, I. Petrović, M.G. Pia, W. Pokorski, J.M. Quesada, M. Raine, M.A. Reis, A. Ribon, A. Ristić Fira, F. Romano, G. Russo, G. Santin, T. Sasaki, D. Sawkey, J.I. Shin, I.I. Strakovsky, A. Taborda, S. Tanaka, B. Tomé, T. Toshito, H.N. Tran, P.R. Truscott, L. Urban, V. Uzhinsky, J.M. Verbeke, M. Verderi, B.L. Wendt, H. Wenzel, D.H. Wright, D.M. Wright, T. Yamashita, J. Yarba, and H. Yoshida. Recent developments in Geant 4. *Nuclear Instruments and Methods in Physics Research Section A: Accelerators, Spectrometers, Detectors and Associated Equipment*, 835:186–225, nov 2016.

[309] J. Apostolakis, M. Asai, A.G. Bogdanov, H. Burkhardt, G. Cosmo, S. Elles, G. Folger, V.M. Grichine, P. Gumplinger, A. Heikkinen, I. Hrivnacova, V.N. Ivanchenko, J. Jacquemier, T. Koi, R.P. Kokoulin, M. Kossov, H. Kurashige, I. McLaren, O. Link, M. Maire, W. Pokorski, T. Sasaki, N. Starkov, L. Urban, and D.H. Wright. Geometry and physics of the Geant4 toolkit for high and medium energy applications. *Radiation Physics and Chemistry*, 78(10):859–873, oct 2009.

[310] Subramanian Raman. A note on 60Co decay. *Zeitschrift für Physik*, 228(5):387–390, oct 1969.

[311] F. Romano, M. G. Sabini, G. Cuttone, G. Russo, V. Mongelli, and R. Foroni. Geant4-based Monte Carlo simulation of the Leksell Gamma Knife®. In *IEEE Nuclear Science Symposium Conference Record*, volume 4, pages 2581–2586. IEEE, 2007.

[312] Reference Physics Lists, 2013.

[313] Jean L Nakamura, Andrea Pirzkall, Mark P Carol, Ping Xia, Vernon Smith, William M Wara, Paula L Petti, Lynn J Verhey, and Penny K Sneed. Comparison of intensity-modulated radiosurgery with gamma knife radiosurgery for challenging skull base lesions. *International Journal of Radiation Oncology*Biology*Physics*, 55(1):99–109, jan 2003.

[314] David J Brenner, Richard Doll, Dudley T Goodhead, Eric J Hall, Charles E Land, John B Little, Jay H Lubin, Dale L Preston, R Julian Preston, Jerome S Puskin, Elaine Ron, Rainer K Sachs, Jonathan M Samet, Richard B Setlow, and Marco Zaider. Cancer risks attributable to low doses of ionizing radiation: assessing what we really know. *Proceedings of the National Academy of Sciences of the United States of America*, 100(24):13761–6, nov 2003.

[315] David J. Brenner and Eric J. Hall. Computed Tomography An Increasing Source of Radiation Exposure. *New England Journal of Medicine*, 357(22):2277–2284, nov 2007.

[316] Rebecca Smith-Bindman. Is Computed Tomography Safe? *New England Journal of Medicine*, 363(1):1–4, jul 2010.

[317] E. Stephen Amis, Priscilla F. Butler, Kimberly E. Applegate, Steven B. Birnbaum, Libby F. Brateman, James M. Hevezi, Fred A. Mettler, Richard L. Morin, Michael J. Pentecost, Geoffrey G. Smith, Keith J. Strauss, and Robert K. Zeman. American College of Radiology White Paper on Radiation Dose in Medicine. *Journal of the American College of Radiology*, 4(5):272–284, may 2007.

[318] H Benjamin Harvey and Pari V Pandharipande. The federal government's oversight of CT safety: regulatory possibilities. *Radiology*, 262(2):391–8, feb 2012.

[319] CDRH. Initiative to Reduce Unnecessary Radiation Exposure from Medical Imaging - White Paper: Initiative to Reduce Unnecessary Radiation Exposure from Medical Imaging. Technical report, US FDA, 2010.

[320] M Wintermark and M H Lev. FDA investigates the safety of brain perfusion CT. *AJNR. American journal of neuroradiology*, 31(1):2–3, jan 2010.

[321] Tao Lu, Ye Zhang, Michael Wong, Alan Feiveson, Ramona Gaza, Nicholas Stoffle, Huichen Wang, Bobby Wilson, Larry Rohde, Louis Stodieck, Fathi Karouia, and Honglu Wu. Detection of DNA damage by space radiation in human fibroblasts flown on the International Space Station. *Life Sciences in Space Research*, 12:24–31, feb 2017.

[322] Marjan Boerma, Gregory A Nelson, Vijayalakshmi Sridharan, Xiao-Wen Mao, Igor Koturbash, and Martin Hauer-Jensen. Space radiation and cardiovascular disease risk. *World Journal of Cardiology*, 7(12):882, 2015.

[323] Hongyu Jiang, Wei Li, Xiuyi Li, Lu Cai, and Guanjun Wang. Low-Dose Radiation Induces Adaptive Response in Normal Cells, but not in Tumor Cells: In vitro and in vivo Studies. *Journal of Radiation Research*, 49(3):219–230, may 2008.

[324] Anne Kiuru, Meerit Kämäräinen, Sirpa Heinävaara, Katri Pylkäs, Kim Chapman, Armi Koivistoinen, Teuvo Parviainen, Robert Winqvist, Munira Kadhim, Virpi Launonen, and Carita Lindholm. Assessment of Targeted and Non-Targeted Responses in Cells Deficient in ATM Function following Exposure to Low and High Dose X-Rays. *PLoS ONE*, 9(3):e93211, mar 2014.

[325] Ming Chen, Qun Huang, Wei Xu, Chang She, Zong-Gang Xie, Yong-Tao Mao, Qi-Rong Dong, and Ming Ling. Low-Dose X-Ray Irradiation Promotes Osteoblast Proliferation, Differentiation and Fracture Healing. *PLoS ONE*, 9(8):e104016, aug 2014.

[326] Xinyue Liang, Junlian Gu, Dehai Yu, Guanjun Wang, Lei Zhou, Xiaoying Zhang, Yuguang Zhao, Xiao Chen, Shirong Zheng, Qiang Liu, Lu Cai, Jiuwei Cui, and Wei Li. Low-Dose Radiation Induces Cell Proliferation in Human Embryonic Lung Fibroblasts but not in Lung Cancer Cells. *Dose-Response*, 14(1):155932581562217, feb 2016.

[327] Feng Ru Tang, Weng Keong Loke, and Boo Cheong Khoo. Low-dose or low-dose-rate ionizing radiationinduced bioeffects in animal models. *Journal of Radiation Research*, 58(2):165–182, jan 2017.

[328] Hannah Cash. The Mechanical and Functional Effects of Ionizing Radiation on Articular Cartilage. *All Dissertations*, may 2019.

[329] Sterling Cornaby and Kris Kozaczek. X-Ray Sources for Handheld X-Ray Fluorescence Instruments. In *Encyclopedia of Analytical Chemistry*, pages 1–25. John Wiley & Sons, Ltd, Chichester, UK, jun 2016.

[330] HDPE cup, Chemplex Industries Inc., Palm City, FL.

[331] XPIN-13XT X-Ray Detector, Moxtek Inc., Orem, Utah.

[332] Isotemp Microbiological Incubator, Fisher Scientific.

[333] Frank H. Attix and Wiley InterScience (Online service). *Introduction to radiological physics and radiation dosimetry*. Wiley, 1986.

[334] B.L. Henke, E.M. Gullikson, and J.C. Davis. X-Ray Interactions: Photoabsorption, Scattering, Transmission, and Reflection at E = 50-30,000 eV, Z = 1-92. *Atomic Data and Nuclear Data Tables*, 54(2):181–342, jul 1993.

[335] Katelyn Truong, Suzanne Bradley, Bryana Baginski, Joseph R. Wilson, Donald Medlin, Leon Zheng, R. Kevin Wilson, Matthew Rusin, Endre Takacs, and Delphine Dean. The effect of well-characterized, very low-dose x-ray radiation on fibroblasts. *PLOS ONE*, 13(1):e0190330, jan 2018.